



저작자표시-비영리-변경금지 2.0 대한민국

이용자는 아래의 조건을 따르는 경우에 한하여 자유롭게

- 이 저작물을 복제, 배포, 전송, 전시, 공연 및 방송할 수 있습니다.

다음과 같은 조건을 따라야 합니다:



저작자표시. 귀하는 원저작자를 표시하여야 합니다.



비영리. 귀하는 이 저작물을 영리 목적으로 이용할 수 없습니다.



변경금지. 귀하는 이 저작물을 개작, 변형 또는 가공할 수 없습니다.

- 귀하는, 이 저작물의 재이용이나 배포의 경우, 이 저작물에 적용된 이용허락조건을 명확하게 나타내어야 합니다.
- 저작권자로부터 별도의 허가를 받으면 이러한 조건들은 적용되지 않습니다.

저작권법에 따른 이용자의 권리는 위의 내용에 의하여 영향을 받지 않습니다.

이것은 [이용허락규약\(Legal Code\)](#)을 이해하기 쉽게 요약한 것입니다.

[Disclaimer](#)

공학박사학위논문

데이터 분석 기반
복합소재 박판 보의 유한요소 모델 개발

Data-driven Approach for the Development of
a Finite Element Model for Composite Thin-walled Beam

2019년 8월

서울대학교 대학원
기계항공공학부
신 동 일

데이터 분석 기반 복합소재 박판 보의 유한요소 모델 개발

Data-driven Approach for the Development of
a Finite Element Model for Composite Thin-walled Beam

지도교수 김 윤 영

이 논문을 공학박사 학위논문으로 제출함
2019년 4월

서울대학교 대학원
기계항공공학부
신 동 일

신동일의 공학박사 학위논문을 인준함
2019년 6월

위원장 : 조 맹 효

부위원장 : 김 윤 영

위 원 : 김 도 년

위 원 : 윤 병 동

위 원 : 장 강 원

ABSTRACT

Data-driven Approach for the Development of a Finite Element Model for Composite Thin-walled Beam

Dongil Shin

School of Mechanical and Aerospace Engineering

The Graduate School

Seoul National University

To analyze the behavior of the thin-walled beams using one-dimensional beam finite elements, considering complex cross-sectional deformations happening on the beam section is important. When it comes to composite thin-walled beams, the accurate definition of shape functions that describe local cross-sectional deformation becomes more critical. It is because anisotropic and laminate effects produce more complicated deformation patterns that do not appear in isotropic beams. This dissertation deals with identifying shape functions required for composite thin-walled beams and expand the higher-order beam theory which was

limited to isotropic thin-walled beams before.

Here, a data-driven approach was conducted to extract the shape functions required for general composite thin-walled beams consist of various cross-sections, ply orientations and stacking sequences. From the shell-based static analysis results of composite beams, big data representing cross-sectional deformations were obtained and then the principal component analysis was performed to identify shape functions. Compared with previous researches deriving shape functions of composite thin-walled beams, proposed approach identified them without various kinematic assumptions. Also, the shape functions were derived generally without considering a specific condition of ply orientation or stacking sequence.

The higher-order beam elements using these shape functions deal with static, vibration and buckling analysis of composite thin-walled beams under general conditions. This dissertation demonstrates that the present results agree well with those obtained by shell analysis results by numerical examples. The proposed research is expected to be applied at various industrial fields requiring composite thin-walled beam models.

Keywords: Laminates, Anisotropy, Thin-walled Beam, Cross-sectional Deformations, Data-driven Analysis, Finite Element Method

Student Number: 2013-22493

CONTENTS

ABSTRACT	i
CONTENTS.....	iii
LIST OF TABLES.....	vi
LIST OF FIGURES.....	viii
CHAPTER 1. INTRODUCTION	1
1.1 Motivation.....	1
1.2 Previous works	5
1.3 Research objectives	10
1.4 Outline of thesis	12
CHAPTER 2. Higher-order beam formulation.....	16
2.1 Overview	16
2.2 Theoretical review: Higher-order beam theory for isotropic thin-walled beam.....	17
2.3 Higher-order beam theory for composite thin-walled beam	20
2.4 Higher-order beam finite element formulation.....	22
2.4.1 Formulation for static analysis	22
2.4.2 Formulation for vibration analysis	24
2.4.3 Formulation for buckling analysis.....	25

CHAPTER 3. Data-driven approach for deriving shape functions of composite thin-walled beams	29
3.1 Overview	29
3.2 Preparing cross-sectional deformation big data	30
3.2.1 Cross-sectional deformation data required for isotropic materials or a certain composite.....	30
3.2.2 Cross-sectional deformation data required for general composites	32
3.3 Pre-process of cross-sectional deformation data	37
3.4 Data-driven analysis for obtaining principal cross-sectional deformations	39
3.5 Post-process required for defining shape functions.....	41
CHAPTER 4. Numerical examples and discussions	49
4.1 Overview	49
4.2 Examples using data-driven shape functions for isotropic thin-walled beams.....	50
4.2.1 Verification of static, vibration and buckling analysis	52
4.2.2 Examples dealing with the validation of the data-driven approach	57
4.3 Examples using data-driven shape functions for composite thin-walled beams.....	62
4.3.1 Verification of static, vibration and buckling results.....	64

4.3.2 Examples dealing with special issues in a composite thin-walled beam under the data-driven approach	69
CHAPTER 5. Conclusions.....	110
APPENDIX A. Physical approach for deriving shape functions of composite thin-walled box beams.....	113
A.1 Overview	113
A.2 Cross-sectional deformations derived by plane stress assumption.....	115
A.3 Definition of sectional shape functions for degrees of freedom.....	127
A.4 Examples	131
REFERENCES.....	151
ABSTRACT (KOREAN).....	161

LIST OF TABLES

Table 4.1 Eigenfrequencies obtained by the data-driven approach with different numbers of sectional shape functions (12, 18, and 24 DOFs) for a free-free isotropic beam having the cross-section shown in Fig. 4.1 (d) (unit: Hz).....	75
Table 4.2 Eigenfrequencies obtained by the data-driven approach with different numbers of sectional shape functions (12, 18, and 24 DOFs) for a clamped-clamped isotropic beam having the cross-section shown in Fig. 4.1 (d) (unit: Hz)	76
Table 4.3 The critical load (P_{cr}) calculated by the data-driven approach using different numbers of sectional shape functions (12, 18, and 24 DOFs) for a isotropic cantilever beam under a compressive load having the cross-section shown in Fig. 4.1 (d) with different beam lengths (L) (unit: N)	77
Table 4.4 Eigenfrequencies obtained by the data-driven approach with different numbers of sectional shape functions (15, 30, 45, and 60 DOFs) for a free-free composite beam having the cross-section shown in Fig. 4.1 (a) (unit: Hz)	78
Table 4.5 Eigenfrequencies obtained by the data-driven approach with different numbers of sectional shape functions (15, 30, 45, and 60 DOFs) for a clamped-clamped composite beam having the cross-section shown in Fig. 4.1 (a) (unit: Hz)	79
Table 4.6 The critical load (P_{cr}) calculated by the data-driven approach using different numbers of sectional shape functions (15, 30, 45, and 60 DOFs) for a composite cantilever beam under a compressive load having the cross-section	

shown in Fig. 4.1 (a) with different beam lengths (L) (unit: N).....80

Table A.1 Bending rotation predicted for various beam thickness by the proposed higher-order beam approach at the tip of composite box beam, and the relative errors with respect to the shell calculation 136

Table A.2 Torsional rotation predicted for various beam thicknesses by the proposed higher-order beam approach at the tip of composite box beam, and the relative errors with respect to the shell calculation 137

Table A.3 Bending rotation predicted for various lengths by the proposed higher-order beam approach at the tip of composite box beam, and the relative errors with respect to the shell calculation 138

Table A.4 Torsional rotation predicted for various lengths by the proposed higher-order beam approach at the tip of composite box beam, and the relative errors with respect to the shell calculation 139

LIST OF FIGURES

Fig. 1.1 Illustration of (a) cross-sectional deformation data from the shell analysis results and (b) shape functions bases of cross-sectional deformation.....	14
Fig. 1.2 Illustration of the cross-sectional deformation of the composite thin-walled box beam by various effects.....	15
Fig. 2.1 Coordinate system used for the analysis of the composite thin-walled beam and geometric parameters.....	28
Fig. 3.1 The procedure used to obtain data-driven shape functions corresponding to the higher-order degrees of freedom. First step: <i>Preparing Big Data</i>	45
Fig. 3.2 The procedure used to obtain data-driven shape functions corresponding to the higher-order degrees of freedom. Second step: <i>Pre-processing</i>	46
Fig. 3.3 The procedure used to obtain data-driven shape functions corresponding to the higher-order degrees of freedom. Third step: <i>Principal Component Analysis</i> ..	47
Fig. 3.4 The procedure used to obtain data-driven shape functions corresponding to the higher-order degrees of freedom. Last step: <i>Post-processing</i>	48
Fig. 4.1 Various beam cross-sections considered for analysis: (a) box beam, (b) lipped channel beam, (c) double-cell beam, and (d) general section beam.....	81
Fig. 4.2 Sectional shape functions of the isotropic thin-walled beam derived by the data-driven approach for the cross-section in Fig. 4.1 (a).....	82
Fig. 4.3 Sectional shape functions of the isotropic thin-walled beam derived by the data-driven approach for the cross-section in Fig. 4.1 (b).....	83

Fig. 4.4 Sectional shape functions of the isotropic thin-walled beam derived by the data-driven approach for the cross-section in Fig. 4.1 (c).....84

Fig. 4.5 Sectional shape functions of the isotropic thin-walled beam derived by the data-driven approach for the cross-section in Fig. 4.1 (d).....85

Fig. 4.6 Numerical results for Example 1 in Chapter 4.2 for (a) *Loading condition 1* and (b) *Loading condition 2*. The three-dimensional displacements in the *X*-, *Y*- and *Z*-directions are plotted by the present data-driven one-dimensional analysis using 12, 18 and 24 degrees of freedom and compared with the shell-based results. The measurements were taken at point $*_a$ (see Fig. 4.1 (d)) of the cross-section along the beam axial axis86

Fig. 4.7 Eigenmodes obtained for Example 2 in Chapter 4.2 (a) free-free beam and (b) clamped-clamped beam. *Shell*: the result by ABAQUS shell elements, *Proposed*: the result by the present data-driven beam elements.....87

Fig. 4.8 Buckling mode shapes in beams under axial compression for Example 2 in Chapter 4.2. *L*: beam length, *Shell*: the result by ABAQUS shell elements, *Proposed*: the result by the present data-driven beam elements88

Fig. 4.9 Numerical results for a isotropic box beam. Three-dimensional displacement along the *Z* (axial) coordinate along (45, 120) (see Fig. 4.1 (a)) of the wall center subjected to (a) shear line force of 1N applied to the $*_a$ - $*_b$ edge in the *Y* direction and (b) normal line force of 1N applied to the $*_c$ - $*_d$ edge in the *X* direction. (c) Eigenmodes with eigenfrequencies in the free-free beam, and (d) buckling mode shapes with the critical load in the cantilevered beam under a

compression load.....89

Fig. 4.10 Numerical results for a isotropic lipped channel beam. Three-dimensional displacement along the Z (axial) coordinate along (30, 120) (see Fig. 4.1 (b)) of the wall center subjected to (a) shear line force of 1N applied to the $*_c - *_d$ edge in the Y direction and (b) normal line force of 1N applied to the $*_b - *_c$ edge in the Y direction. (c) Eigenmodes with eigenfrequencies in the free-free beam, and (d) buckling mode shapes with the critical load in the cantilevered beam under a compression load.....90

Fig. 4.11 Numerical results for a isotropic double-cell beam. Three-dimensional displacement along the Z (axial) coordinate along (30, 120) (see Fig. 4.1 (c)) of the wall center subjected to (a) a shear line force of 1N applied to the $*_a - *_b$ edge in the Y direction and (b) a normal line force of 1N applied to the $*_d - *_e$ edge in the X direction. (c) Eigenmodes with eigenfrequencies in the free-free beam, and (d) buckling mode shapes with the critical load in the cantilevered beam under a compression load.....91

Fig. 4.12 The tendencies of the eigenvalue of the principal components corresponding to each beam sections in Fig. 4.1 for Chapter 4.2.1. (a) Eigenvalue proportion and (b) Remain proportion92

Fig. 4.13 The effects of the data size on the solution accuracy for Example 3 in Chapter 4.2. Errors in the mean compliance are plotted for (a) the proposed approach when the reference beam length varies from 0.15 m to 0.9 m and (b) the proposed approach when downsampling among the total amount of cross-sectional

deformation data when the beam length is fixed at 0.6 m.....	93
Fig. 4.14 The effects of the shell mesh resolution on the solution accuracy for Example 4 in Chapter 4.2. Errors by larger shell mesh analyses (<i>Mesh M, Mesh C</i>) and data-driven beam analysis corresponding to shape functions obtained when using different shell mesh sizes (<i>Mesh F, Mesh M, Mesh C</i>) are plotted	94
Fig. 4.15 The effects of the selected data sets on the solution accuracy for Example 5 in Chapter 4.2. Errors in the mean compliance for (a) <i>Loading condition 3</i> and (b) <i>Loading condition 4</i> , and (c) deformation configuration at the free end of the thin-walled beam model under <i>Loading condition 4</i> using 24 degrees of freedom.....	95
Fig. 4.16 Sectional shape functions of the composite thin-walled beam derived by the data-driven approach for the cross-section in Fig. 4.1 (a).....	96
Fig. 4.17 Sectional shape functions of the composite thin-walled beam derived by the data-driven approach for the cross-section in Fig. 4.1 (b).....	97
Fig. 4.18 Sectional shape functions of the composite thin-walled beam derived by the data-driven approach for the cross-section in Fig. 4.1 (d).....	98
Fig. 4.19 Numerical results for Example 1 in Chapter 4.3 for (a) <i>Loading condition 1</i> , (b) <i>Loading condition 2</i> and (c) <i>Loading condition 3</i> . The three-dimensional displacements in the <i>X</i> -, <i>Y</i> - and <i>Z</i> -directions are plotted by the present data-driven one-dimensional analysis using 15, 30 and 45 degrees of freedom and compared with the shell-based results. The measurements were taken at point (45, 120) (see Fig. 4.1 (a)) of the cross-section along the beam axial axis	99
Fig. 4.20 Eigenmodes obtained for Example 2 in Chapter 4.3 (a) free-free beam	

and (b) clamped-clamped beam. *Shell*: the result by ABAQUS shell elements, *Proposed*: the result by the present data-driven beam elements 100

Fig. 4.21 Buckling mode shapes in beams under axial compression for Example 2 in Chapter 4.3. *L*: beam length, *Shell*: the result by ABAQUS shell elements, *Proposed*: the result by the present data-driven beam elements 101

Fig. 4.22 Numerical results for a composite lipped channel beam. Three-dimensional displacement along the *Z* (axial) coordinate along (30, 120) (see Fig. 4.1 (b)) of the wall center subjected to (a) shear line force of 1N applied to the $*_c - *_d$ edge in the *Y* direction and (b) normal line force of 1N applied to the $*_b - *_c$ edge in the *Y* direction. (c) Eigenmodes with eigenfrequencies in the free-free beam, and (d) buckling mode shapes with the critical load in the cantilevered beam under a compression load..... 102

Fig. 4.23 Numerical results for a composite general section beam. Three-dimensional displacement along the *Z* (axial) coordinate along $*_a$ (see Fig. 4.1 (d)) of the wall center subjected to (a) shear line force of 1N applied to the $*_c - *_d$ edge in the *Y* direction and (b) normal line force of 1N applied to the $*_h - *_d$ edge in the *Y* direction. (c) Eigenmodes with eigenfrequencies in the free-free beam, and (d) buckling mode shapes with the critical load in the cantilevered beam under a compression load..... 103

Fig. 4.24 Numerical results for Example 3 in Chapter 4.3 conducted with a single-layer composite thin-walled box beam under torsional moment and bending moment..... 104

Fig. 4.25 Numerical results for Example 3 in Chapter 4.3 for (a) *Loading condition 1* and (b) *Loading condition 2*. The three-dimensional displacements in the X -, Y - and Z -directions are plotted by the present data-driven one-dimensional analysis using 45 degrees of freedom and compared with the shell-based results. The measurements were taken at point (45, 120) (see Fig. 4.1 (a)) of the cross-section along the beam axial axis 105

Fig. 4.26 The effects of the selected data sets on the solution accuracy for Example 4 in Chapter 4.3. Errors in the mean compliance for (a) *Loading condition 1* and (b) *Loading condition 2* 106

Fig. 4.27 MAC values between shape functions obtained by different data sets for Example 4 in Chapter 4.3. (a) *Data set A1* and *Data set A7*, (b) *Data set A3* and *Data set A7* and (c) *Data set A5* and *Data set A7*..... 107

Fig. 4.28 The effects of the selected data sets on the solution accuracy for Example 5 in Chapter 4.3. Errors in the mean compliance for (a) *Loading condition 1* and (b) *Loading condition 2* 108

Fig. 4.29 MAC values between shape functions obtained by different data sets for Example 5 in Chapter 4.3. (a) *Data set Iso* and *Data set A5* and (b) *Data set [30°]* and *Data set A5* 109

Fig. A.1 The coordinate system used for the analysis of the composite thin-walled box beam and the detail geometry parameters 140

Fig. A.2 Schematic to explain the process to derive the displacement field associated with M_y 141

Fig. A.3 Derived cross-section deformation functions associated with out-of-plane loads	142
Fig. A.4 Derived cross-section deformation functions associated with in-plane loads	143
Fig. A.5 Sectional shape functions for the degrees of freedom employed in the Higher-order Beam Theory for composite thin-walled box beams.....	144
Fig. A.6 Numerical results for Example 1 in Appendix A to examine the effects of the linear and Hermite finite element interpolation functions. The composite box beam is subjected to (a) bending moment and (b) torsional moment.....	145
Fig. A.7 Numerical results for Example 3 in Appendix A in a single-layer composite thin-walled box beam under bending moment. Three-dimensional displacements at $s=b/2$ at the center of (a) wall 2 and (b) wall 4.....	146
Fig. A.8 Numerical results for Example 3 in Appendix A in a single-layer composite thin-walled box beam under torsional moment. Three-dimensional displacements at $s=b/2$ at the center of (a) wall 2 and (b) wall 4.....	147
Fig. A.9 Static analysis results for Example 4 in Appendix A considering bending moment loading. (a) Three-dimensional displacement at $s=0$ at the center of wall 1 and (b) stress at $s=b/40$ at the outermost ply of wall 1	148
Fig. A.10 Static analysis results for Example 4 in Appendix A considering torsional moment loading. (a) Three-dimensional displacement at $s=0$ at the center of wall 1 and (b) stress at $s=b/40$ at the outermost ply of wall 1	149
Fig. A.11 Free vibration analysis results for Example 4 in Appendix A. (a)	

ABAQUS shell results and (b) the present higher-order beam theory results150

CHAPTER 1.

INTRODUCTION

1.1 Motivation

As large amounts of data become available, and data analysis techniques evolve, data-driven approaches are expanding to the field of structural engineering. There are two main reasons why data-driven approaches are attractive to researchers. The first advantage they offer is that the design can be performed at a significantly faster rate than the conventional structural design. For example, in structural analysis studies, deep learning has been applied to select the Gauss point to reduce the analysis cost in a finite element analysis [1], and in the area of topology optimization, research is being conducted using base data to reduce the design time cost [2] or to search for crucial design parameters [3]. Second and more importantly, many researchers are keenly interested in expanding deductive research methods to the area of inductive research methods because the errors and uncertainties that have occurred due to an insufficient understanding of physical phenomena can be reflected in a data-driven analysis. As an example, studies of

data-driven computational mechanics using experimental data are expanding. Neggers et al. [4] performed model/data reductions to simplify experimental information and make using it more efficient, and Kirchdoerfer and Ortiz [5-7] are actively researching data-driven computational mechanics utilizing a data set obtained from physical experiments, without resorting to empirical modeling. Other data-driven studies in a variety of fields, such as dynamic problems [8], fuzzy data [9], and material designs [10], can also be found.

In the field of finite element modeling, elements can be roughly divided into the one, two, and three-dimensional types based on the geometry of the model under consideration. In most cases, we prefer low-dimensional elements that fit the geometric dimensions, taking into account the ease of the design and the analysis time cost. However, in some cases, the expression is possible geometrically as a low-dimensional element, but it is difficult to trust the analytical results in such cases because there are physical phenomena that cannot be expressed in such low dimensions. Thin-walled beams, widely used throughout the industry due to their excellent mass-to-stiffness ratios, represent a typical example. When an external force is applied, as shown in Fig. 1.1 (a), complicated cross-sectional deformation occurs in the beam cross-section, including distortion and warping. Given that classical one-dimensional beam elements consider only rigid deformation in the beam section, it is impossible to describe the complex deformation of the beam accurately. Therefore, in the real world, thin-walled beams are analyzed by a two-

dimensional shell element or a three-dimensional continuum element, and the advantage of using a one-dimensional beam element is not realized.

If the thin-walled beam is composed of composite materials, cross-sectional deformation happens more complicated. Composite materials have been widely used to reduce the weight of a structure without sacrificing stiffness. In particular, laminated composites can be tailored to meet various design requirements and have been utilized as efficient load-carrying members in automobiles and aircraft. Figure 1.2 shows a composite thin-walled beam under an axial load (in the z -direction). In this figure, we indicate that various deformation patterns can simultaneously occur. Specifically, we argue that in addition to typical deformation patterns that occur in an isotropic beam (indicated by “*isotropic effect*”), additional deformation patterns also appear because of anisotropic and laminated effects if the thin-walled beam is made of a composite material. If these effects are not appropriately taken into account when considering cross-sectional deformations, it may be difficult to obtain accurate results.

To overcome the hard of describing the complex deformation of the composite thin-walled beam, advanced beam theories which consider cross-sectional deformation have been devised. In these theories, sectional shape functions corresponding higher-order beam degrees of freedom are introduced, where they form the bases upon which to represent general cross-sectional deformation, as

shown in Fig. 1.1 (b). The critical consideration in these theories is how to define sectional shape functions, such as warping and distortion, in addition to six rigid-body motions of the beam cross-section.

This thesis presents a one-dimensional composite thin-walled beam finite element model expanding earlier research on isotropic thin-walled beam. Additional conditions required for updating finite element formulation of composite thin-walled beams are addressed, and a data-driven approach for identifying core cross-sectional deformations of composite thin-walled beams is proposed. In spite of the many available approaches that define sectional shape functions, it remains challenging to determine more critical shape functions. Besides, it is sometimes hard to derive shape functions for beams with complicated, non-uniform, or reinforced sections. Motivated by this, we propose a data-driven approach to acquiring such shape functions by collecting and analyzing the section deformations occurring in composite thin-walled beams modeled by a two-dimensional refined shell model.

1.2 Previous works

Recent works on advanced beam theories

To overcome the hard of analyzing thin-walled beams, advanced beam theories which consider cross-sectional deformation have been devised. As mentioned above, several advanced beam models performed more accurate beam analyses by considering not only rigid body motions but also several local cross-sectional deformations as additional degrees of freedom. If we consider for isotropic thin-walled beam analysis first, advanced beam theories have been extensively developed for decades since Vlasov [11] proposed a thin-walled beam theory that takes into account warping deformation in the Saint-Venant torsion problem. Since then, a number of investigations to establish advanced beam theories and derive the corresponding beam finite elements have been reported [12-43]. The core idea about the establishment of these theories and finite elements lies in how to define or derive the sectional shape functions. Although it is difficult to subdivide the methods precisely, there are roughly three approaches which can be used to define shape functions. The first is to define the displacement field of the section through geometric characteristics. As typical examples, Carrera and his colleagues conducted shape functions [13-16] by expanding the displacement field using methods such as Lagrangian and Taylor expansion, Camotim and his researchers [17-21] formed shape functions by imposing a unit displacement on a particular node or wall while forcing other displacements to comply with null or to deform under some assumptions, and Vieira et al. [22-24] derived shape functions by

solving the eigenvalue problem on a set of linearly independent basis functions from the bar model of a thin-walled beam section. Other methods defined shape functions through a two-dimensional analysis of the beam cross-section. Hodges and related researchers [25-27] decomposed a three-dimensional elasticity problem into a one-dimensional problem along the axial direction and a two-dimensional problem along the beam cross-section and then derived a beam-type equation that takes into account the higher order effects. Genoese et al. [28-30] developed a model that reflects sectional shape functions by solving a generalized eigenvalue problem of the two-dimensional model of a thin-walled beam section. Lastly, other methods seek to obtain shape functions by solving the equilibrium equation generated from the physics of the beam. For example, Ferradi et al. [31-33] proposed a means of determining transverse deformations and warping deformations iteratively using their equilibrium equations along the beam, and Kim and his researchers [34-43] derived sectional deformation shapes in a closed form using a generalized force-stress relationship.

Recent works on composite thin-walled beams

Considering composite thin-walled beams, Loughlan and Ata [44] used a theoretical model to assess warping in the static analysis of composite thin-walled beams and Vo and Lee [45] predicted the response of symmetric and asymmetric stacked beams based on shear-deformable theories. Cesnik and Hodges [46] and Yu et al. [47] used variational asymptotic beam section analysis to study the exact

stiffness of beam sections. Jung et al. [48] used Reissner's semi-complementary energy function to analyze the coupling between global deformations of composite thin-walled beams, and Sheikh and Thomsen [49] performed an analysis of thin-walled open and closed beams. Studies on wave propagation [50], vibration [51], and buckling [52] in composite thin-walled beams were also reported. Aside from the studies mentioned above, a more extensive review on laminated composite and sandwich beams may be found in Sayyad and Ghugal [53].

Several studies performed more accurate beam analyses by considering not only torsional warping but also several sectional shape functions that describe the local cross-sectional deformations associated with the additional degrees of freedom. Silvestre and Camotim [54, 55] conducted static and buckling analyses based on the Generalized Beam Theory. They defined cross-sectional deformation modes by considering the geometric characteristics of the beam section. Carrera et al. [56-58] conducted various studies to analyze composite thin-walled beams based on the Carrera Unified Formulation theory. Their sectional shape functions are obtained by expanding displacement fields using a method such as the Lagrangian expansion method. Genoese et al. [59] defined the sectional shape functions for distortion and warping by using two-dimensional analysis on beam cross-sections. However, no earlier study has taken a data-driven approach to identify the shape functions to the best of our knowledge.

Recent works on the data-driven approach in structural analysis field

Recently, several attempts were made to apply data-driven approaches to analyze and design beam structures. Susac et al. [60] conducted a study to predict the beam buckling load when the design variables change through an artificial neural network, and Ferreiro-Cabello et al. [61] obtained a Pareto set of major factors during a slab design process through deep learning. Additionally, Lee et al. [62] checked the parameters and key factors that should be considered when applying deep learning to a structural analysis using beam structure examples. However, to the best of our knowledge, this is the first time thin-walled beam element models are created by a data-driven approach in the finite element analysis field.

In this thesis, we obtain cross-sectional deformation data through various static analysis results based on shell elements and conduct a data-driven analysis. Specifically, we adopted principal component analysis as the means of obtaining the sectional shape functions essential for composite thin-walled beam analysis. Principal component analysis is a feature-extraction method for dimension reduction in data analysis. It expresses data in a low-dimensional format while maintaining minimum information loss using the dependency between high-dimensional data variables [63]. The principal component analysis approach was previously used in several approaches involving a structural analysis. Aschheim et al. [64] used principal component analysis to analyze dominant vibration modes during seismic excitations. The relationship between the sample size and the error

when using the principal component analysis was also discussed [65], and the interstory drift occurring in low-level diaphragm structures was estimated [66]. It was also used to analyze imperfections in structures [67], to extract damage patterns from frequency response function data to predict damage [68] and to undertake damage detection by selecting a damage index [69]. Because the principal component analysis is a data analysis method, it can be used to identify core bases when well-defined data can be obtained. Here, the principal component analysis is used to extract the core shape functions of section deformations occurring in a composite thin-walled beam. Because big data from the refined shell analysis of a composite thin-walled beam under various selected static loads is used, the principal component analysis based approach does not require any assumptions about beam sectional deformations, as typically required in earlier thin-walled beam analyses. Therefore, the proposed principal component analysis based data-driven approach can be applied to beam sections of any shape, including open or closed sections, with or without symmetry.

1.3 Research objectives

In this dissertation, an efficient one-dimensional beam theory for composite thin-walled beam analysis based on a higher-order beam theory is proposed. This theory includes degrees of freedom that describe the local cross-sectional deformations necessary to depict the complicated deformations that occur in composite thin-walled beams. The theory is updated so that it can represent the effects of anisotropic properties and lamination of composite materials. Although several pre-existing beam-based methods consider additional degrees of freedom associated with local sectional deformations (such as warping and distortion), a refined higher-order beam analysis that utilizes systematically derived sectional shape functions to describe local cross-sectional deformations is expected to yield more accurate results.

The shape functions of cross-sectional deformations are derived through data processing using the shell-based static analysis results of a composite thin-walled beam. We perform a principal component analysis during the data processing step, in which the desired shape functions are obtained without any specific assumptions on the behavior of cross-sectional deformations. Compared to previous analytical or numerical models often requiring various kinematic assumptions, this approach requires no such assumptions. Moreover, the approach was shown to be valid for various types of cross-sections, making it possible to prioritize significant cross-sectional deformations. Cross-sectional deformations required for thin-walled beam

analysis involves not only deformation happening from the weakness of the cross-section but also deformations occurring due to axial motions related to the thin-walled beam's three-dimensional behavior. One of the typical examples is 'Poisons modes' [39, 70] that includes the stretch of each wall of the thin-walled beams. These deformations are hard to obtain from the eigenvalue analysis of the beam's cross-section in lower eigenmodes without specific kinematic assumptions or additional conditions [70]. Also, cross-sectional deformations obtained through the previous eigenvalue analysis of the beam cross-section gives the weakest deformation of the beam section, which is not the proper order for the general beam analysis. In other words, it gives cross-sectional deformations according to weak deformation of the beam section which differs from the order of dealing with the beam's general motion. However, our approach can found these cross-sectional deformations directly in the lower principal cross-sectional deformations.

Important issues related to the establishment of a well-defined dataset are addressed, and the procedure by which to incorporate the obtained shape functions for a higher-order beam analysis is presented. A series of static, vibration and buckling analyses using data-driven shape functions are performed for various composite thin-walled beams. We demonstrate by numerical examples that the present data-driven results agree well with those obtained by shell analysis results, and discuss data related issues concerning physical backgrounds.

1.4 Outline of thesis

The thesis is organized as follows.

In **Chapter 2**, a higher-order beam formulation for an efficient structural analysis of composite thin-walled beams will be presented. Because the effects of anisotropic properties and lamination cannot be taken into account in the earlier higher-order beam theory, the theory is updated so that it can represent these effects. The earlier higher-order beam theory will be reviewed, and then an updated finite element formulation for a composite thin-walled beam is set up with explicitly expressed stiffness matrix, mass matrix, and geometric stiffness matrix.

In **Chapter 3**, we present a data-driven approach for the identification of principal cross-sectional deformations of the composite thin-walled beams required for one-dimensional beam finite element analysis. We derive the shape functions of cross-sectional deformations by the principal component analysis using big data consisting of the shell-based static analysis results of a thin-walled beam. Important issues related to the establishment of a well-defined dataset are addressed, and the procedure by which to incorporate the obtained shape functions for a higher-order beam analysis is presented.

In **Chapter 4**, we deal with numerical examples solving static, vibration, and buckling analysis of isotropic and composite thin-walled beams. After verifying the

solution accuracy of the one-dimensional higher-order beam analysis using the data-driven shape functions, we investigate the numerical and data aspects of the present data-driven approach.

In **Chapter 5**, the overall conclusion of this dissertation is presented.

In **Appendix A**, the previous work obtaining shape functions by physical approach will be briefly introduced. The developed approach, a systematic method to derive the sectional shape function reflecting the effects of anisotropic properties and lamination, has formed the base of the research in this thesis.

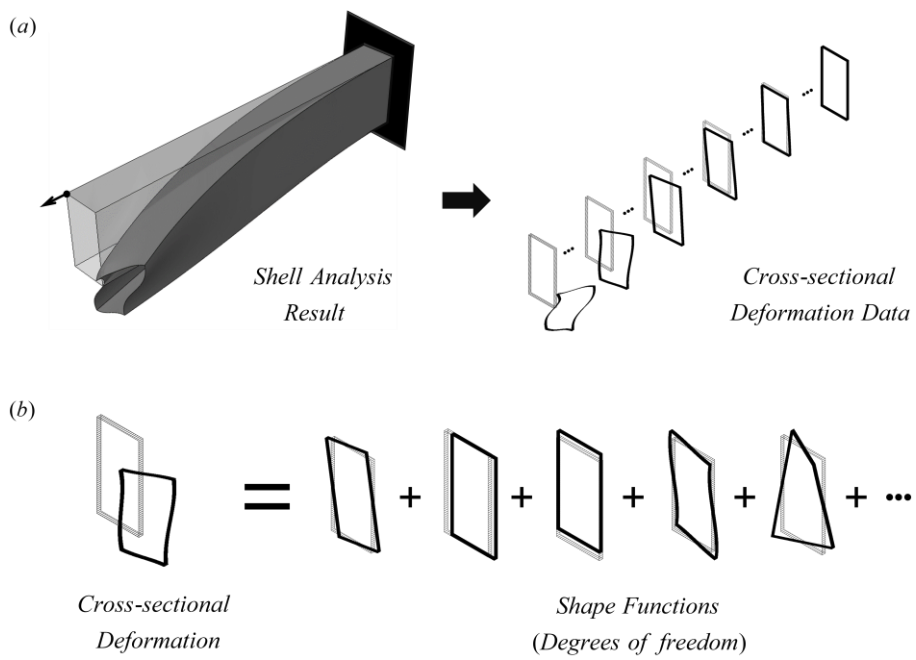


Fig. 1.1 Illustration of (a) cross-sectional deformation data from the shell analysis results and (b) shape functions bases of cross-sectional deformation

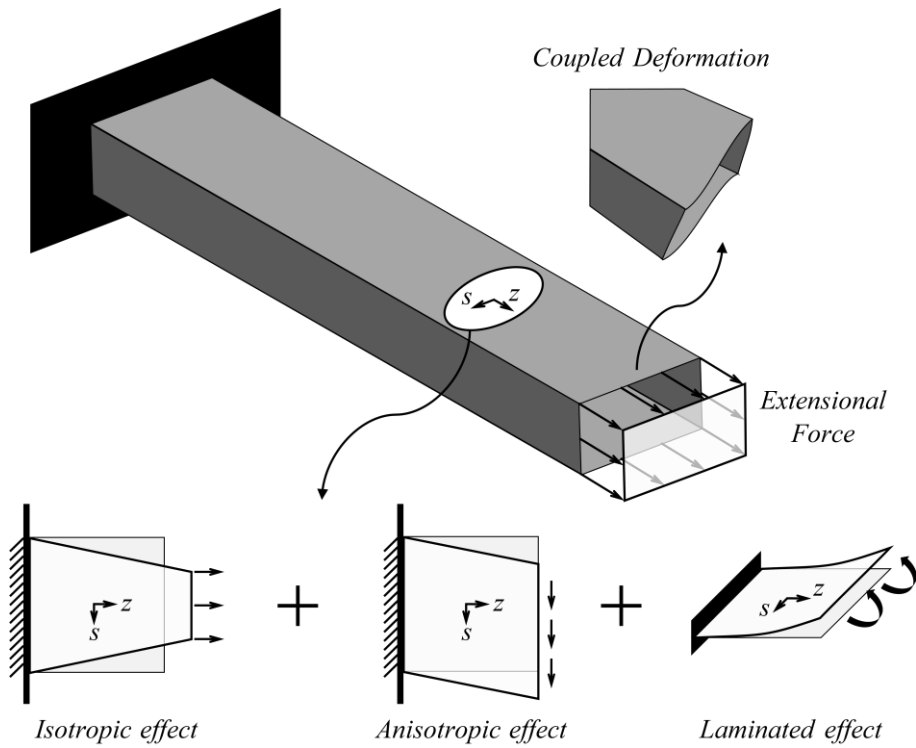


Fig. 1.2 Illustration of the cross-sectional deformation of the composite thin-walled box beam by various effects

CHAPTER 2.

Higher-order beam formulation

2.1 Overview

In this chapter, a one-dimensional higher-order beam theory is developed for an efficient structural analysis of composite thin-walled beams [43]. Because the effects of anisotropic properties and lamination cannot be taken into account in the earlier higher-order beam theory [34-42], the theory is updated so that it can represent these effects. A higher-order beam formulation will be presented in this chapter, while Chapter 3 is devoted to how to define the shape functions using a data-driven approach [71].

In Chapter 2.2, the higher-order beam theory for isotropic thin-walled beam will be reviewed. After establishing the higher-order beam theory for composite thin-walled beams in Chapter 2.3, a finite element formulation based on it is set up with explicitly expressed stiffness matrix, mass matrix, and geometric stiffness matrix in Chapter 2.4.

2.2 Theoretical review: Higher-order beam theory for isotropic thin-walled beam

As shown in Fig. 2.1, the cross-section of the beam consists of several walls and the local coordinate system of n -, s - and z -axes is introduced with its origin at the center of the wall. Because the sectional shape functions in the higher-order beam theory [34-43, 71] depict the deformation patterns of a beam section, they are represented in terms of the displacements ${}^{\xi_i}\psi_\eta$ ($\eta=n, s, z$) as a function of arc-length s where ξ_i is the index representing the i -th degree of freedom. Because ξ_i denotes the axial variation of the one-dimensional deformation measure, it is only a function of z . In terms of ${}^{\xi_i}\psi_\eta$ and ξ_i , the normal (u_n), tangential (u_s), and axial (u_z) displacements along the wall centerline can be expressed as follows:

$$u_\eta(s, z) = \sum_i {}^{\xi_i}\psi_\eta(s)\xi_i(z) \quad (\eta = n, s, z) \quad (2.1)$$

Once the displacement field at the center of the wall is defined as Eq. (2.1), one can derive the corresponding beam finite element using the minimum potential energy principle.

When the shape functions corresponding to degrees of freedom ξ_i are assumed to be defined as ${}^{\xi_i}\psi_\eta$, the normal (u_n), tangential (u_s), and axial (u_z) displacements

along the wall centerline can be expressed. Using u_η ($\eta = n, s, z$) in Eq. (2.1), the three-dimensional displacement ($\tilde{u}_n, \tilde{u}_s, \tilde{u}_z$) at a generic point (n, s, z) can be expressed as

$$\tilde{u}_n(n, s, z) = u_n(s, z) \quad (2.2)$$

$$\tilde{u}_s(n, s, z) = u_s(s, z) - n\dot{u}_n(s, z) \quad (2.3)$$

$$\tilde{u}_z(n, s, z) = u_z(s, z) - nu'_n(s, z), \quad (2.4)$$

where $(\dot{\quad})$ and $(\quad)'$ denote $\partial(\quad)/\partial s$ and $\partial(\quad)/\partial z$, respectively. The terms involved in the differentiation of $u_n(s, z)$ with respect to s and z appear in Eqs. (2.3-2.4) in order to represent the bending effects resulting from the Kirchhoff plate theory.

If the three-dimensional displacement is expressed as Eqs. (2.2-2.4), the strains at a generic point are given by

$$\varepsilon_{ss}(n, s, z) = \dot{\tilde{u}}_s(n, s, z) = \dot{u}_s(s, z) - n\ddot{u}_n(s, z) \quad (2.5)$$

$$\varepsilon_{zz}(n, s, z) = \tilde{u}'_z(n, s, z) = u'_z(s, z) - nu''_n(s, z) \quad (2.6)$$

$$2\varepsilon_{sz}(n, s, z) = \dot{\tilde{u}}_z(n, s, z) + \tilde{u}'_s(n, s, z) = \dot{u}_z(s, z) + u'_s(s, z) - 2n\dot{u}'_n(s, z) \quad (2.7)$$

For isotropic beams with a modulus of elasticity of E , Poisson's ratio ν , and shear modulus G , one can express the stresses using the equation below.

$$\sigma_{ss} = \frac{E}{1-\nu^2}(\varepsilon_{ss} + \nu\varepsilon_{zz}), \quad \sigma_{zz} = \frac{E}{1-\nu^2}(\varepsilon_{zz} + \nu\varepsilon_{ss}), \quad \sigma_{sz} = 2G\varepsilon_{sz} \quad (2.8)$$

Then, the total potential energy of a beam with $z_1 < z < z_2$ is given as

$$\Pi = \frac{1}{2} \int_{z_1}^{z_2} \int_A (\sigma_{ss}\varepsilon_{ss} + \sigma_{zz}\varepsilon_{zz} + 2\sigma_{sz}\varepsilon_{sz}) dA dz - \int_A (\sigma_{zz}\tilde{u}_z + \sigma_{sz}\tilde{u}_s)_{z_1}^{z_2} dA, \quad (2.9)$$

where A is the cross-sectional area of the beam.

2.3 Higher-order beam theory for composite thin-walled beam

Figure 2.1 shows that each wall of the composite thin-walled beam consists of laminates composed of anisotropic plies having different stacking angles. When it comes to a composite thin-walled beam, three conditions have to be updated from the higher-order beam theory for isotropic thin-walled beams to deal with the effects of anisotropic properties and lamination in composite materials.

First, the constitutive relation should be updated.

$$\begin{bmatrix} \sigma_{ss} \\ \sigma_{zz} \\ \sigma_{sz} \end{bmatrix} = \begin{bmatrix} \bar{Q}_{11} & \bar{Q}_{12} & \bar{Q}_{16} \\ \bar{Q}_{21} & \bar{Q}_{22} & \bar{Q}_{26} \\ \bar{Q}_{61} & \bar{Q}_{62} & \bar{Q}_{66} \end{bmatrix} \begin{bmatrix} \varepsilon_{ss} \\ \varepsilon_{zz} \\ 2\varepsilon_{sz} \end{bmatrix} \quad (2.10)$$

In the previous higher-order beam theory, this constitutive relation was limited to isotropic properties, where several coupling terms relating stresses and strains are zero. To deal with composite thin-walled beams, we have to consider the full coupling between stresses and strains in the s - z plane. The specific formulas of coupling terms will not be given here because they are available in existing studies [72].

Second, the total potential energy equation of the thin-walled beam should be updated. In laminated composite, constitutive relation changes along the thickness because the relation depends on the stacking angle of each ply. In other words,

constitutive relation in the total potential energy equation should vary along the thickness in the updated formulation, while it was constant in isotropic materials.

Finally, two-node elements with the Hermite interpolation instead of linear interpolation [34-41] should be used in the finite element formulation, because the influence of the curvature in composite thin-walled beams is more significant than that in isotropic thin-walled beams. The definition of composite high-order elements by applying these conditions is discussed in detail, at Chapter 2.4.

2.4 Higher-order beam finite element formulation

Here, we discuss of deriving the finite element formulation required for the static, vibration and buckling analysis [42] of composite thin-walled beams. The finite element formulation is developed from previous works on the higher-order beam theory. Details can be found followed.

2.4.1 Formulation for static analysis

The finite element equations can be obtained by minimizing Eq. (2.9) [73]. First, the displacement along the centerline, defined as $\mathbf{u}(s, z)$, is interpolated as

$$\mathbf{u}(s, z) = \begin{Bmatrix} u_n \\ u_s \\ u_z \end{Bmatrix} = \begin{bmatrix} \xi_1 \psi_n & \xi_2 \psi_n & \dots & \xi_k \psi_n \\ \xi_1 \psi_s & \xi_2 \psi_s & \dots & \xi_k \psi_s \\ \xi_1 \psi_z & \xi_2 \psi_z & \dots & \xi_k \psi_z \end{bmatrix} \begin{Bmatrix} \xi_1 \\ \xi_2 \\ \dots \\ \xi_k \end{Bmatrix} = \begin{bmatrix} \Psi_n(s) \\ \Psi_s(s) \\ \Psi_z(s) \end{bmatrix} \mathbf{D}(z) = \Psi(s) \mathbf{N}(z) \mathbf{d}, \quad (2.11)$$

where \mathbf{D} is the displacement vector corresponding to the beam degrees of freedom that refer to shape functions defined later, \mathbf{d} is the nodal displacement vector, and \mathbf{N} is the interpolation function matrix, under the assumption that we use k degrees of freedom containing six global deformations. We use two-node elements with the Hermite interpolation because to consider the influence of the curvature in composite thin-walled beams more precisely. The results obtained by the linear and Hermite interpolations are compared in the Appendix.

Using Eq. (2.11), the strain and stress are expressed as

$$\boldsymbol{\varepsilon} = \begin{bmatrix} \varepsilon_{ss} \\ \varepsilon_{zz} \\ 2\varepsilon_{sz} \end{bmatrix} = \begin{bmatrix} -n(\cdot) & (\cdot) & 0 \\ -n(\cdot)' & 0 & (\cdot)' \\ -2n(\cdot)' & (\cdot)' & (\cdot) \end{bmatrix} \boldsymbol{\Psi} \mathbf{N} \mathbf{d} = \mathbf{B} \mathbf{d} \quad (2.12)$$

$$\boldsymbol{\sigma} = \begin{bmatrix} \sigma_{ss} \\ \sigma_{zz} \\ \sigma_{sz} \end{bmatrix} = \begin{bmatrix} \bar{Q}_{11} & \bar{Q}_{12} & \bar{Q}_{16} \\ \bar{Q}_{21} & \bar{Q}_{22} & \bar{Q}_{26} \\ \bar{Q}_{61} & \bar{Q}_{62} & \bar{Q}_{66} \end{bmatrix} \boldsymbol{\varepsilon} = \bar{\mathbf{Q}} \mathbf{B} \mathbf{d}, \quad (2.13)$$

where \mathbf{B} is the strain interpolation matrix, and $\bar{\mathbf{Q}}$ represents the constitutive relationship between the stress and strain. $\bar{\mathbf{Q}}$ matrix becomes a function of n because it is dependent upon the material property and the stacking angle.

Inserting the strain and stress expressions in Eqs. (2.12-2.13) into Eq. (2.9) and minimizing the total potential energy, the stiffness matrix \mathbf{K} and the external nodal load vector \mathbf{R} corresponding to the generalized stress resultants can be defined as

$$\mathbf{K} = \int_{z_1}^{z_2} \int_A \mathbf{B}^T(n, s, z) \bar{\mathbf{Q}}(n) \mathbf{B}(n, s, z) dA dz, \quad (2.14)$$

and

$$\mathbf{R} = \{\mathbf{F}_1 \quad \mathbf{F}'_1 \quad \mathbf{F}_2 \quad \mathbf{F}'_2\}^T, \quad (2.15)$$

with

$$\mathbf{F} = \begin{Bmatrix} F_{\xi_1} \\ F_{\xi_2} \\ \dots \\ F_{\xi_k} \end{Bmatrix} = \begin{bmatrix} \int_A (\sigma_{sz}^{\xi_1} \psi_s + \sigma_{zz}^{\xi_1} \psi_z) dsdn \\ \int_A (\sigma_{sz}^{\xi_2} \psi_s + \sigma_{zz}^{\xi_2} \psi_z) dsdn \\ \dots \\ \int_A (\sigma_{sz}^{\xi_k} \psi_s + \sigma_{zz}^{\xi_k} \psi_z) dsdn \end{bmatrix} \quad (2.16)$$

In Eq. (2.16), the subscripts 1 and 2 are associated with the node numbers of the two-node element, and the axial derivatives, \mathbf{F}' , in the z -direction are needed as nodal variables because Hermite interpolation is used. The forces acting on the nodes of the shell model can also be rewritten in the higher-order beam formula by imposing that the virtual work expressed in the shell model is equal to that in the beam model. Details can be found in the literature [36].

Finally, it becomes possible to express the finite element equation

$$\mathbf{Kd} = \mathbf{R} \quad (2.17)$$

2.4.2 Formulation for vibration analysis

The mass matrix \mathbf{M} can also be defined similarly [73],

$$\mathbf{M} = \int_{z_1}^{z_2} \int_A \mathbf{N}^T \boldsymbol{\Psi}^T \rho \boldsymbol{\Psi} \mathbf{N} dA dz, \quad (2.18)$$

where ρ is the density. Finally, it becomes possible to express the finite element equation for eigenvalue or free vibration problems as

$$\mathbf{Kd} - \omega^2 \mathbf{Md} = \mathbf{0}, \quad (2.19)$$

where ω is the angular frequency.

2.4.3 Formulation for buckling analysis

To consider buckling behavior, the geometric nonlinear strains should be considered [42]. Geometric nonlinear strains, expressed in terms of the von Kármán strain, are defined as follows:

$$\bar{\varepsilon}_{ss}(n, s, z) = \frac{\dot{u}_n^2 + \dot{u}_z^2}{2} = \frac{\dot{u}_n^2 + (\dot{u}_z - n\dot{u}'_n)^2}{2} \quad (2.20)$$

$$\bar{\varepsilon}_{zz}(n, s, z) = \frac{\tilde{u}_n'^2 + \tilde{u}_s'^2}{2} = \frac{u_n'^2 + (u_s' - nu_n')^2}{2} \quad (2.21)$$

$$2\bar{\varepsilon}_{sz}(n, s, z) = \dot{u}_n \tilde{u}'_n = \dot{u}_n u'_n \quad (2.22)$$

The geometric nonlinear strain fields are combined with the pre-buckling stress fields to calculate the work performed by buckling. The work performed by the nonlinear strain is defined as follows:

$$\Pi_b = -\int_V \Lambda \left\{ \bar{\sigma}_{ss} \bar{\varepsilon}_{ss} + \bar{\sigma}_{zz} \bar{\varepsilon}_{zz} + 2\bar{\sigma}_{sz} \bar{\varepsilon}_{sz} \right\} dV = -\int_V \Lambda \bar{\boldsymbol{\sigma}} \cdot \bar{\boldsymbol{\varepsilon}} dV \quad (2.23)$$

In Eq. (2.23), Λ , $\bar{\boldsymbol{\sigma}}$, and $\bar{\boldsymbol{\varepsilon}}$ denote the buckling load scale factor, pre-buckling stress vector, and geometric nonlinear strain vector, respectively. The pre-buckling stress vector $\bar{\boldsymbol{\sigma}}$ is calculated as

$$\bar{\boldsymbol{\sigma}} = \bar{\mathbf{Q}}\boldsymbol{\varepsilon}(\bar{\mathbf{d}}), \quad (2.24)$$

where $\bar{\mathbf{d}}$ denotes the vector of deformation calculated by a linear static analysis in Eq. (2.17) for the given loading and boundary condition. When we consider the finite element for the discretized geometric nonlinear strain, Eqs. (2.20-2.22) are obtained in discretized form:

$$\begin{aligned} \bar{\boldsymbol{\varepsilon}} &= \frac{1}{2} \left\{ \begin{array}{l} \mathbf{U}^T \left[\mathbf{N}^T \dot{\boldsymbol{\Psi}}_n^T \boldsymbol{\Psi}_n \mathbf{N} + (\mathbf{N}^T \dot{\boldsymbol{\Psi}}_z^T - n \mathbf{N}'^T \dot{\boldsymbol{\Psi}}_n^T) (\boldsymbol{\Psi}_z \mathbf{N} - n \boldsymbol{\Psi}_n \mathbf{N}') \right] \mathbf{U} \\ \mathbf{U}^T \left[\mathbf{N}'^T \boldsymbol{\Psi}_n^T \boldsymbol{\Psi}_n \mathbf{N}' + (\mathbf{N}'^T \boldsymbol{\Psi}_s^T - n \mathbf{N}'^T \dot{\boldsymbol{\Psi}}_n^T) (\boldsymbol{\Psi}_s \mathbf{N}' - n \dot{\boldsymbol{\Psi}}_n \mathbf{N}') \right] \mathbf{U} \\ \mathbf{U}^T (\mathbf{N}^T \dot{\boldsymbol{\Psi}}_n^T \boldsymbol{\Psi}_n \mathbf{N}' + \mathbf{N}'^T \boldsymbol{\Psi}_n^T \dot{\boldsymbol{\Psi}}_n \mathbf{N}) \mathbf{U} \end{array} \right\} \\ &= \frac{1}{2} \left\{ \begin{array}{l} \mathbf{U}^T \mathbf{B}_{ss} \mathbf{U} \\ \mathbf{U}^T \mathbf{B}_{zz} \mathbf{U} \\ \mathbf{U}^T \mathbf{B}_{sz} \mathbf{U} \end{array} \right\} \end{aligned} \quad (2.25)$$

The geometric stiffness matrix, \mathbf{G} , can then be defined as

$$\mathbf{G} = \int_V \left\{ \bar{\sigma}_{ss} \mathbf{B}_{ss} + \bar{\sigma}_{zz} \mathbf{B}_{zz} + \bar{\sigma}_{sz} \mathbf{B}_{sz} \right\} dV \quad (2.26)$$

Finally, one can express the finite element equation as

$$\mathbf{Kd} + \Lambda \mathbf{Gd} = \mathbf{0} \quad (2.27)$$

By multiplying the prescribed unit load and critical scale factor calculated from Eq. (2.27), the critical load can be obtained,

$$P_{cr} = \Lambda P, \quad (2.28)$$

where P denotes the prescribed unit load corresponding to the given loading condition. More details about the buckling formulation can be found in an earlier study [42].

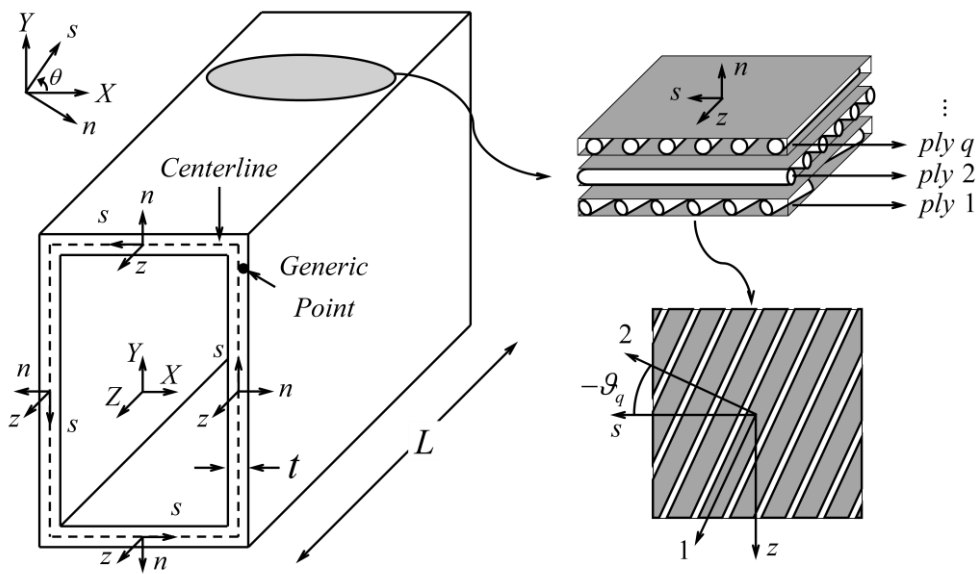


Fig. 2.1 Coordinate system used for the analysis of the composite thin-walled beam and geometric parameters

CHAPTER 3.

Data-driven approach for deriving shape functions of composite thin-walled beams

3.1 Overview

In this chapter, we derive the shape functions of cross-sectional deformations through data processing using the shell-based static analysis results of a thin-walled beam [71]. We perform a principal component analysis during the data processing step, in which the desired shape functions are obtained without any specific assumptions on the behavior of cross-sectional deformations. Important issues related to the establishment of a well-defined dataset are addressed, and the procedure by which to incorporate the obtained shape functions for a higher-order beam analysis is presented. The overall process is sketched in Figs. 3.1-3.4 and a detailed explanation of it will be presented below.

3.2 Preparing cross-sectional deformation big data

In a data-driven analysis, it is most important to obtain well-defined cross-sectional deformation data (CSD data) to be used to derive the shape functions. As suggested in Fig. 3.1, we consider cantilevered beams to collect CSD data. A shell model of a cantilevered beam is uniformly meshed along the beam axial direction, and we collect the beam deformations obtained over the axial coordinates as the CSD data.

Chapter 3.2.1 introduces the CSD data required for isotropic materials or certain composite materials. Chapter 3.2.2 deals with the additional issues involved in obtaining the CSD data required for generally laminated composites.

3.2.1 Cross-sectional deformation data required for isotropic materials or a certain composite

When generating the CSD data for a thin-walled beam consist of isotropic materials or a specific composite, the sectional geometry information and material properties of the shell model are identical to those of the target beam model, and several different loading conditions are considered. Among other factors, it is most important to choose the proper beam length and loading conditions. Concerning these issues, the following strategies are taken.

- The beam length is approximately five times the sections height. With this length, sectional deformations affected by end effects can be correctly captured
- For loading, we consider not only uniformly distributed forces over the beam cross-section but also shell nodal forces over all of the shell nodes of the beam cross-section at the beam end

To apply the uniformly distributed forces, which will be called the general beam force, all shell nodes lying on the section of the beam free end are rigidly coupled to the center of gravity of those nodes so that the section moves as if it were a rigid cross-section. Three resultant forces and three resultant moments are applied at the center of gravity. It has been shown [39] that the resultant beam force loading generates cross-sectional deformation due to Poisson's effect and shear deformation. About the shell nodal forces, forces in three independent directions are applied at all nodal points of the beam end section. With these loads, local sectional deformations will be effectively induced. To avoid overestimating particular deformation patterns from a specific load, the beam deformation due to each load is normalized to ensure equal overall compliance measures of the beam.

To form an array of CSD data for the principal component analysis, the deformations of all cross-sections of the cantilevered beam under all selected loading cases are collected. If the beam is divided into N_d cross-sections along its

axial direction and the total number of load cases is $N_l=6+3m$ (m : the number of the nodes used to discretize the beam cross-section in the shell model), the total number of CSD data instances is $N=N_d \times N_l$. The i -th cross-sectional deformation is stored as the column vector \underline{S}_i such that

$$\underline{S}_i = [{}^1d_X \ {}^2d_X \ \dots \ {}^m d_X \ {}^1d_Y \ {}^2d_Y \ \dots \ {}^m d_Y \ {}^1d_Z \ {}^2d_Z \ \dots \ {}^m d_Z]_i^T \quad (i=1,2,\dots,N) \quad (3.1)$$

Each value of d_X , d_Y , and d_Z is a nodal displacement component of the shell model in the global Cartesian coordinates (X, Y, Z). Accordingly, the vector \underline{S}_i contains $3m$ components.

One can store \underline{S}_1 to \underline{S}_N as a matrix \mathbf{U} for the subsequent process:

$$\mathbf{U} = [\underline{S}_1 \ \underline{S}_2 \ \dots \ \underline{S}_N]^T \quad (3.2)$$

3.2.2 Cross-sectional deformation data required for general composites

Assuming that plies of each wall have circumferentially uniform stiffness (CUS) with the same angle in this study, composite thin-walled beams have two design variables. The first is the rotation angle of the plies and the second is the laminated sequences. Combining these design variables yields an infinite number of thin-walled beam models so that different cross-sectional deformations occur for the

same cross-section. Here, we discuss securing the cross-section deformation data necessary to represent the sectional deformations of composite thin-walled beams laminated with randomly oriented plies.

As addressed in the previous study on composite thin-walled box beam [43], the effect of the rotation angle induces the coupling between the stress and strain. If we consider Eq. (2.10) in more detail, the constitutive equation can be defined as following when the ply orientation 1-2 is equal to the s - z plane ($\vartheta = 0^\circ$ in Fig. 2.1) [72].

$$\begin{Bmatrix} \sigma_{ss} \\ \sigma_{zz} \\ \sigma_{sz} \end{Bmatrix} = \begin{bmatrix} \frac{E_1}{1-\nu_{12}\nu_{21}} & \frac{\nu_{12}E_2}{1-\nu_{12}\nu_{21}} & 0 \\ \frac{\nu_{12}E_2}{1-\nu_{12}\nu_{21}} & \frac{E_2}{1-\nu_{12}\nu_{21}} & 0 \\ 0 & 0 & G_{12} \end{bmatrix} \begin{Bmatrix} \varepsilon_{ss} \\ \varepsilon_{zz} \\ \varepsilon_{sz} \end{Bmatrix} = \mathbf{Q} \begin{Bmatrix} \varepsilon_{ss} \\ \varepsilon_{zz} \\ \varepsilon_{sz} \end{Bmatrix} \quad (3.3)$$

When the ply rotates at angle ϑ , the constitutive equation varies as

$$\begin{Bmatrix} \sigma_{ss} \\ \sigma_{zz} \\ \sigma_{sz} \end{Bmatrix} = \mathbf{T}_\sigma^{-1} \mathbf{Q} \mathbf{T}_\varepsilon \begin{Bmatrix} \varepsilon_{ss} \\ \varepsilon_{zz} \\ \varepsilon_{sz} \end{Bmatrix} = \bar{\mathbf{Q}} \begin{Bmatrix} \varepsilon_{ss} \\ \varepsilon_{zz} \\ \varepsilon_{sz} \end{Bmatrix}, \quad (3.4)$$

where

$$\mathbf{T}_\sigma = \begin{bmatrix} \cos^2 \vartheta & \sin^2 \vartheta & 2\cos \vartheta \sin \vartheta \\ \sin^2 \vartheta & \cos^2 \vartheta & -2\cos \vartheta \sin \vartheta \\ -\cos \vartheta \sin \vartheta & \cos \vartheta \sin \vartheta & \cos^2 \vartheta - \sin^2 \vartheta \end{bmatrix}, \quad (3.5)$$

and

$$\mathbf{T}_\varepsilon = \begin{bmatrix} \cos^2 \vartheta & \sin^2 \vartheta & \cos \vartheta \sin \vartheta \\ \sin^2 \vartheta & \cos^2 \vartheta & -\cos \vartheta \sin \vartheta \\ -2\cos \vartheta \sin \vartheta & 2\cos \vartheta \sin \vartheta & \cos^2 \vartheta - \sin^2 \vartheta \end{bmatrix} \quad (3.6)$$

The mathematical expressions of the $\bar{\mathbf{Q}}$ matrix can be obtained as a function of ϑ , whereas obtaining this expression by the analysis results requires a sufficient database to take into account. The more databases there are, the more likely it is to predict the behavior at different angles, but there is a limit because dealing with all of the continuous variables is impossible. The constitutive equations defined above are revised in form as follows [74] to overcome this problem.

$$\bar{\mathbf{Q}} = \mathbf{Q}_1 + \mathbf{Q}_2 \sin 2\vartheta + \mathbf{Q}_3 \sin 4\vartheta + \mathbf{Q}_4 \cos 2\vartheta + \mathbf{Q}_5 \cos 4\vartheta \quad (3.7)$$

where

$$\mathbf{Q}_1 = \begin{bmatrix} Q_A & Q_D & 0 \\ Q_D & Q_A & 0 \\ 0 & 0 & Q_E \end{bmatrix} \quad (3.8)$$

$$\mathbf{Q}_2 = \begin{bmatrix} 0 & 0 & Q_B/2 \\ 0 & 0 & Q_B/2 \\ Q_B/2 & Q_B/2 & 0 \end{bmatrix} \quad (3.9)$$

$$\mathbf{Q}_3 = \begin{bmatrix} 0 & 0 & Q_C \\ 0 & 0 & -Q_C \\ Q_C & -Q_C & 0 \end{bmatrix} \quad (3.10)$$

$$\mathbf{Q}_4 = \begin{bmatrix} Q_B & 0 & 0 \\ 0 & -Q_B & 0 \\ 0 & 0 & 0 \end{bmatrix} \quad (3.11)$$

$$\mathbf{Q}_5 = \begin{bmatrix} Q_C & -Q_C & 0 \\ -Q_C & Q_C & 0 \\ 0 & 0 & -Q_C \end{bmatrix}, \quad (3.12)$$

where

$$Q_A = (3Q_{11} + 3Q_{22} + 2Q_{12} + 4Q_{66}) / 8 \quad (3.13)$$

$$Q_B = (Q_{11} - Q_{22}) / 2 \quad (3.14)$$

$$Q_C = (Q_{11} + Q_{22} - 2Q_{12} - 4Q_{66}) / 8 \quad (3.15)$$

$$Q_D = (Q_{11} + Q_{22} + 6Q_{12} - 4Q_{66}) / 8 \quad (3.16)$$

$$Q_E = (Q_{11} + Q_{22} - 2Q_{12} + 4Q_{66}) / 8 \quad (3.17)$$

We can find that the $\bar{\mathbf{Q}}$ matrix can be separated into five orthogonal bases related to \mathcal{G} . By considering these bases, we infer that more than five angles related to 1, $\sin 2\mathcal{G}$, $\sin 4\mathcal{G}$, $\cos 2\mathcal{G}$, $\cos 4\mathcal{G}$ is required to represent the constitutive relationship design space. Here, we assumed that the constitutive equation information varying according to \mathcal{G} could be represented if the determinant of the matrix below, consist of five angles $\mathcal{G}_1 - \mathcal{G}_5$, is nonzero.

$$\begin{vmatrix} 1 & \sin 2\mathcal{G}_1 & \sin 4\mathcal{G}_1 & \cos 2\mathcal{G}_1 & \cos 4\mathcal{G}_1 \\ 1 & \sin 2\mathcal{G}_2 & \sin 4\mathcal{G}_2 & \cos 2\mathcal{G}_2 & \cos 4\mathcal{G}_2 \\ 1 & \sin 2\mathcal{G}_3 & \sin 4\mathcal{G}_3 & \cos 2\mathcal{G}_3 & \cos 4\mathcal{G}_3 \\ 1 & \sin 2\mathcal{G}_4 & \sin 4\mathcal{G}_4 & \cos 2\mathcal{G}_4 & \cos 4\mathcal{G}_4 \\ 1 & \sin 2\mathcal{G}_5 & \sin 4\mathcal{G}_5 & \cos 2\mathcal{G}_5 & \cos 4\mathcal{G}_5 \end{vmatrix} \neq 0 \quad (3.18)$$

For this purpose, five angles $[-45^\circ]$, $[-22.5^\circ]$, $[0^\circ]$, $[22.5^\circ]$ and $[45^\circ]$ of the equal interval were selected for $\mathcal{G}_1 - \mathcal{G}_5$. The example in Chapter 4.3 verifies the validity

of the assumption.

Besides, as addressed in the previous study on composite thin-walled box beams [43], the effect of the lamination induces the coupling between the stress and curvature. This issue should also be taken into account. However, assuming that the plate bending results from the shell nodal forces represents more general curvature deformations, it had not been further considered. Finally, if the beam is divided into N_d cross-sections along its axial direction and the total number of load cases is $N_l=6+3m$ as addressed in Chapter 3.2.1, the total number of CSD data for general composite thin-walled beam instances becomes $N=5 \times N_d \times N_l$.

3.3 Pre-process of cross-sectional deformation data

The amounts of CSD data from the general beam force and the shell nodal force loading are entirely different. To take their contributions equally into account in the principal component analysis, we scale $\underline{\tilde{S}}_i$ from the shell nodal force by a factor of $6/3m$, where 6 and $3m$ correspond to the load cases of the general beam force and the shell nodal force, respectively. Accordingly, $\underline{\tilde{S}}_i$ is redefined as follows:

$$\begin{aligned}\tilde{S}_i &= \underline{\tilde{S}}_i && \text{(CSD from general beam force)} \\ \tilde{S}_i &= \frac{6}{3m} \underline{\tilde{S}}_i && \text{(CSD from shell nodal force)}\end{aligned}\tag{3.19}$$

Thus, we can form the matrix $\bar{\mathbf{U}}$.

$$\bar{\mathbf{U}} = [\tilde{S}_1 \ \tilde{S}_2 \ \dots \ \tilde{S}_N]^T\tag{3.20}$$

Because six rigid-body motions of the beam cross-section are naturally included in the beam analysis, we remove the rigid-body components from \tilde{S}_i by means of orthogonalization and introduce $\bar{\underline{\tilde{S}}}_i$ and $\bar{\mathbf{U}}$, which are defined as

$$\bar{\underline{\tilde{S}}}_i = \tilde{S}_i - \sum_{j=1}^6 \frac{\tilde{S}_i \cdot \mathbf{R}_j}{\mathbf{R}_j \cdot \mathbf{R}_j} \mathbf{R}_j\tag{3.21}$$

$$\bar{\mathbf{U}} = [\bar{\underline{\tilde{S}}}_1 \ \bar{\underline{\tilde{S}}}_2 \ \dots \ \bar{\underline{\tilde{S}}}_N]^T,\tag{3.22}$$

where \mathbf{R}_j ($j=1, 2, \dots, 6$) denotes the rigid-body motions of the cross-section on the assumption of a small amount of deformation.

Based on the higher-order beam theory requiring the bases of the sectional deformations, the in-plane (distortion) and out-of-plane (warping) deformations are considered to be independent deformation patterns. Therefore, it is useful to decouple $\bar{\underline{S}}_i$ into the vector $\bar{\underline{S}}_i^{XY}$ consisting only of its in-plane nodal displacement values and $\bar{\underline{S}}_i^Z$ consisting only of its out-of-plane nodal displacement values. We also considered deformation in the opposite direction to take into account the reverse loading case, because the principal component analysis is facilitated if the average of the entire CSD data matrix is zero. We finally obtained the following preprocessed matrix $\bar{\bar{\underline{U}}}$, which is $4N \times 3m$ in size.

$$\bar{\bar{\underline{U}}} = \left[\bar{\underline{S}}_1^{XY} \quad \bar{\underline{S}}_2^{XY} \quad \dots \quad \bar{\underline{S}}_N^{XY} \quad \bar{\underline{S}}_1^Z \quad \bar{\underline{S}}_2^Z \quad \dots \quad \bar{\underline{S}}_N^Z \quad -\bar{\underline{S}}_1^{XY} \quad -\bar{\underline{S}}_2^{XY} \quad \dots \quad -\bar{\underline{S}}_N^{XY} \quad -\bar{\underline{S}}_1^Z \quad -\bar{\underline{S}}_2^Z \quad \dots \quad -\bar{\underline{S}}_N^Z \right]^T \quad (3.23)$$

3.4 Data-driven analysis for obtaining principal cross-sectional deformations

The principal component analysis finds new base axes that are orthogonal to each other while maximizing the variances along the axes. In other words, it determines the principal factors by obtaining vectors with large variance. Each instance of the preprocessed CSD data uses $3m$ -dimensional information to represent section deformation.

For the principal component analysis, we consider a unit vector \underline{e} of length $3m$.

$$\underline{e} \cdot \underline{e} = \underline{e}^T \underline{e} = 1 \quad (3.24)$$

The variance of the $\bar{\underline{U}}$ data projected onto \underline{e} can be written as follows:

$$Var(\bar{\underline{U}}_{\underline{e}}) = \frac{\sum (\bar{\underline{U}}_{\underline{e}} - E(\bar{\underline{U}}_{\underline{e}}))^2}{(4N - 1)} \quad (3.25)$$

Because the mean of the projected value is zero, the variance is given merely by

$$Var(\bar{\underline{U}}_{\underline{e}}) = \frac{\underline{e}^T \bar{\underline{U}} \bar{\underline{U}}_{\underline{e}}}{(4N - 1)} = \underline{e}^T \underline{\Sigma} \underline{e}, \quad (3.26)$$

where $\underline{\Sigma}$ corresponds to the covariance matrix.

To solve the variance maximization problem, we introduce that the Lagrangian L with the Lagrange multiplier λ .

$$L = \underline{e}^T \underline{\Sigma} \underline{e} - \lambda (\underline{e}^T \underline{e} - 1) \quad (3.27)$$

$$\frac{\partial L}{\partial \underline{e}} = 2\underline{\Sigma}\underline{e} - 2\lambda\underline{e} = 2(\underline{\Sigma} - \lambda\underline{I})\underline{e} = 0 \quad (3.28)$$

Here, λ becomes the eigenvalue of the covariance matrix $\underline{\Sigma}$, and the unit vector \underline{e} becomes the eigenvector corresponding to the principal component. A larger eigenvalue corresponds to a more critical principal component. In this study, we define these principal components as the principal cross-sectional deformations and define shape functions based on them. It is expected that $3m$ -dimensional information can be well represented by a small number of principal cross-sectional deformations.

3.5 Post-process required for defining shape functions.

The obtained principal components represent the sectional deformation in a nodal vector form of the shell model. The obtained principal component $\underline{\mathbf{P}}_{\xi_i}$ ($i=1,2,\dots,k$) will be associated with the i -th degree of freedom ξ_i , under the assumption that we use k principal components containing six global deformations. It contains the nodal displacement of a section in the following order.

$$\underline{\mathbf{P}}_{\xi_i} = [{}^1d_X \quad {}^2d_X \quad \dots \quad {}^m d_X \quad {}^1d_Y \quad {}^2d_Y \quad \dots \quad {}^m d_Y \quad {}^1d_Z \quad {}^2d_Z \quad \dots \quad {}^m d_Z]_{\xi_i}^T \quad (3.29)$$

Note that we associate $\underline{\mathbf{P}}_{\xi_1}$ to $\underline{\mathbf{P}}_{\xi_6}$ with the rigid-body motions $\underline{\mathbf{R}}_1$ to $\underline{\mathbf{R}}_6$, while $\underline{\mathbf{P}}_{\xi_i}$ ($i \geq 7$) corresponds to sectional deformations free from rigid-body motions (warping, distortion) obtained from the principal component analysis. While $\underline{\mathbf{P}}_{\xi_i}$ is explicitly written according to the displacements of the nodes discretizing the cross-section in the global coordinate, we should express these values in the local beam edge coordinate (n, s, z) using the coordinate transformation by the rotation angle θ (the angle between the s -axis and the X -axis at each edge) on the X - Y or n - s plane. This relationship is expressed simply as shown below.

$$\begin{bmatrix} d_n \\ d_s \\ d_z \end{bmatrix}_{\xi_i} = \begin{bmatrix} \sin \theta & -\cos \theta & 0 \\ \cos \theta & \sin \theta & 0 \\ 0 & 0 & 1 \end{bmatrix} \begin{bmatrix} d_X \\ d_Y \\ d_Z \end{bmatrix}_{\xi_i} \quad (3.30)$$

Because the higher-order beam theory uses the functional form $\xi_i \psi_\eta(s)$, as in Eq.

(2.1), the discrete data represented by \mathbf{P}_{ξ_i} will be converted into the following polynomial:

$$\xi_i \psi_\eta(s) = \xi_i a_0 s^0 + \xi_i a_1 s^1 + \dots + \xi_i a_\beta s^\beta \quad (3.31)$$

The highest order β will be determined in the process of determining the unknown coefficients $\xi_i a_0$ to $\xi_i a_\beta$. Note that the interpolation in Eq. (3.31) is performed independently for each edge of the beam cross-section. If the data from \mathbf{P}_{ξ_i} is available at α nodes for each edge, the following relationship can be written (we defined s -axis coordinate values for the α nodes at an edge as $s_1, s_2, \dots, s_\alpha$).

$$\begin{bmatrix} d_\eta(s_1) \\ d_\eta(s_2) \\ \dots \\ d_\eta(s_\alpha) \end{bmatrix}_{\xi_i} = \begin{bmatrix} s_1^0 & s_1^1 & \dots & s_1^\beta \\ s_2^0 & s_2^1 & \dots & s_2^\beta \\ \dots & \dots & \dots & \dots \\ s_\alpha^0 & s_\alpha^1 & \dots & s_\alpha^\beta \end{bmatrix} \begin{bmatrix} \xi_i a_0 \\ \xi_i a_1 \\ \dots \\ \xi_i a_\beta \end{bmatrix} + \begin{bmatrix} e_1 \\ e_2 \\ \dots \\ e_\alpha \end{bmatrix} = \begin{bmatrix} \xi_i \psi_\eta(s_1) \\ \xi_i \psi_\eta(s_2) \\ \dots \\ \xi_i \psi_\eta(s_\alpha) \end{bmatrix} + \begin{bmatrix} e_1 \\ e_2 \\ \dots \\ e_\alpha \end{bmatrix} \quad (3.32)$$

In Eq. (3.32), e_1, e_2, \dots , and e_α denote errors between the nodal displacements extracted from \mathbf{P}_{ξ_i} and the corresponding values obtained from the polynomial shape function in Eq. (3.31). Because the displacements at the corner nodes (s_1 and s_α) for one edge must be equal to those at the corner nodes of the adjacent edges, $\xi_i \psi_\eta(s_1)$ and $\xi_i \psi_\eta(s_\alpha)$ must be identical to $d_\eta(s_1)$ and $d_\eta(s_\alpha)$, respectively, implying that $e_1 = 0$ and $e_\alpha = 0$. These two conditions allow us to express $\xi_i a_0$ and $\xi_i a_1$ in terms of the remaining coefficients $\xi_i a_2$ to $\xi_i a_\beta$ as

follows:

$$\begin{bmatrix} \xi_i \\ \eta \\ a_0 \end{bmatrix} = \begin{bmatrix} s_1^0 & s_1^1 \\ s_\alpha^0 & s_\alpha^1 \end{bmatrix}^{-1} \begin{bmatrix} d_\eta(s_1) \\ d_\eta(s_\alpha) \end{bmatrix}_{\xi_i} - \begin{bmatrix} s_1^0 & s_1^1 \\ s_\alpha^0 & s_\alpha^1 \end{bmatrix}^{-1} \begin{bmatrix} s_1^2 & s_1^3 & \dots & s_1^\beta \\ s_\alpha^2 & s_\alpha^3 & \dots & s_\alpha^\beta \end{bmatrix} \begin{bmatrix} \xi_i \\ \eta \\ a_2 & \xi_i \\ \eta \\ a_3 & \dots & \xi_i \\ \eta \\ a_\beta \end{bmatrix}^T \quad (3.33)$$

The coefficients $\xi_i a_2$ to $\xi_i a_\beta$ can be determined by a regression analysis,

yielding

$$\begin{bmatrix} \xi_i \\ \eta \\ a_2 & \xi_i \\ \eta \\ a_3 & \dots & \xi_i \\ \eta \\ a_\beta \end{bmatrix}^T = (\mathbf{X}^T \mathbf{X})^{-1} \mathbf{X}^T \mathbf{Y} \quad (3.34)$$

$$\mathbf{X} = \begin{bmatrix} s_1^2 & s_1^3 & \dots & s_1^\beta \\ s_2^2 & s_2^3 & \dots & s_2^\beta \\ \dots & \dots & \dots & \dots \\ s_\alpha^2 & s_\alpha^3 & \dots & s_\alpha^\beta \end{bmatrix} - \begin{bmatrix} s_1^0 & s_1^1 \\ s_2^0 & s_2^1 \\ \dots & \dots \\ s_\alpha^0 & s_\alpha^1 \end{bmatrix} \begin{bmatrix} s_1^0 & s_1^1 \\ s_\alpha^0 & s_\alpha^1 \end{bmatrix}^{-1} \begin{bmatrix} s_1^2 & s_1^3 & \dots & s_1^\beta \\ s_\alpha^2 & s_\alpha^3 & \dots & s_\alpha^\beta \end{bmatrix} \quad (3.35)$$

$$\mathbf{Y} = \begin{bmatrix} d_\eta(s_1) \\ d_\eta(s_2) \\ \dots \\ d_\eta(s_\alpha) \end{bmatrix}_{\xi_i} - \begin{bmatrix} s_1^0 & s_1^1 \\ s_2^0 & s_2^1 \\ \dots & \dots \\ s_\alpha^0 & s_\alpha^1 \end{bmatrix} \begin{bmatrix} s_1^0 & s_1^1 \\ s_\alpha^0 & s_\alpha^1 \end{bmatrix}^{-1} \begin{bmatrix} d_\eta(s_1) \\ d_\eta(s_\alpha) \end{bmatrix}_{\xi_i} \quad (3.36)$$

The use of low-order polynomials (with $\beta \geq 2$) is preferred for the regression analysis, and the value of β is so chosen as to satisfy the following error criterion,

$$\min\left(\frac{\sum_{j=1}^{\alpha} |e_j|}{\alpha}, \frac{\sum_{j=1}^{\alpha} (d_\eta(s_j) - \xi_i \psi_\eta(s_j))^2}{\sum_{j=1}^{\alpha} (d_\eta(s_j) - \bar{d}_\eta)^2}\right) < \delta, \quad (3.37)$$

where the first term in the parentheses represents the mean error over all nodes and

the second term represents the explained sum of squares (SSE) over the total sum of squares (SST). The symbol \bar{d}_η denotes the average of the d_η values. The parameter δ is set to $\delta = 10^{-2}$ for $\eta = s$ and z and to $\delta = 10^{-4}$ for $\eta = n$. By conducting the regression analysis for all displacement components at all edges, all shape functions are explicitly determined as polynomial functions of s .

Preparing Big Data

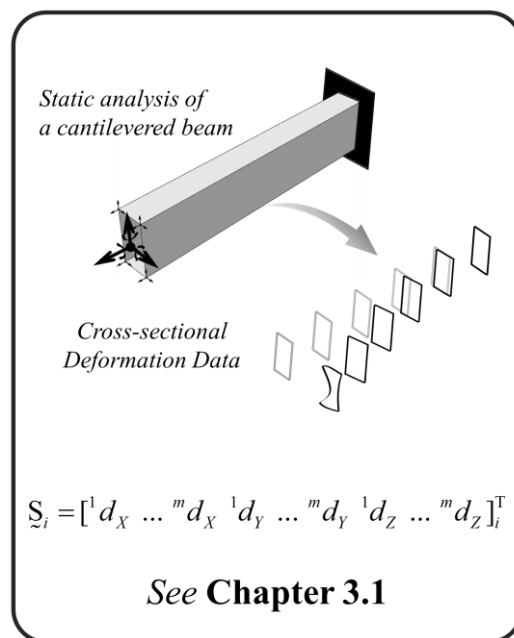


Fig. 3.1 The procedure used to obtain data-driven shape functions corresponding to the higher-order degrees of freedom. First step: *Preparing Big Data*

Pre-processing

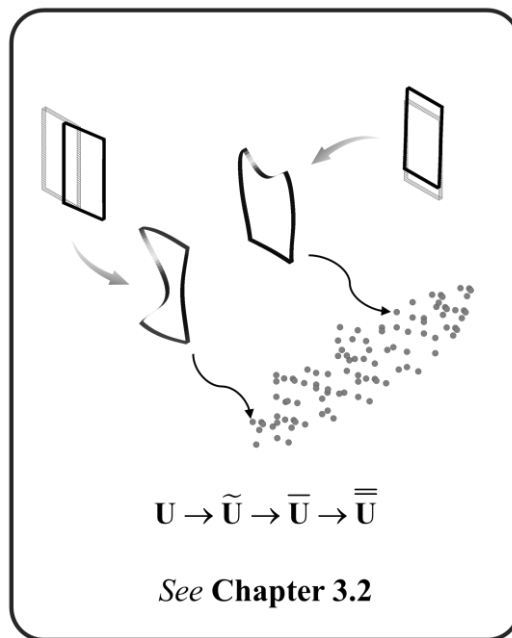


Fig. 3.2 The procedure used to obtain data-driven shape functions corresponding to the higher-order degrees of freedom. Second step: *Pre-processing*

Principal Component Analysis

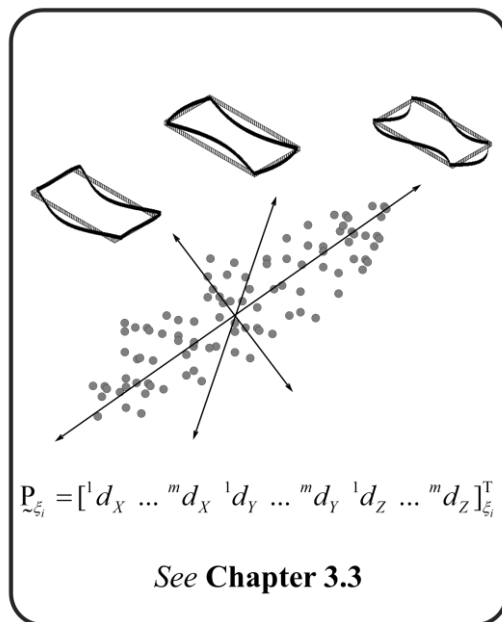


Fig. 3.3 The procedure used to obtain data-driven shape functions corresponding to the higher-order degrees of freedom. Third step: *Principal Component Analysis*

Post-processing

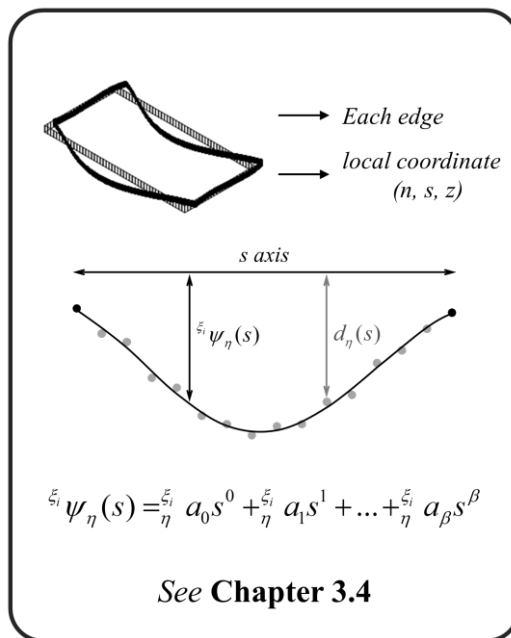


Fig. 3.4 The procedure used to obtain data-driven shape functions corresponding to the higher-order degrees of freedom. Last step: *Post-processing*

CHAPTER 4.

Numerical examples and discussions

4.1 Overview

In this chapter, we deal with numerical examples solving static, vibration, and buckling analysis of thin-walled beams. In Chapter 4.2, we discuss numerical examples related to isotropic thin-walled beams. We verify the solution accuracy of the one-dimensional higher-order beam analysis using the data-driven shape functions by comparing the present results against the ABAQUS shell finite element analysis results. Also, we investigate the numerical aspects of the present data-driven approach.

Then, in Chapter 4.3, we check the analysis results on composite thin-walled beams. As like in Chapter 4.2, we deal with additional numerical and data issues when it comes to a composite beam, after verifying the structural analysis results on composite thin-walled beams.

4.2 Examples using data-driven shape functions for isotropic thin-walled beams

In order to verify that the proposed methodology can be applied to various types of cross-sections, the cross-sections in Fig. 4.1, including an open or a closed section, with or without symmetry axes are considered (units in Fig. 4.1 are defined as mm). Figures 4.2-4.5 show the sectional shape functions determined through the principal component analysis procedure. The figures correspond to an isotropic thin-walled beam problem (shape functions corresponding to composites can be found in Chapter 4.3). Shape functions of the isotropic thin-walled beam were confirmed first to verify the validity of the proposed approach. A degree of freedom $\xi_i(z)$ varying as a function of the axial coordinate z corresponds to each of the shape functions. The CSD data needed for the principal component analysis was obtained from ABAQUS [75] four-node element analysis results. All thin-walled beams considered are assumed to have a thickness of 2.5 mm (t) and a length of 0.6 m (L). For the ABAQUS analysis, they were meshed with an element size of around 2.5 mm. Considering beams made of steel, $E= 200$ GPa, $\nu= 0.3$, and $\rho= 7800$ kg/m³ were used. The first six sectional shape functions shown in Figs. 4.2-4.5 correspond to ξ_1 to ξ_6 representing three rigid-body motions of a section (U_x , U_y , U_z) and three rigid-body rotations (θ_x , θ_y , θ_z). The sectional shape functions associated with the additional degrees of freedom (ξ_7 - ξ_{24}) are those extracted as the principal cross-sectional deformation from the principal component analysis.

When we identify sectional shape functions in Fig. 4.2 referring to the previous higher-order beam theory [34, 39] for an isotropic thin-walled box beam, ξ_7 and ξ_9 represent the torsional distortion and warping and ξ_{10}, ξ_{15} and ξ_{16} represent the sectional shape functions induced by Poison's effect.

To check the validity of the sectional shape functions from the principal component analysis, we considered 1.2 m-long thin-walled beams of the cross-sections shown in Fig. 4.1 and performed static, vibration, and buckling analyses under various conditions. We initially checked the solution accuracy of the one-dimensional higher-order beam analysis using the data-driven shape functions by comparing the present results against the ABAQUS shell finite element analysis results. Examples 1 and 2 in Chapter 4.2.1 investigate how the static, vibration, and buckling analysis results of the thin-walled beams consisting of beam cross-sections in Fig. 4.1 vary as the number of degrees of freedom increases. We will show that the present data-driven-based beam analysis yields result nearly identical to those by the shell analysis as long as a reasonable number of degrees of freedom is used.

Hence, we investigate the numerical aspects of the present data-driven approach in Chapter 4.2.2. For generality, we use a thin-walled beam having a general section, as shown in Fig. 4.1 (d), as a test beam. In particular, we examine the effects of certain data-related controlling parameters on the obtained results. Specifically, we compare the static responses of the beam analyzed by a higher-order beam model

using different data-driven shape function sets. The following controlling parameters are used for each example.

- Example 3: Length of the base model and number of the sampled cross-sections to generate CSD data
- Example 4: Mesh resolution of the base shell model
- Example 5: Type of applied load used to collect the sectional deformations

For all numerical studies, 80 Hermite one-dimensional beam elements were used along the axial direction. For the shell reference model, a fine mesh approximately 2.5 mm in size was used to obtain converging results. In the case of the cantilevered general section beam 0.6 m in length which is used to generate the CSD data, we will have $N = N_d \times N_l (N_l = 3m + 6)$ CSD data. For all problems in the examples without additional specific information, a fine mesh gives $m = 110$ corresponding to the number of shell nodes on the cross-section of Fig. 4.1 (d) and N_d corresponding to the number of mesh along the axial axis. With the axial mesh size of 2.5 mm, the maximum value of N_d is 240 if data at every section is used. If undersampled, N_d can be smaller than 240.

4.2.1 Verification of static, vibration and buckling analysis

Example 1

In this example, static problems of a cantilevered beam under two loading

conditions are considered. *Loading condition 1* refers to shear line force of 1N applied to the edge connecting $*_c$ to $*_d$ in the Y -direction at the free end of the cantilevered beam of the general section shown in Fig. 4.1 (d). For *Loading condition 2*, we consider normal line force of 1N applied to the edge connecting $*_h$ to $*_a$ in the Y -direction at the free end of the same beam considered in *Loading condition 1*. Figures 4.6 (a) and (b) plot the three-dimensional displacement along the axial axis at point $*_a$ of the wall center when the beam is subjected to *Loading condition 1* and *Loading condition 2*, respectively. The static analysis results show that the data-driven higher-order beam model can predict the deformations sufficiently close to those calculated by the shell analysis. It can be seen that displacement components by the data-driven approach are in good agreement with those by the shell analysis if more than 18 degrees of freedom are used. Clearly, the use of more degrees of freedom improves the accuracy of the solution, implying that the sectional shape functions are consistently extracted by the data-driven analysis. Static analysis results for the beam cross-sections in Figs. 4.1 (a-c) are presented in Figs. 4.9-4.11.

Example 2

This example aims to check if the sectional shape functions derived by the static data-driven approach are effective for vibration and buckling analyses. For the vibration analyses, free-free and clamped-clamped thin-walled beams having the general cross-section shown in Fig. 4.1 (d) were considered. The results for the

vibration analysis are given in Tables 4.1 and 4.2 (Eigenfrequencies) and Figs. 4.7 (a) and (b) (Eigenmodes). In Tables 4.1 and 4.2, the eigenfrequencies by the present data-driven approach are denoted by 12, 18 and 24 degrees of freedom, which indicate the total number of the sectional shape functions included in the analysis. Clearly, the use of more degrees of freedom improves the accuracy of the solution, providing evidence of the consistency of the proposed method. When 24 degrees of freedom are used, the mean error over the lowest five eigenfrequencies is 0.88% with a maximum error of 1.57%. Figure 4.7 shows that the eigenmodes by the proposed data-driven approach are nearly identical to those by the shell analysis.

Table 4.3 and Fig. 4.8 present the results of a buckling analysis of a cantilevered beam with the cross-section shown in Fig. 4.1 (d). The critical load (P_{cr}) is predicted while applying a compressive unit load at the end of the beam with a rigid cross-sectional deformation boundary condition. The beam length is varied from 0.3 m to 1.2 m. Figure 4.8 showing the buckling mode shapes shows that the eigenmodes are correctly predicted for all beams of different lengths. The eigenmodes by the proposed approach in the figure were taken for the case of 24 degrees of freedom. In particular, local deformations appearing in the shortest beam are accurately predicted by the data-driven approach. Table 4.3 lists the critical loads predicted by the proposed data-driven approach and the shell analyses. Clearly, the prediction accuracy of the proposed method increases as the number of degrees of freedom increases. The data in Table 4.3 shows that the average error is

approximately 1.14% with the maximum error of less than 3% when 24 degrees of freedom are used.

Through this example, it is found that the use of the sectional shape functions derived from the static data-driven analysis are equally valid for other types of analyses, vibration and buckling analyses, supporting the effectiveness and validity of the present analysis. Besides, it is also found that the derived shape functions can be universally applied for analyses of beams with different lengths and boundary conditions. The results of vibration and buckling analyses of beams having other cross-sections shown in Figs. 4.1 (a-c) are also presented in Fig. 4.9-11. They support the findings from the analysis using the cross-section in Fig. 4.1 (d).

Generally, it is argued that additional cross-sectional deformations are required in the higher-order beam analysis process if the complexity of the beam-section increases. We confirmed that this tendency is revealed through the methodology proposed in this study. In the process of principal component analysis, the eigenvalues of the covariance matrix are obtained. For the eigenvector corresponding to a large eigenvalue, this study defined the core cross-sectional deformation as a priority. In Figure 4.12, the eigenvalue proportion and the remain proportion corresponding to each component value were confirmed for each cross-section in Fig. 4.1. When the k -th eigenvalue is defined as λ_k , eigenvalue

proportion is $\lambda_k / \sum_{j=1}^{3m} \lambda_j$ and remain proportion is $\sum_{j=k+1}^{3m} \lambda_j / \sum_{j=1}^{3m} \lambda_j$.

The trend of the graph shows that eigenvalue proportion and remain proportion decrease in the order of Lipped channel beam, Box beam, Double cell beam, and General section beam more quickly. In general, it is discussed that the open section beam (Fig. 4.1 (b)) has less influence on the cross-sectional deformation than the closed section beam (Fig. 4.1 (a, d)) [11]. Also, it is known that more complex cross-sectional deformations occur in the cross-section with multiple cells (Fig. 4.1 (c)) and asymmetric cross-section (Fig. 4.1 (d)) than in the rectangular cross-section [35, 37]. When we consider the results of Fig. 4.12, we can confirm that the results of the proposed methodology show the results as discussed in the previous studies.

Because the cross-sectional deformation that occurs on the beam section depends on the loading conditions of the static analysis or vibration and buckling analysis conditions, it is difficult to compare the analytical accuracy of thin-walled beams quantitatively with a single parameter. So, a qualitative comparison is made from the overall static, vibration, and compressive buckling analysis results in Example 1 and Example 2. When the same number of principal components are considered, it can be seen that the analytical results converge early to the shell analysis results in the order of cross-sections with small remain proportion values. Nevertheless, as

discussed in Example 1 and Example 2, the overall error is not significant when using 18 degrees of freedom regardless of the section complexity, and the results almost same to the shell analysis can be obtained when using 24 degrees of freedom.

4.2.2 Examples dealing with the validation of the data-driven approach

Example 3

To generate the CSD data for the data-driven shape functions, the length of a base beam model for a shell analysis was chosen to be approximately five times the section height. If cross-sectional deformation at every mesh along the Z -axis discretized by shell elements is used, the amount of CSD data will depend on the beam length assuming that the axial discretization level is identical. To examine the effect of the data size of the principal component analysis on the accuracy of the solution, we can vary the beam length. For this analysis, the same beam considered in Example 1 in Chapter 4.2.1 is used here. As an error measure of the solution accuracy, we will consider the mean compliance (equal to two times the stored strain energy). Figure 4.13 shows the compliance errors for varying values of N_d for two loading conditions. The compliance by the data-driven beam analysis is compared against that by the shell analysis. In the case of Fig. 4.13 (a), we vary the

length (L) of the cantilevered base beam model analyzed by the shell elements while sampling all CSD data at every section. Therefore, the longer the beam is, the larger the size of the data becomes. For instance, N becomes 336×180 and 336×240 for beams of $L = 0.45$ m and $L = 0.6$ m, respectively. An examination of Fig. 4.13 (a) shows that the use of larger N_d values (i.e., longer beams) results in a smaller compliance error although the accuracy improvement is marginal if $L \geq 0.6$ m. The beam length of $L = 0.6$ m, which is used throughout our analyses, is approximately five times the beam height. When fewer degrees of freedom are used, this tendency becomes more apparent.

Fig. 4.13 (b) also shows the effects of N_d on the solution accuracy, but the beam length is fixed at $L = 0.6$ m while CSD data is downsampled among the total 336×240 samples. The results of this analysis are shown when the shape function set is defined using an equidistant length longer than the mesh size along the beam axis to secure the base data. For instance, only one third of all samples are taken if $N_d = 80$. If $N_d = 1$ (yielding $N = 336$), each of the cross-sectional deformation only at the loaded end of the beam are used for the principal component analysis. If only a fraction of available data is used, the solution accuracy can deteriorate considerably. This tendency is more apparent with a relatively small number of degrees of freedom.

Example 4

With this example, we aim to investigate the effects of the base shell mesh resolution on the solution accuracy of the data-driven beam analysis. As before, we consider a cantilevered beam having the cross-section in Fig. 4.1 (d) under *Loading condition 1*. For this study, three shell meshes are considered:

- *Mesh F*: fine mesh size of about 2.5 mm (used for all analyses in previous examples). Each cross-section is discretized by 110 nodes
- *Mesh M*: medium mesh size of about 4 mm. Each cross-section is discretized by 68 nodes
- *Mesh C*: coarse mesh size of about 11.5 mm. Each cross-section is discretized by 24 nodes

The data-driven beam analyses are carried out using the cross-sectional deformations with different shell meshes. The displacement error along the contour of the beam cross-section at the loaded end of the beam is defined as

$$\sqrt{u_n^2 + u_s^2 + u_z^2} / \sqrt{u_n^2 + u_s^2 + u_z^2} \Big|_{ref} \quad (ref: \text{shell model } Mesh F \text{ results}).$$

The numerical results are presented in Fig. 4.14. The horizontal axis represents the arc-length s along the contour of the general section beam, where the locations of the corner nodes in Fig. 4.1 (d) are marked by the symbols $*_a$, $*_b$, etc. Because the shell results with *Mesh M* and *Mesh C* still yield small errors in the displacement prediction, the data-driven beam analyses with *Mesh M* and *Mesh C* also yield errors comparable to those by the data-driven beam analysis with *Mesh F*. All data-

driven higher-order beam models in Fig. 4.14 were tested with 18 degrees of freedom. This suggests that as long as converged shell results are used and a sufficient amount of CSD data is used, the data-driven beam result yields sufficiently accurate results only with marginal errors.

Example 5

During the determination of $\bar{\bar{\mathbf{U}}}$ in Eq. (3.23), we considered CSD data generated by general beam force loading (*Data set B*) and by shell nodal force loading (*Data set S*). Here, we will justify considering these two sets simultaneously during the determination of $\bar{\bar{\mathbf{U}}}$ instead of using *Data set B* or *Data set S* alone. *Data set B* has $6 \times N_d$ of CSD information while *Data set S* has $3m \times N_d$ of CSD information. To assess the accuracy of the solution depending on the choice of data set, we consider the same cantilevered beam in Example 1 in Chapter 4.2.1 under the following loading conditions:

- *Loading condition 3*: compressive force of 1 N applied to the mass center of the end of the beam with a rigid cross-sectional deformation boundary condition
- *Loading condition 4*: vertical force of 1N applied to $*_a$ in the *X*-direction at the end of the beam with a free cross-sectional deformation boundary condition

We vary the number of degrees of freedom and plot the errors in the mean

compliances of the beams in Fig. 4.15 (a) for *Loading condition 3* and in Fig. 4.15 (b) for *Loading condition 4*. The errors are calculated against the mean compliance calculated by the shell analysis. In this study, we aim to obtain a set of shape functions that can cover the overall behavior of a thin-walled beam. In fact, the required shape functions depend on the handling load. For example, it can be predicted that *Data set B* can provide better analysis results when subjected to the general beam force, while *Data set S* can predict better results when subjected to the shell nodal force.

The results in Figs. 4.15 (a) and (b) show that as long as the number of degrees of freedom is sufficiently large (i.e., more than 18 degrees of freedom), the errors in the compliance calculations are insignificant regardless of the selected data set. They also show that the use of *Data set B* appears to yield the best convergence. However, Fig. 4.15 (c) suggests that if *Data set B* is used alone, the detailed deformation is incorrectly estimated, while the simultaneous use of *Data sets B* and *Data sets S* yields the most accurate results. Fig. 4.15 (c) showed the deformation configuration at the end of the thin-walled beam under *Loading condition 4* using 24 degrees of freedom. This study justifies the simultaneous use of *Data set B* and *Data set S* in the data-driven approach for the analysis of thin-walled beams. With the proposed method considering both data sets, we were able to identify the relative degrees of freedom quickly, with better results to deal with the overall beam responses.

4.3 Examples using data-driven shape functions for composite thin-walled beams

In order to verify that the proposed methodology can be applied to general composite thin-walled beams including various types of cross-sections, the cross-sections in Figs. 4.1 (a, b, d) are considered (units in Fig. 4.1 are defined as mm). Figures 4.16-4.18 show the sectional shape functions determined through the principal component analysis procedure. The figures correspond to a composite thin-walled beam problem. Shape functions of the composite thin-walled beam were confirmed first to verify the validity of the proposed approach. As in Chapter 4.2, the CSD data needed for the principal component analysis was obtained from ABAQUS [75] four-node element analysis results. All thin-walled beams considered are assumed to have a thickness of 2 mm (t) and a length of 0.6 m (L). For the ABAQUS analysis, they were meshed with an element size of around 2.5 mm. Considering beams made of general carbon fiber reinforced plastic, the material properties for the analysis of the beam are as follows: $E_L = 141.96$ GPa, $E_T = 9.79$ GPa, $G_{LT} = 6$ GPa, $\nu_{LT} = 0.42$, and $\rho = 1445$ kg/m³. We considered five beams having a single ply at $[-45^\circ]$, $[-22.5^\circ]$, $[0^\circ]$, $[22.5^\circ]$ and $[45^\circ]$. The first six sectional shape functions shown in Figs. 4.16-4.18 correspond to ξ_1 to ξ_6 representing three rigid-body motions of a section (U_x , U_y , U_z) and three rigid-body rotations (θ_x , θ_y , θ_z). The sectional shape functions associated with the additional degrees of freedom (ξ_7 - ξ_{30}) are those extracted as the principal cross-sectional

deformation from the principal component analysis. When we compare sectional shape functions in Figs. 4.16-4.18 referring to the sectional shape functions in Chapter 4.2 for isotropic thin-walled beams, they look quite similar, but the order changes and it differs in detail. Part of this effect is covered in the examples.

To check the validity of the sectional shape functions from the principal component analysis, we considered 1.2 m-long thin-walled beams of the cross-sections shown in Figs. 4.1 (a, b, d) and performed static, vibration, and buckling analyses under various conditions. We initially checked the solution accuracy of the one-dimensional higher-order beam analysis using the data-driven shape functions by comparing the present results against the ABAQUS shell finite element analysis results. Examples 1 and 2 in Chapter 4.3.1 investigate how the static, vibration, and buckling analysis results of the composite thin-walled beams vary as the number of degrees of freedom increases. In Example 3, the numerical results based on our theory for composite thin-walled box beams are checked with different ply angles and stacking sequences. We will show that the present data-driven-based beam analysis yields result nearly identical to those by the shell analysis as long as a reasonable number of degrees of freedom is used.

Hereafter, we investigate the data-related aspects of the present data-driven approach in Chapter 4.3.2. We use a thin-walled beam having a box section, as shown in Fig. 4.1 (a), as a test beam. In particular, we examine the effects of

certain data-related controlling parameters on the obtained results. Specifically, we compare the static responses of the beam analyzed by a higher-order beam model using different data-driven shape function sets. The following controlling parameters are used for each example.

- Example 4: The number of reference shell models which are consist of different ply orientations required for obtaining shape functions for a general composite thin-walled beam
- Example 5: Comparing proposed shape functions with shape functions from specific thin-walled beam models

As like in Chapter 4.2, 80 Hermite one-dimensional beam elements were used along the axial direction for all numerical studies. For the shell reference model, a fine mesh approximately 2.5 mm in size was used to obtain converging results. In the case of the cantilevered general section beam 0.6 m in length which is used to generate the CSD data, we will have $N= 5 \times N_d \times N_l (N_l = 3m+6)$ CSD data. For all problems in the examples, a fine mesh gives $m=144$ corresponding to the number of shell nodes on the cross-section of Fig. 4.1 (a) and N_d corresponding to 240, the number of mesh along the axial axis.

4.3.1 Verification of static, vibration and buckling results

Example 1

In this example, static problems of a cantilevered beam under three loading conditions are considered. The beam has two plies with the same thickness of 1 mm and is stacked at $[15^\circ/30^\circ]$. *Loading condition 1* refers to shear line force of 1N applied to the edge connecting $*_c$ to $*_d$ in the Y -direction at the free end of the cantilevered beam of the box section shown in Fig. 4.1 (a). For *Loading condition 2*, we consider normal line force of 1N applied to the edge connecting $*_c$ to $*_d$ in the X -direction at the free end of the same beam considered in *Loading condition 1*. *Loading condition 3* refers to normal line force of 1 N/m applied at point (45, 120) of the wall center in the negative Y -direction along 0.6 m to 0.9 m of the clamped-clamped box beam. Figures 4.19 (a), (b) and (c) plot the three-dimensional displacement along the axial axis at point (45, 120) of the wall center when the beam is subjected to *Loading condition 1*, *Loading condition 2* and *Loading condition 3*, respectively. The static analysis results show that the data-driven higher-order beam model can predict the deformations sufficiently close to those calculated by the shell analysis. It can be seen that displacement components by the data-driven approach are in good agreement with those by the shell analysis if more than 30 degrees of freedom are used. Clearly, the use of more degrees of freedom improves the accuracy of the solution, implying that the sectional shape functions are consistently extracted by the data-driven analysis. Static analysis results for the beam cross-sections in Figs. 4.1 (b) and (d) are presented in Figs. 4.22-4.23.

Example 2

This example aims to check if the sectional shape functions derived by the static data-driven approach are effective for vibration and buckling analyses. For the vibration analyses, free-free and clamped-clamped thin-walled beams having the box cross-section shown in Fig. 4.1 (a) were considered. The results for the vibration analysis are given in Tables 4.4 and 4.5 (Eigenfrequencies) and Figs. 4.20 (a) and (b) (Eigenmodes). In Tables 4.4 and 4.5, the eigenfrequencies by the present data-driven approach are denoted by 15, 30, 45 and 60 degrees of freedom, which indicate the total number of the sectional shape functions included in the analysis. Clearly, the use of more degrees of freedom improves the accuracy of the solution, providing evidence of the consistency of the proposed method. When 60 degrees of freedom are used, the mean error over the lowest four eigenfrequencies is 0.72% with a maximum error of 1.21%. Figure 4.20 shows that the eigenmodes by the proposed data-driven approach are nearly identical to those by the shell analysis.

Table 4.6 and Fig. 4.21 present the results of a buckling analysis of a cantilevered beam with the cross-section shown in Fig. 4.1 (a). The critical load (P_{cr}) is predicted while applying a distributed compressive unit load at the free end of the beam. The beam length is varied from 0.6 m to 2.4 m. Figure 4.21 showing the buckling mode shapes shows that the eigenmodes are correctly predicted for all beams of different lengths. The eigenmodes by the proposed approach in the figure

were taken for the case of 60 degrees of freedom. In particular, local deformations appearing in the shortest beam are accurately predicted by the data-driven approach. Table 4.6 lists the critical loads predicted by the proposed data-driven approach and the shell analyses. Clearly, the prediction accuracy of the proposed method increases as the number of degrees of freedom increases. The data in Table 4.6 shows that the average error is approximately 0.67% with the maximum error of less than 1% when 60 degrees of freedom are used.

Through this example, it is found that the use of the sectional shape functions derived from the static data-driven analysis are equally valid for other types of analyses, vibration and buckling analyses, supporting the effectiveness and validity of the present analysis. Besides, it is also found that the derived shape functions can be universally applied for analyses of beams with different lengths and boundary conditions. The results of vibration and buckling analyses of beams having other cross-sections shown in Figs. 4.1 (b) and (d) are also presented in Figs. 4.22-23. They support the findings from the analysis using the cross-section in Fig. 4.1 (a).

Example 3

This example checks whether the proposed method is valid if the ply is laid out at an arbitrary angle or in various stacking sequences. The other geometric and material properties, boundary conditions are the same as in Example 1, except the

stacking sequences in this example. First, we tested static problems of composite thin-walled beams having a single ply of 2 mm thickness, where the ply angle varies from 0° - 90° . The beam rotation angle is predicted while applying a torsional load (1 Nm) or a bending moment (1 Nm) at the end of the beam with a rigid cross-sectional deformation boundary condition. Figure 4.24 shows how the torsional rotation angle (for the torsional load case) and the bending rotational angle (for the bending moment case) vary as the ply angle varies from 0° - 90° . The numerical results obtained by the present theory using 45 degrees of freedom are found to be in good agreement with the results of the shell analysis over a wide range of ply angles. It suggests that the proposed beam theory is capable of predicting the structural behavior of composite thin-walled beam, which is consist of an arbitrarily angled ply, accurately.

Then, we consider a static analysis of composite thin-walled beams having two plies of 1 mm thickness, stacked at $[0^\circ/90^\circ]$, $[15^\circ/-15^\circ]$ and $[-10^\circ/50^\circ]$. Figures 4.25 (a) and (b) plot the three-dimensional displacement along the axial axis at point (45, 120) of the wall center when the beam is subjected to *Loading condition 1* and *Loading condition 2*, respectively. 45 degrees of freedom were used for static analysis. The static analysis results show that the data-driven higher-order beam model can predict the deformations sufficiently close to those calculated by the shell analysis generally, regardless of the stacking sequences.

4.3.2 Examples dealing with special issues in a composite thin-walled beam under the data-driven approach

Example 4

In this example, we deal with the number of required reference shell models consist of different ply angles to obtain qualified shape functions of composite thin-walled beams. As addressed in Chapter 3.2.2, we suggest that more than five thin-walled beam models having different single ply angle should be considered to obtain shape functions which can recover the behavior of composite thin-walled beams laminated with plies consist of arbitrary angles. We check the validation of the assumption by comparing static analysis results of a composite thin-walled beam. The data-driven beam analyses are carried out using the shape functions with different data sets. As before, we consider a cantilevered beam having the cross-section in Fig. 4.1 (a) under *Loading condition 1* and *Loading condition 2*. The geometric and material properties, boundary conditions are the same as in Example 1 in Chapter 4.3. For this study, four shape function sets are considered:

- *Data set A1*: shape functions are obtained by an anisotropic material thin-walled beam consist of a single ply. Ply angle is $[0^\circ]$
- *Data set A3*: shape functions are obtained by three anisotropic material thin-walled beam consist of a single ply. Ply angles are $[-45^\circ]$, $[0^\circ]$ and $[45^\circ]$

- *Data set A5*: shape functions are obtained by five anisotropic material thin-walled beam consist of a single ply. Ply angles are $[-45^\circ]$, $[-22.5^\circ]$, $[0^\circ]$, $[22.5^\circ]$ and $[45^\circ]$. The shape functions obtained here are the proposed shape functions and are used in other composite thin-walled beam examples
- *Data set A7*: shape functions are obtained by seven anisotropic material thin-walled beam consist of a single ply. Ply angles are $[-45^\circ]$, $[-30^\circ]$, $[-15^\circ]$, $[0^\circ]$, $[15^\circ]$, $[30^\circ]$ and $[45^\circ]$. The shape functions obtained here are used for checking the convergence of the configures of the shape functions

As an error measure of the solution accuracy, we will consider the mean compliance (equal to two times the stored strain energy). We vary the number of degrees of freedom and plot the errors in the mean compliances of the beams in Fig. 4.26 (a) for *Loading condition 1* and in Fig. 4.26 (b) for *Loading condition 2*. The errors are calculated against the mean compliance calculated by the shell analysis. In this study, we aim to obtain a set of shape functions that can cover the behavior of general composite thin-walled beams. It is expected that using many composite thin-walled beam models can give better shape functions set. However, we aim to check whether the marginal model number required is five as suggested.

The results in Figs. 4.26 (a) and (b) show that the errors in the compliance

calculations decrease regardless of the selected data set when using more degrees of freedom. However, both of the figures suggest that if *Data set A1* or *Data set A3* is used, the meaningful error remains, while the use of *Data set A5* and *Data set A7* yield the most accurate results at almost the same level as suggested in Chapter 3.2.2.

Figure 4.27 shows the comparison between shape functions obtained from different data set using the modal assurance criterion (MAC) [76]. The MAC number is defined as a scalar representing the degree of consistency between two different modal vectors. MAC was formerly used for model-to-test comparisons and model updating. However, it can be successfully applied for comparing shape functions from different data sets. The MAC takes on values from zero (representing no consistent correspondence) to one (representing a consistent correspondence), and it is defined as follows

$$MAC_{ij} = \frac{\left| \{^1\mathbf{P}_{\tilde{\xi}_i}\}^T \{^2\mathbf{P}_{\tilde{\xi}_j}\} \right|^2}{\{^1\mathbf{P}_{\tilde{\xi}_i}\}^T \{^1\mathbf{P}_{\tilde{\xi}_i}\} \{^2\mathbf{P}_{\tilde{\xi}_j}\}^T \{^2\mathbf{P}_{\tilde{\xi}_j}\}} \quad (4.1)$$

where $^1\mathbf{P}_{\tilde{\xi}_i}$ is the i -th principal component of *Data set 1* and $^2\mathbf{P}_{\tilde{\xi}_j}$ is the j -th principal component of *Data set 2*. Concerning principal components obtained by using *Data set A7*, we compared principal components obtained from *Data set A1*, *Data set A3*, *Data set A5* in Figs. 4.27 (a), (b) and (c), respectively. When we consider Figs. 4.27 (a) and (b), principal cross-sectional deformations are similar

order under 20 degrees of freedom. However, the order of principal components is quite different after then. Also, considering Fig. 4.26, although the MAC values are close to one, they give different shape functions in detail.

On the other hand, in the case of using *Data set A5* in Fig. 4.27 (c), it can be confirmed that the shape functions are predicted in almost the same order. Taking into account that use of *Data set A5* yields accurate results at the same level with *Data set A7*, the results verify the suggestion to use five thin-walled beam models for obtaining the shape functions of general composite thin-walled beams.

Example 5

In this example, we discuss the difference between shape functions required for general composites (corresponding to Chapter 3.2.2) and shape functions required for isotropic materials or a specific composite (corresponding to Chapter 3.2.1). We discuss two issues in this example. The first issue is the difference between the shape functions required for composite thin-walled beam and isotropic thin-walled beam, which was mentioned in the previous work [43]. Then, validating the use of shape functions for a specific composite, which was discussed in Chapter 3.2.1, is the second issue. The verifications of these problems are discussed by comparing static analysis results from data-driven beam models using different shape functions and checking the MAC value between them. For this study, two additional shape function sets are considered:

- *Data set Iso*: shape functions are obtained by an isotropic material thin-walled beam. Considering beams made of steel, $E= 200$ GPa and $\nu= 0.3$ were used
- *Data set [30°]*: shape functions are obtained by an anisotropic material thin-walled beam consist of a single ply. Ply angle is [30°], and other material properties are the same in Chapter 4.3

We compare static analysis results of a composite thin-walled beam, which are carried out using the shape functions with different reference data. As before, we consider a cantilevered beam having the cross-section in Fig. 4.1 (a) under *Loading condition 1* and *Loading condition 2*. All conditions except beam thickness and ply orientation are shown in Example 4 in Chapter 4.3. The ply is a single ply with a thickness of 2 mm and the rotation angle θ is 30°. Figures 4.28 (a) and (b) plot the errors in the mean compliances of the beams for *Loading condition 1* and *Loading condition 2*, respectively. The errors are calculated against the mean compliance calculated by the shell analysis. The results in Fig. 4.28 show that the errors decrease regardless of the selected data set when using more degrees of freedom as like the previous examples. However, the figure shows that if *Data set Iso* is used, the meaningful error remains, while the use of *Data set [30°]* yields the most accurate results at almost the same level with the proposed shape functions when using more than about 30 degrees of freedom.

Figures 4.29 (a) and (b) shows the MAC value between the principal component obtained by *Proposed (Data set A5)* with those by *Data set Iso* and *Data set [30°]*, respectively. When we consider Fig. 4.29 (a), we can see that the order of the principal cross-sectional deformations for the isotropic thin-walled beam are quite different compared to the proposed principal cross-sectional deformations. Figure 4.28 shows that even if the MAC values are close to 1, shape functions are provided differently in detail, which means that the structural analysis error becomes meaningful. This shows the necessity of using shape functions required for composite materials.

Figure 4.29 (b) also seems like the order of the principal cross-sectional deformations are different, and even the deformation patterns are coupled to each other. However, considering Fig. 4.28 together, it shows that whether the principal cross-sectional deformations are different, it can give qualified analysis results. By this, we can show that the shape functions can be obtained even with limited data when the composite thin-walled beam of a specific condition should be considered.

Table 4.1 Eigenfrequencies obtained by the data-driven approach with different numbers of sectional shape functions (12, 18, and 24 DOFs) for a free-free isotropic beam having the cross-section shown in Fig. 4.1 (d) (unit: Hz)

Method	1st	2nd	3rd	4th	5th
Shell	229.19	415.88	546.56	707.42	764.64
12 DOFs	241.01	435.34	590.11	726.09	847.01
18 DOFs	229.84	418.02	550.46	719.59	773.49
24 DOFs	229.63	416.40	549.27	716.17	771.84

Table 4.2 Eigenfrequencies obtained by the data-driven approach with different numbers of sectional shape functions (12, 18, and 24 DOFs) for a clamped-clamped isotropic beam having the cross-section shown in Fig. 4.1 (d) (unit: Hz)

Method	1st	2nd	3rd	4th	5th
Shell	219.19	399.12	517.04	724.78	737.57
12 DOFs	232.92	418.67	558.98	747.35	820.67
18 DOFs	221.95	404.87	524.97	739.43	748.56
24 DOFs	221.40	402.48	523.03	736.19	746.41

Table 4.3 The critical load (P_{cr}) calculated by the data-driven approach using different numbers of sectional shape functions (12, 18, and 24 DOFs) for a isotropic cantilever beam under a compressive load having the cross-section shown in Fig. 4.1 (d) with different beam lengths (L) (unit: N)

Method	$L= 300\text{mm}$	$L= 600\text{mm}$	$L= 900\text{mm}$	$L= 1200\text{mm}$
Shell	1088850	326850	147567	83406
12 DOFs	1282101	358807	162013	91611
18 DOFs	1126624	328627	148495	83972
24 DOFs	1121417	328235	148378	83916

Table 4.4 Eigenfrequencies obtained by the data-driven approach with different numbers of sectional shape functions (15, 30, 45, and 60 DOFs) for a free-free composite beam having the cross-section shown in Fig. 4.1 (a) (unit: Hz)

Method	1st	2nd	3rd	4th
Shell	185.58	220.37	262.03	281.19
15 DOFs	187.94	223.16	293.76	298.76
30 DOFs	185.04	219.96	263.90	279.66
45 DOFs	184.66	219.43	262.20	278.12
60 DOFs	184.39	219.10	260.09	277.83

Table 4.5 Eigenfrequencies obtained by the data-driven approach with different numbers of sectional shape functions (15, 30, 45, and 60 DOFs) for a clamped-clamped composite beam having the cross-section shown in Fig. 4.1 (a) (unit: Hz)

Method	1st	2nd	3rd	4th
Shell	255.58	291.73	305.82	327.77
15 DOFs	293.25	308.46	328.28	345.06
30 DOFs	259.00	289.63	305.37	331.91
45 DOFs	256.80	288.42	304.07	329.97
60 DOFs	254.81	288.20	303.72	329.14

Table 4.6 The critical load (P_{cr}) calculated by the data-driven approach using different numbers of sectional shape functions (15, 30, 45, and 60 DOFs) for a composite cantilever beam under a compressive load having the cross-section shown in Fig. 4.1 (a) with different beam lengths (L) (unit: N)

Method	$L= 600\text{mm}$	$L= 1200\text{mm}$	$L= 1800\text{mm}$	$L= 2400\text{mm}$
Shell	28151	27666	16940	9584
15 DOFs	40610	40135	20501	11622
30 DOFs	29125	28678	17191	9730
45 DOFs	28771	28346	17101	9681
60 DOFs	28310	27866	17053	9654

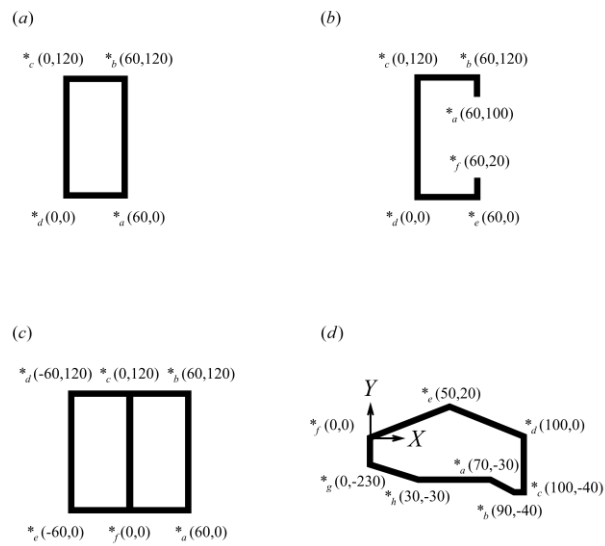


Fig. 4.1 Various beam cross-sections considered for analysis: (a) box beam, (b) lipped channel beam, (c) double-cell beam, and (d) general section beam

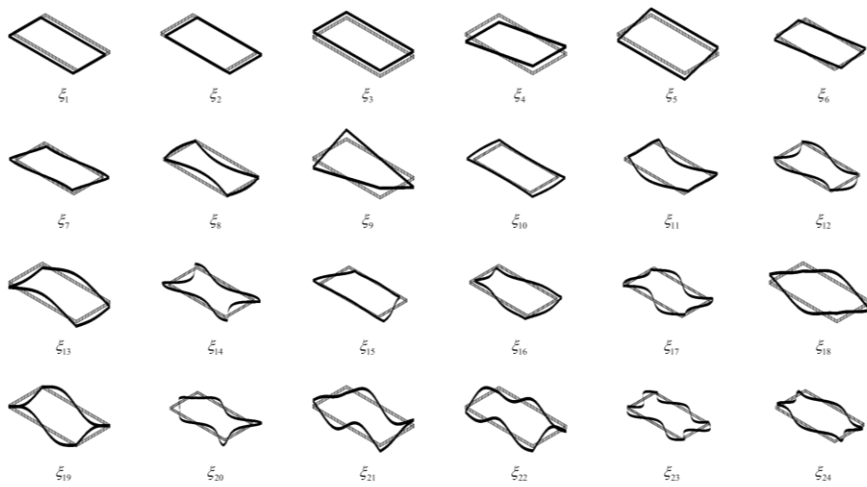


Fig. 4.2 Sectional shape functions of the isotropic thin-walled beam derived by the data-driven approach for the cross-section in Fig. 4.1 (a)

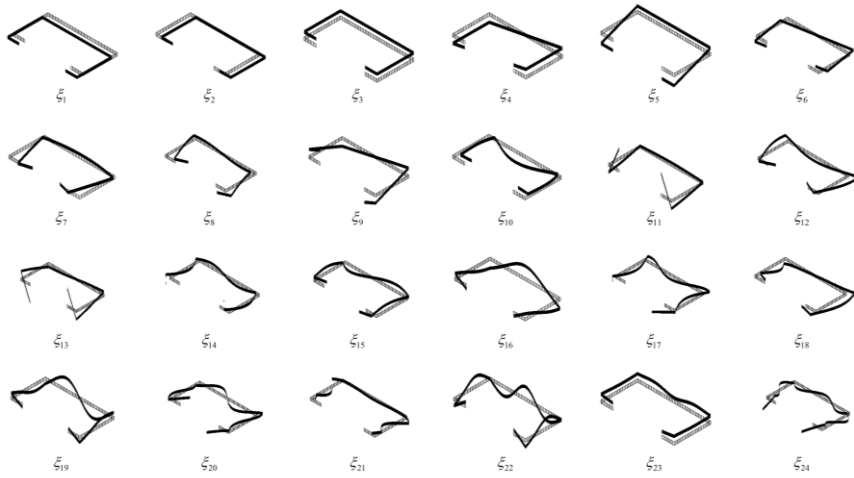


Fig. 4.3 Sectional shape functions of the isotropic thin-walled beam derived by the data-driven approach for the cross-section in Fig. 4.1 (b)

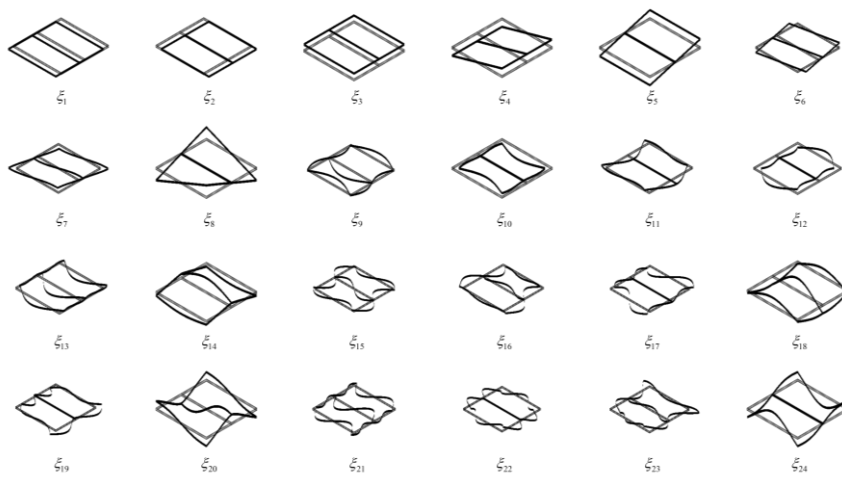


Fig. 4.4 Sectional shape functions of the isotropic thin-walled beam derived by the data-driven approach for the cross-section in Fig. 4.1 (c)

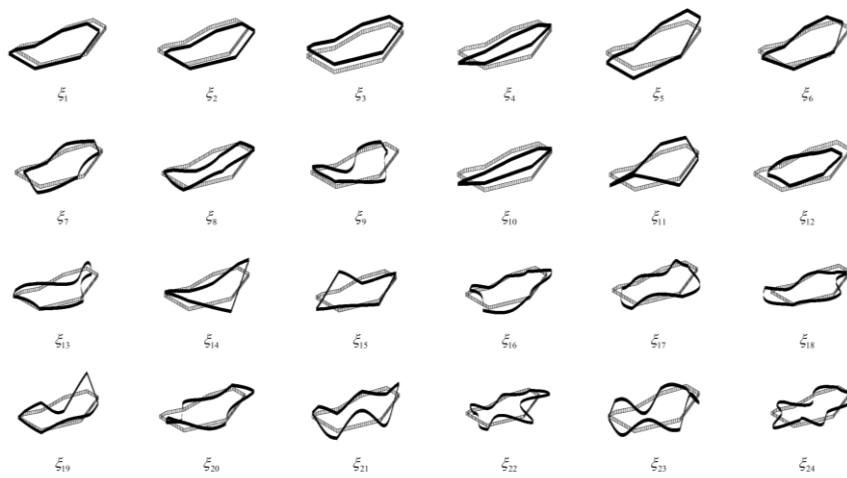


Fig. 4.5 Sectional shape functions of the isotropic thin-walled beam derived by the data-driven approach for the cross-section in Fig. 4.1 (d)

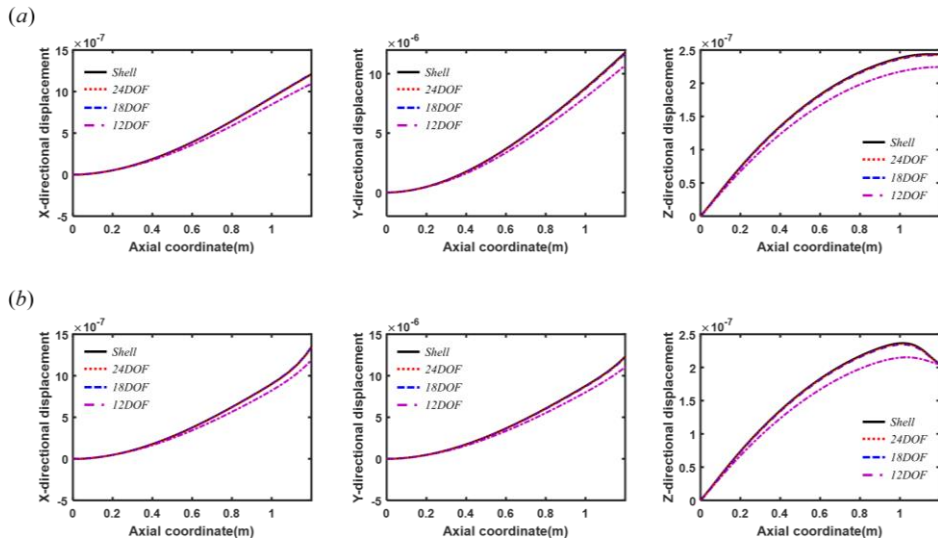


Fig. 4.6 Numerical results for Example 1 in Chapter 4.2 for (a) *Loading condition 1* and (b) *Loading condition 2*. The three-dimensional displacements in the X-, Y- and Z-directions are plotted by the present data-driven one-dimensional analysis using 12, 18 and 24 degrees of freedom and compared with the shell-based results. The measurements were taken at point $*_a$ (see Fig. 4.1 (d)) of the cross-section along the beam axial axis

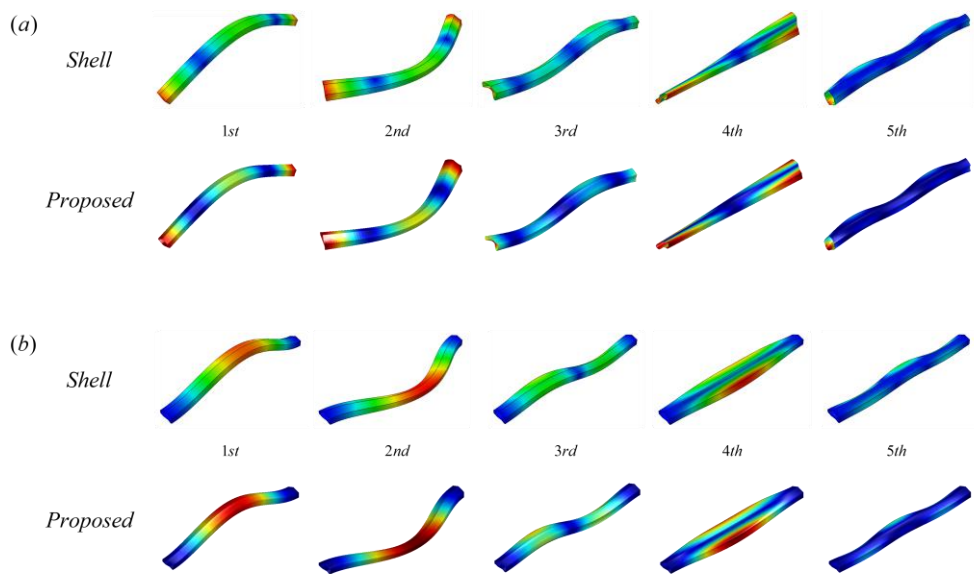


Fig. 4.7 Eigenmodes obtained for Example 2 in Chapter 4.2 (a) free-free beam and (b) clamped-clamped beam. *Shell*: the result by ABAQUS shell elements, *Proposed*: the result by the present data-driven beam elements

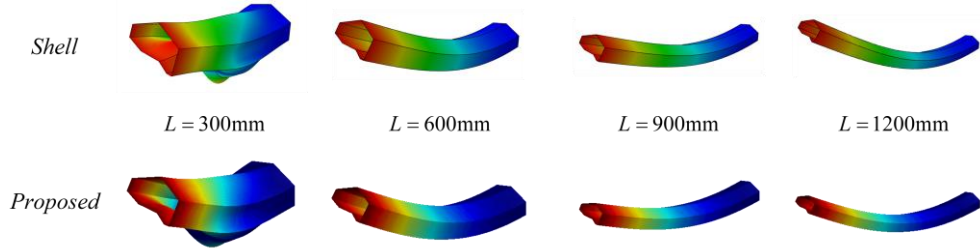


Fig. 4.8 Buckling mode shapes in beams under axial compression for Example 2 in Chapter 4.2. L : beam length, *Shell*: the result by ABAQUS shell elements, *Proposed*: the result by the present data-driven beam elements

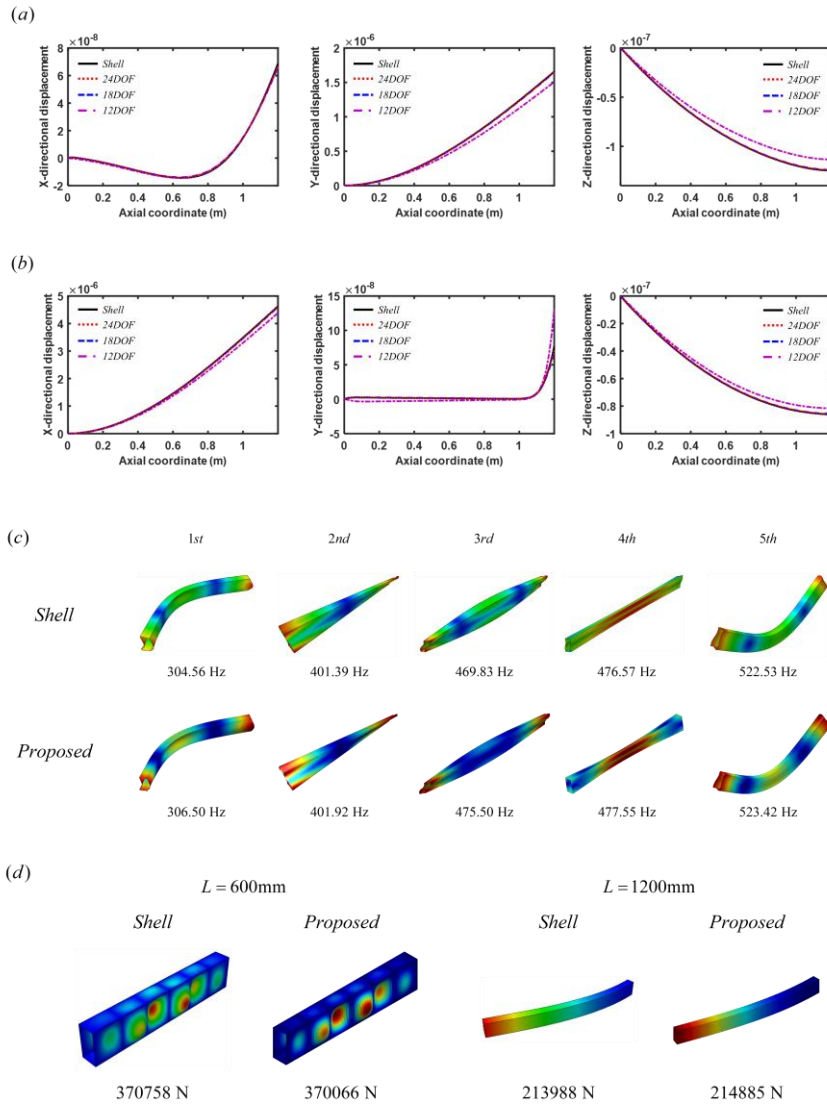


Fig. 4.9 Numerical results for a isotropic box beam. Three-dimensional displacement along the Z (axial) coordinate along (45, 120) (see Fig. 4.1 (a)) of the wall center subjected to (a) shear line force of 1N applied to the $*_a - *_b$ edge in the Y direction and (b) normal line force of 1N applied to the $*_c - *_d$ edge in the X direction. (c) Eigenmodes with eigenfrequencies in the free-free beam, and (d) buckling mode shapes with the critical load in the cantilevered beam under a compression load

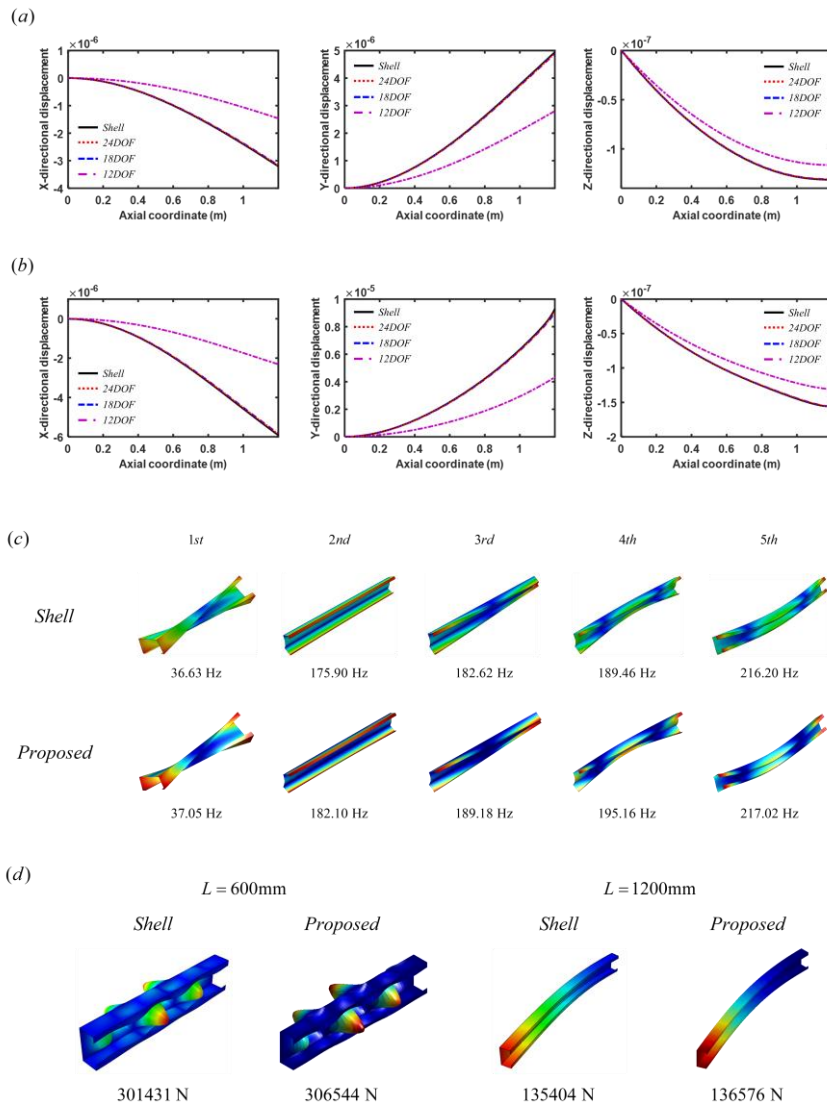


Fig. 4.10 Numerical results for an isotropic lipped channel beam. Three-dimensional displacement along the Z (axial) coordinate along (30, 120) (see Fig. 4.1 (b)) of the wall center subjected to (a) shear line force of 1N applied to the $*_c - *_d$ edge in the Y direction and (b) normal line force of 1N applied to the $*_b - *_c$ edge in the Y direction. (c) Eigenmodes with eigenfrequencies in the free-free beam, and (d) buckling mode shapes with the critical load in the cantilevered beam under a compression load

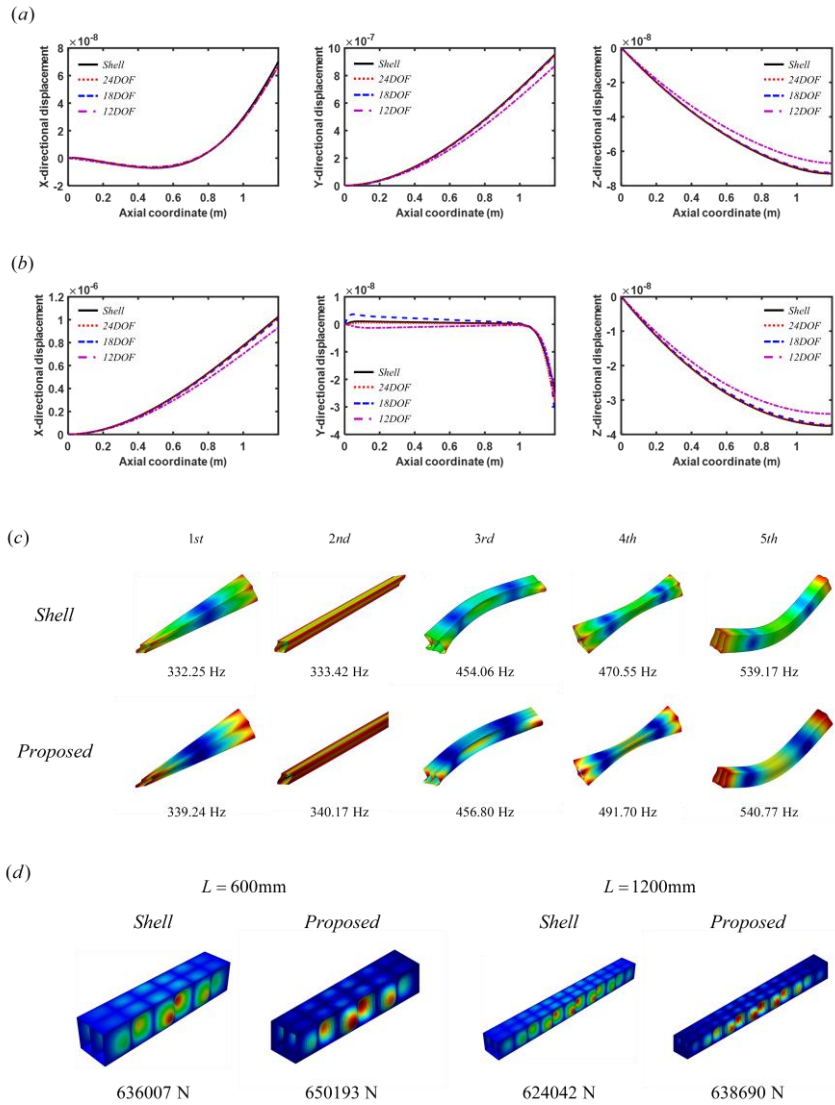


Fig. 4.11 Numerical results for an isotropic double-cell beam. Three-dimensional displacement along the Z (axial) coordinate along (30, 120) (see Fig. 4.1 (c)) of the wall center subjected to (a) a shear line force of 1N applied to the $*_a - *_b$ edge in the Y direction and (b) a normal line force of 1N applied to the $*_d - *_e$ edge in the X direction. (c) Eigenmodes with eigenfrequencies in the free-free beam, and (d) buckling mode shapes with the critical load in the cantilevered beam under a compression load

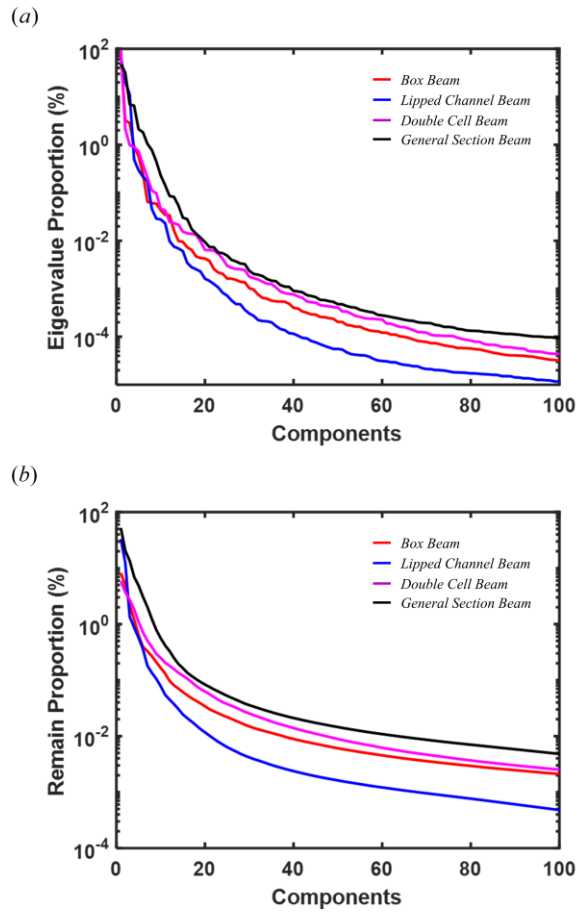


Fig. 4.12 The tendencies of the eigenvalue of the principal components corresponding to each beam sections in Fig. 4.1 for Chapter 4.2.1. (a) Eigenvalue proportion and (b) Remain proportion

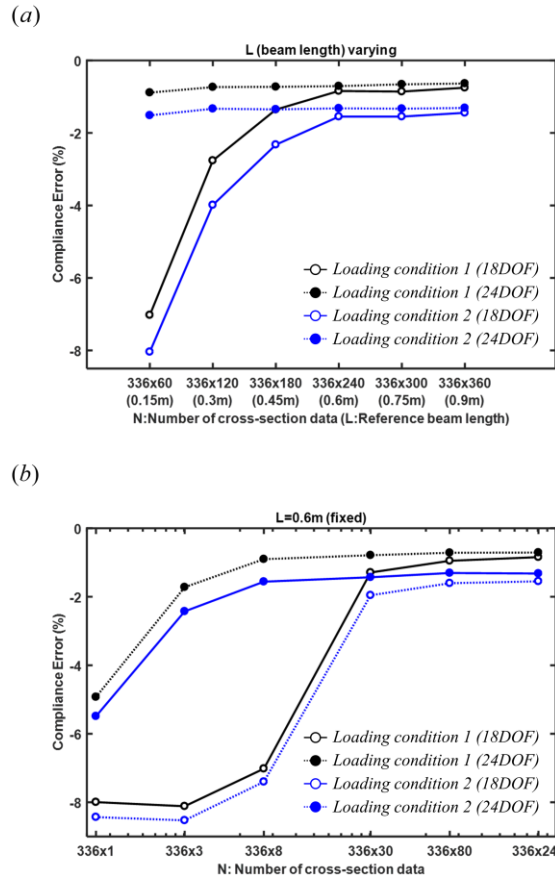


Fig. 4.13 The effects of the data size on the solution accuracy for Example 3 in Chapter 4.2. Errors in the mean compliance are plotted for (a) the proposed approach when the reference beam length varies from 0.15 m to 0.9 m and (b) the proposed approach when downsampling among the total amount of cross-sectional deformation data when the beam length is fixed at 0.6 m

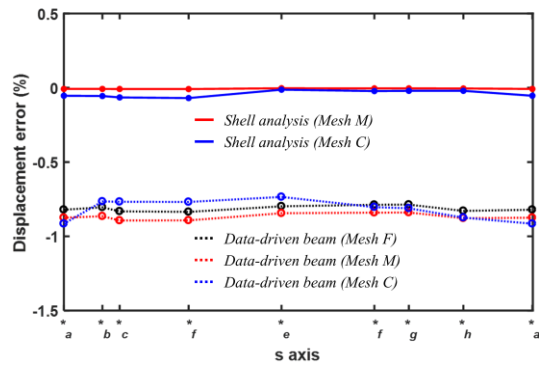


Fig. 4.14 The effects of the shell mesh resolution on the solution accuracy for Example 4 in Chapter 4.2. Errors by larger shell mesh analyses (*Mesh M*, *Mesh C*) and data-driven beam analysis corresponding to shape functions obtained when using different shell mesh sizes (*Mesh F*, *Mesh M*, *Mesh C*) are plotted

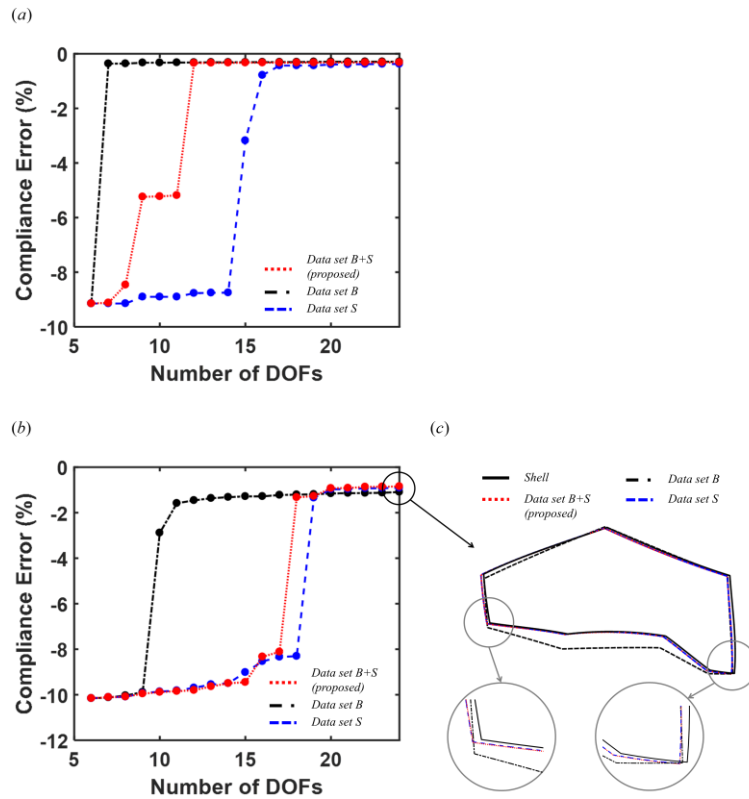


Fig. 4.15 The effects of the selected data sets on the solution accuracy for Example 5 in Chapter 4.2. Errors in the mean compliance for (a) *Loading condition 3* and (b) *Loading condition 4*, and (c) deformation configuration at the free end of the thin-walled beam model under *Loading condition 4* using 24 degrees of freedom

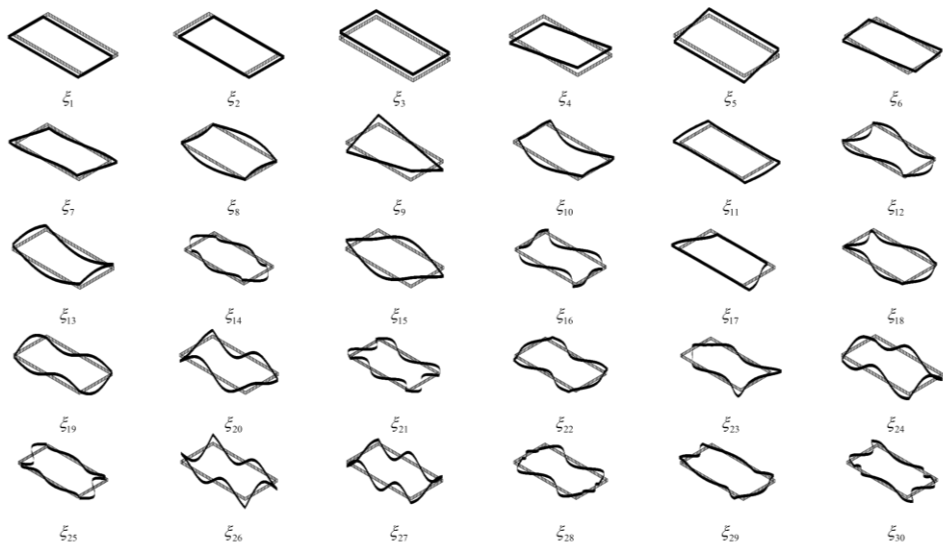


Fig. 4.16 Sectional shape functions of the composite thin-walled beam derived by the data-driven approach for the cross-section in Fig. 4.1 (a)

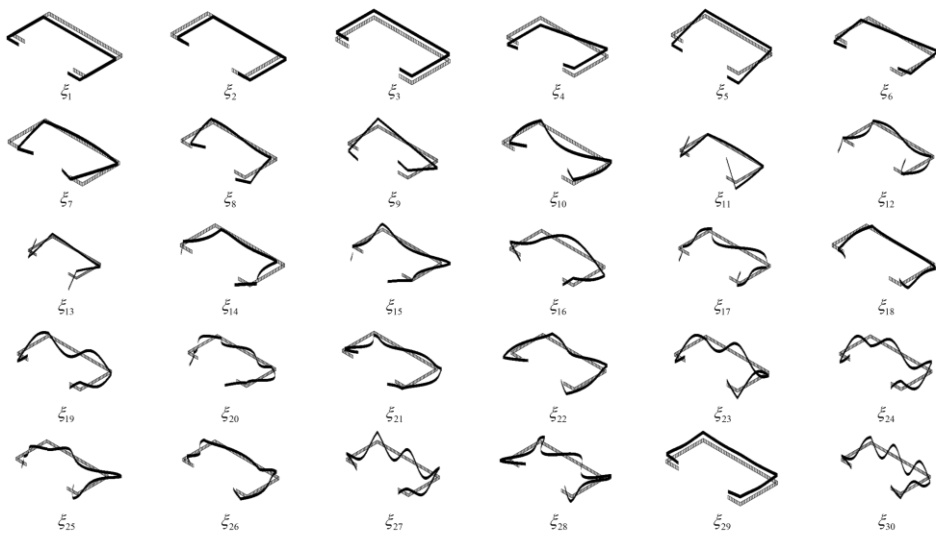


Fig. 4.17 Sectional shape functions of the composite thin-walled beam derived by the data-driven approach for the cross-section in Fig. 4.1 (b)

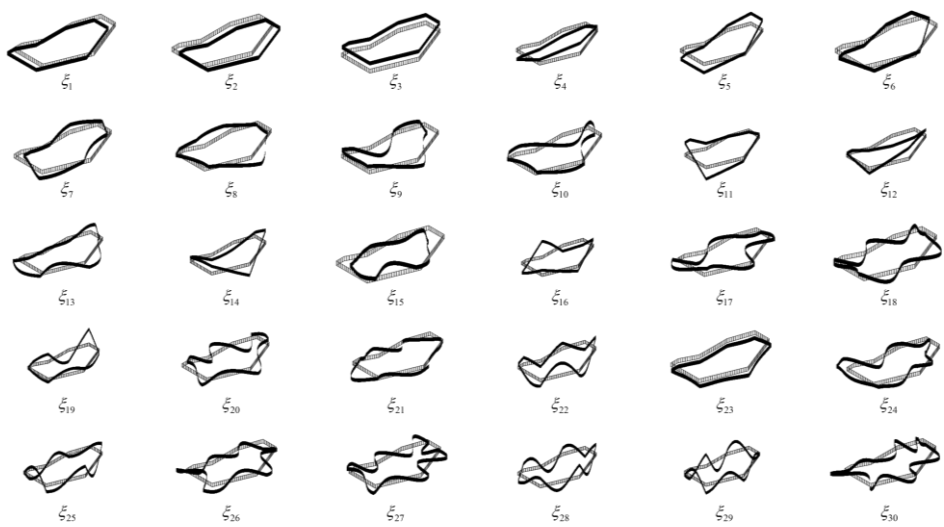


Fig. 4.18 Sectional shape functions of the composite thin-walled beam derived by the data-driven approach for the cross-section in Fig. 4.1 (d)

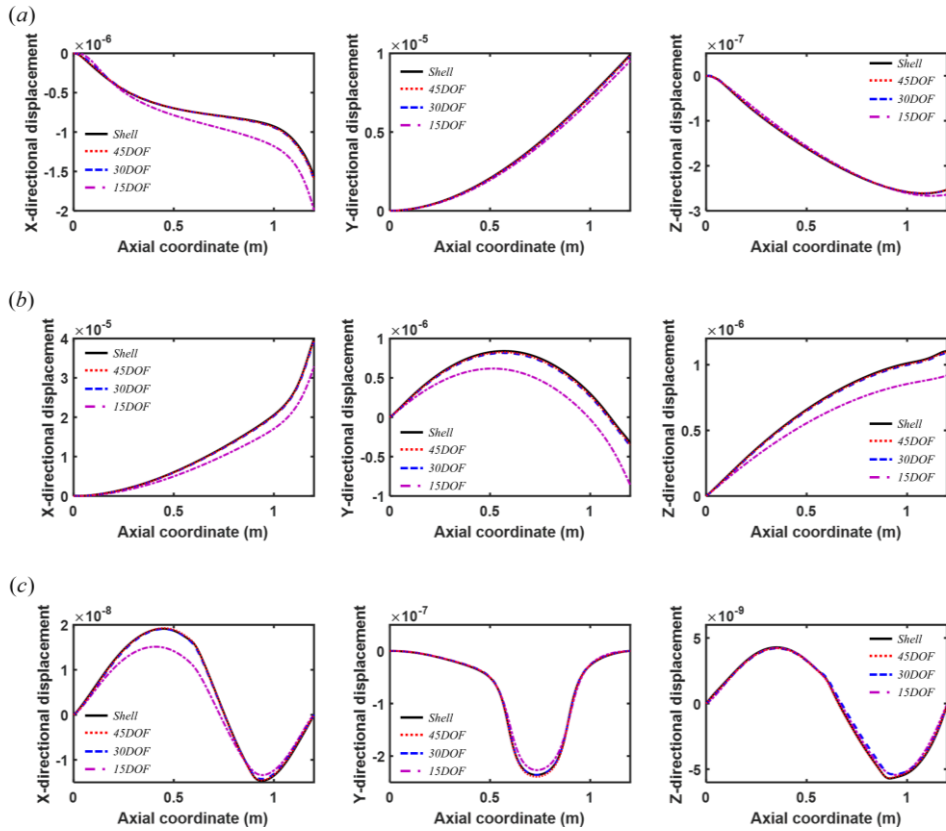


Fig. 4.19 Numerical results for Example 1 in Chapter 4.3 for (a) *Loading condition 1*, (b) *Loading condition 2* and (c) *Loading condition 3*. The three-dimensional displacements in the X-, Y- and Z-directions are plotted by the present data-driven one-dimensional analysis using 15, 30 and 45 degrees of freedom and compared with the shell-based results. The measurements were taken at point (45, 120) (see Fig. 4.1 (a)) of the cross-section along the beam axial axis

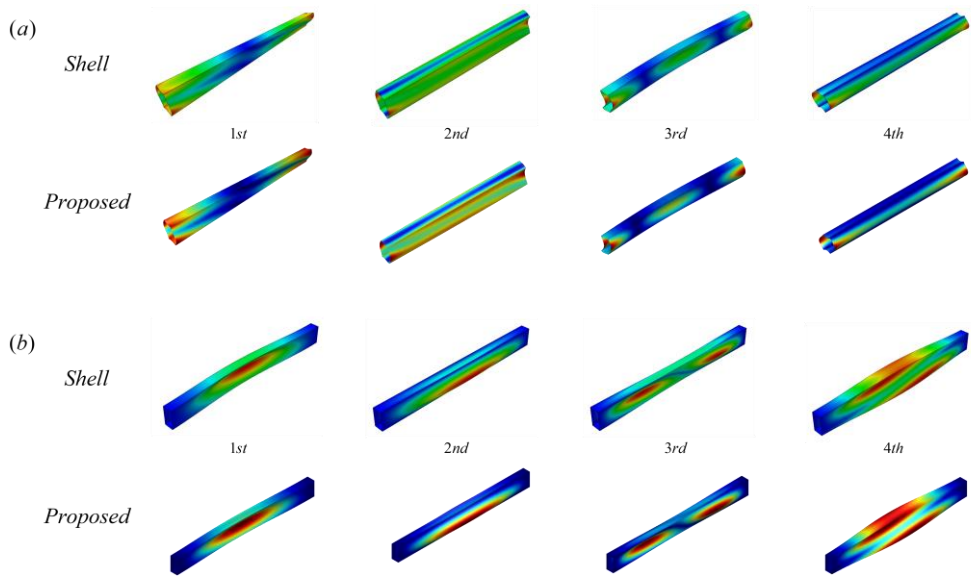


Fig. 4.20 Eigenmodes obtained for Example 2 in Chapter 4.3 (a) free-free beam and (b) clamped-clamped beam. *Shell*: the result by ABAQUS shell elements, *Proposed*: the result by the present data-driven beam elements

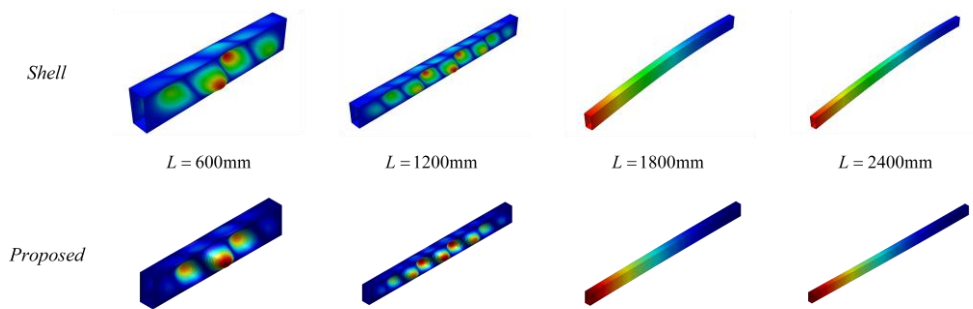


Fig. 4.21 Buckling mode shapes in beams under axial compression for Example 2 in Chapter 4.3. L : beam length, *Shell*: the result by ABAQUS shell elements, *Proposed*: the result by the present data-driven beam elements

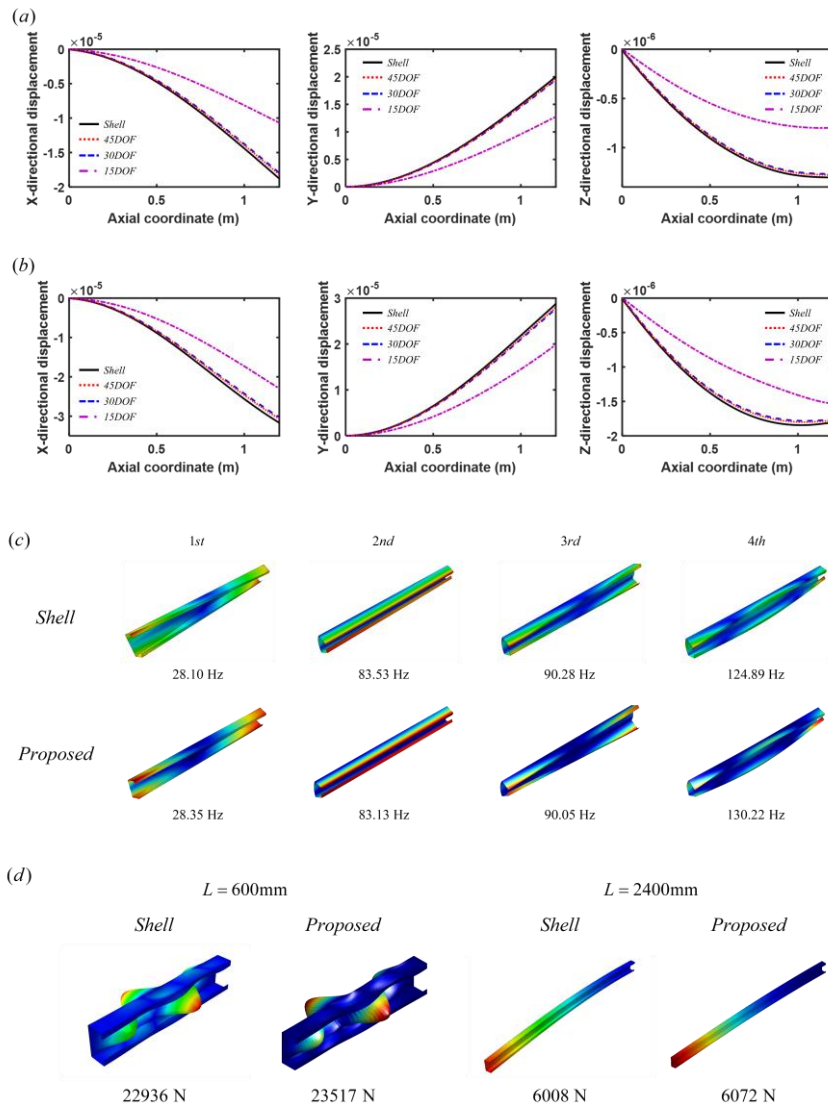


Fig. 4.22 Numerical results for a composite lipped channel beam. Three-dimensional displacement along the Z (axial) coordinate along (30, 120) (see Fig. 4.1 (b)) of the wall center subjected to (a) shear line force of 1N applied to the $*_c - *_d$ edge in the Y direction and (b) normal line force of 1N applied to the $*_b - *_c$ edge in the Y direction. (c) Eigenmodes with eigenfrequencies in the free-free beam, and (d) buckling mode shapes with the critical load in the cantilevered beam under a compression load

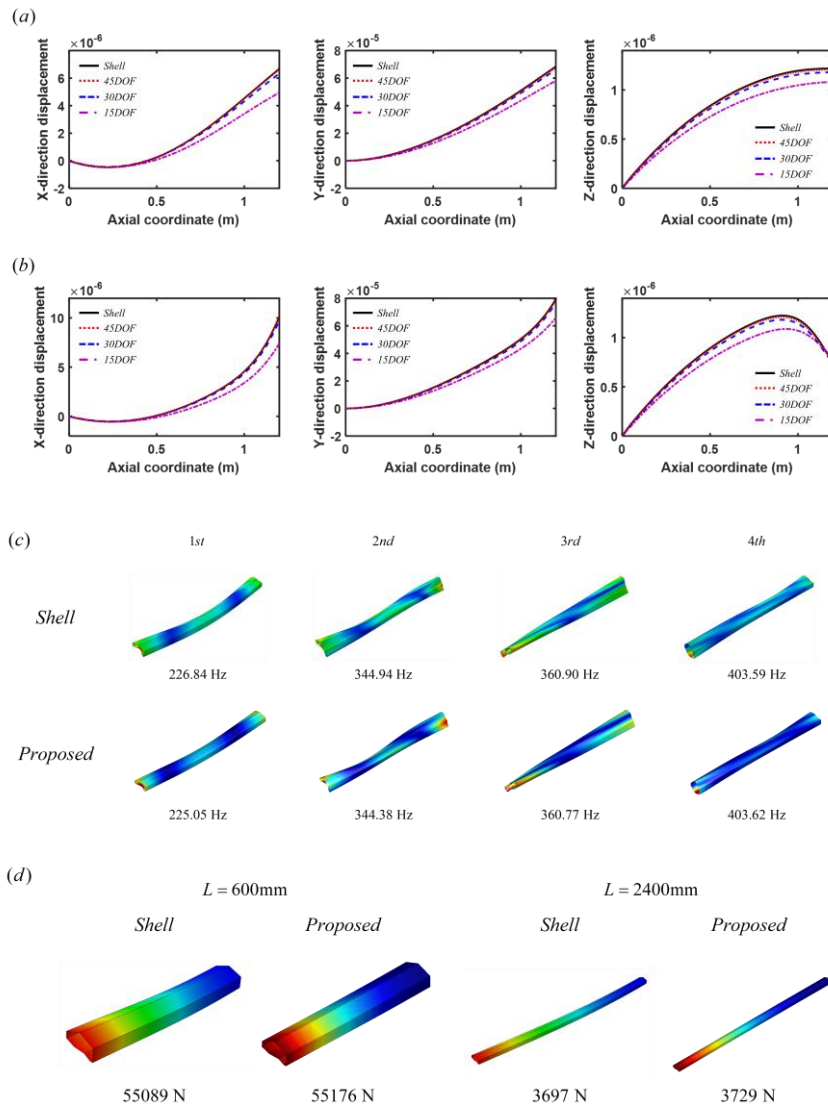


Fig. 4.23 Numerical results for a composite general section beam. Three-dimensional displacement along the Z (axial) coordinate along $*_a$ (see Fig. 4.1 (d)) of the wall center subjected to (a) shear line force of 1N applied to the $*_c - *_d$ edge in the Y direction and (b) normal line force of 1N applied to the $*_h - *_d$ edge in the Y direction. (c) Eigenmodes with eigenfrequencies in the free-free beam, and (d) buckling mode shapes with the critical load in the cantilevered beam under a compression load

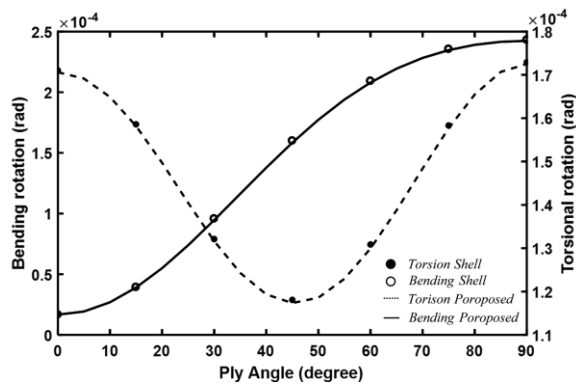


Fig. 4.24 Numerical results for Example 3 in Chapter 4.3 conducted with a single-layer composite thin-walled box beam under torsional moment and bending moment

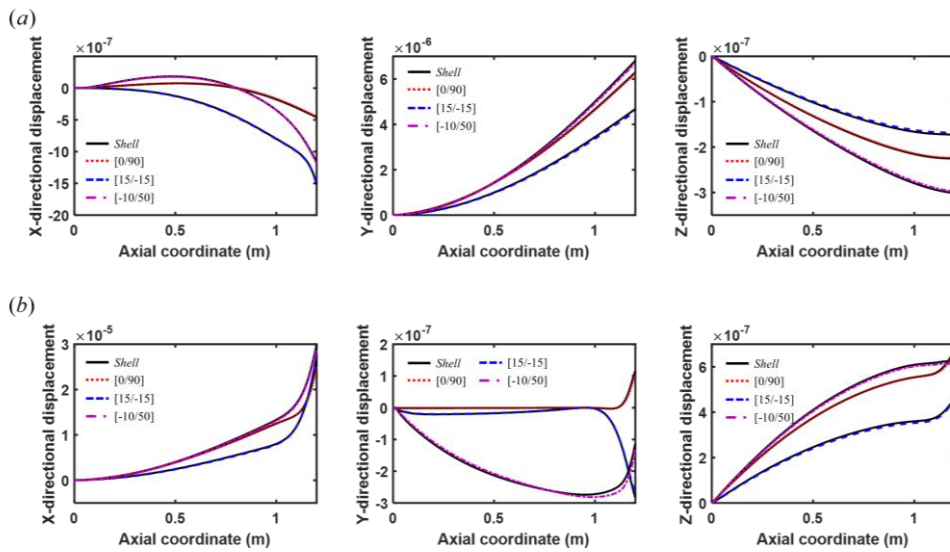


Fig. 4.25 Numerical results for Example 3 in Chapter 4.3 for (a) *Loading condition 1* and (b) *Loading condition 2*. The three-dimensional displacements in the X-, Y- and Z-directions are plotted by the present data-driven one-dimensional analysis using 45 degrees of freedom and compared with the shell-based results. The measurements were taken at point (45, 120) (see Fig. 4.1 (a)) of the cross-section along the beam axial axis

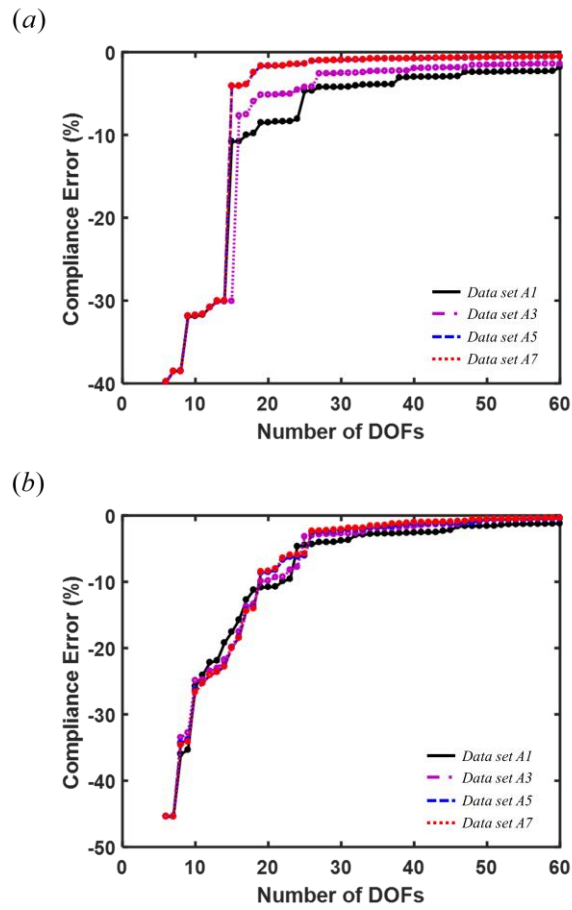


Fig. 4.26 The effects of the selected data sets on the solution accuracy for Example 4 in Chapter 4.3. Errors in the mean compliance for (a) *Loading condition 1* and (b) *Loading condition 2*

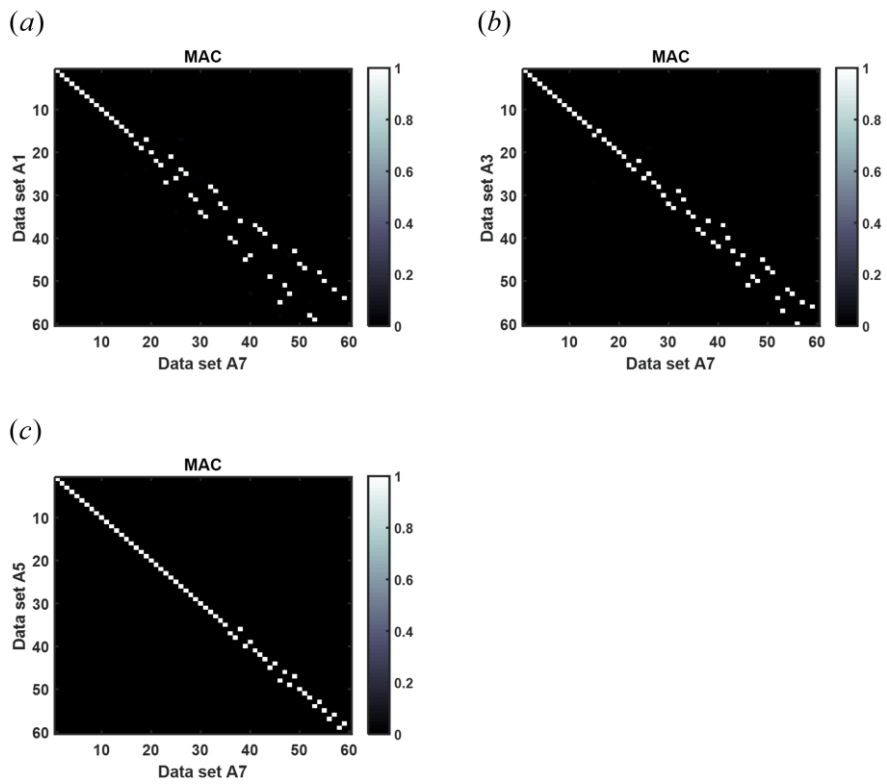


Fig. 4.27 MAC values between shape functions obtained by different data sets for Example 4 in Chapter 4.3. (a) *Data set A1* and *Data set A7*, (b) *Data set A3* and *Data set A7* and (c) *Data set A5* and *Data set A7*

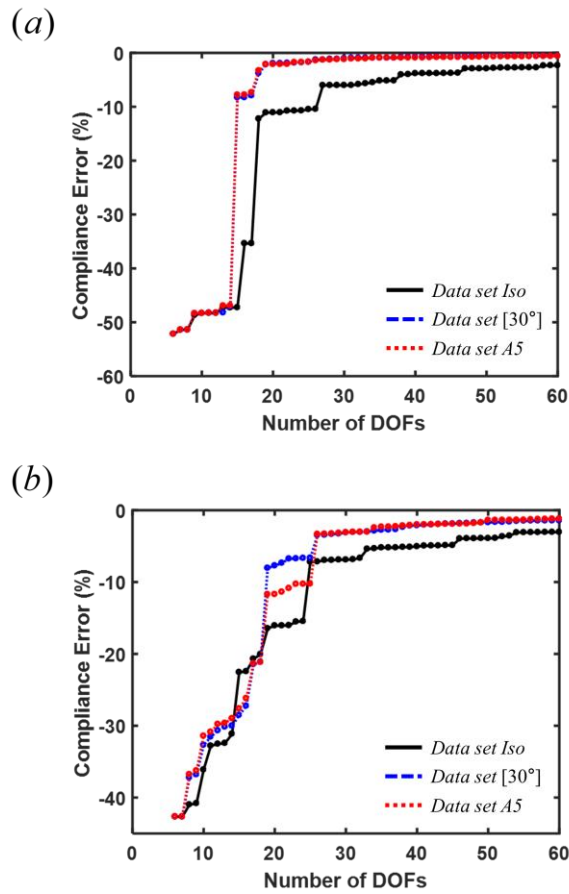
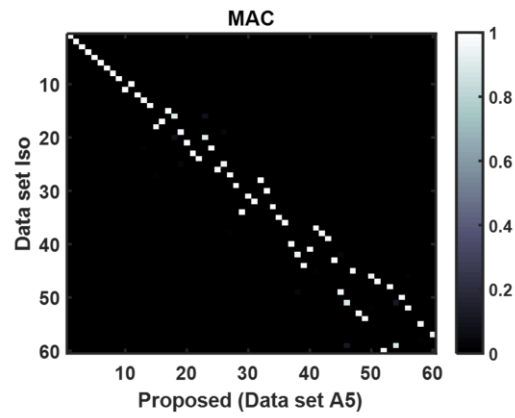


Fig. 4.28 The effects of the selected data sets on the solution accuracy for Example 5 in Chapter 4.3. Errors in the mean compliance for (a) *Loading condition 1* and (b) *Loading condition 2*

(a)



(b)

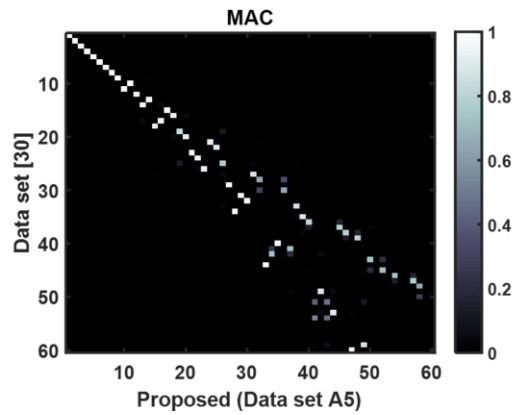


Fig. 4.29 MAC values between shape functions obtained by different data sets for Example 5 in Chapter 4.3. (a) *Data set Iso* and *Data set A5* and (b) *Data set [30°]* and *Data set A5*

CHAPTER 5.

Conclusions

In this thesis, we proposed a data-driven approach for a higher-order beam analysis of composite thin-walled beams in which the core cross-sectional shape functions corresponding to higher-order beam degrees of freedom are derived using a data-driven approach. Because the effects of anisotropic properties and lamination cannot be taken into account in the earlier higher-order beam theory, the beam formulation was updated so that it can represent these effects. After establishing the modified higher-order beam theory for composite thin-walled beam, a finite element formulation based on the developed higher-order beam theory was set up with explicitly expressed stiffness, mass, and geometric stiffness matrices.

In the process of deriving shape functions, the big data representing local deformations of all cross-sections of a composite thin-walled beam was obtained using the structural response of a statically loaded thin-walled cantilevered beam modeled by a detailed shell model. This big data was processed by a principal component analysis to extract the principal cross-sectional deformations used to

derive the sectional shape functions corresponding to important beam degrees of freedom. Compared to previous analytical or numerical models often requiring various kinematic assumptions, this approach requires no such assumptions. Moreover, the approach was shown to be valid for various types of cross-sections, making it possible to prioritize significant cross-sectional deformations.

The findings from our data-driven approach are summarized below.

- The use of two sets of loads, the global beam force and shell nodal force, applied at the cantilevered beam was found to be effective for generating reliable cross-sectional deformation data
- The generated data of the cross-sectional deformations must be properly pre-processed before the principal component analysis: the orthogonalization of the resulting deformations with respect to six rigid-body motions, separating the cross-sectional deformation data into two parts, the in-plane and out-of-plane deformations to be consistent with the higher-order beam theory, and adjusting the average of the entire cross-sectional deformation data matrix to zero
- The amount of cross-sectional deformation data critically affects the solution accuracy; accordingly, a sufficient amount of data should be used. A guideline was given
- The sectional shape functions derived by static analyses were found to be valid not only for static problems but also vibration and buckling problems

(within about 1% errors), justifying the validity of the proposed approach

- If the mesh resolution of the shell model for the thin-walled beam was sufficiently fine to yield converging results, the collected data of cross-sectional deformations was also found to be reliable
- Using more than five anisotropic thin-walled beam models enables obtaining shape functions for analyzing the behavior of general composite thin-walled beams
- Shape functions that can analyze isotropic thin-walled beams were not enough to analyze composite thin-walled beams. However, shape functions specialized for a certain composite thin-walled beam model can be defined with limited data

While the analysis here is limited to linear analysis as the first work on the subject, the proposed big-data approach is expected to be more effective when dealing with nonlinear thin-walled beam problems where the cross-sectional deformation of the beam has more influence. Also, this thesis has concentrated on the process of defining shape functions to a given specific section, but the extension of this work should be able to deal with a general approach to carried out shape functions generally without performing new analysis according to the cross-sectional shape. It is also expected to extend this research to the field of data-driven reduced finite element modeling, as the identification process for deformation modes can be applied to other dimensional models similarly.

APPENDIX A.

Physical approach for deriving shape functions of composite thin-walled box beams

A.1 Overview

In the Appendix, research [43] on composite thin-walled box beam that obtains shape functions by a physical approach is introduced. The developed higher-order beam theory here has formed the base of the research in this thesis. A systematic method to derive the sectional shape functions that are critical in developing the higher-order beam theory for composite box beams is proposed. Because the effects of anisotropic properties and lamination cannot be taken into account in the earlier higher-order beam theory [34-42], the developed theory must consider additional degrees of freedom related to sectional shape functions that can represent these effects. The sectional shape functions needed for composite thin-walled box beams are newly derived by considering the characteristics of the anisotropic materials. After establishing the higher-order beam theory for composite thin-walled box beam, a finite element formulation was considered by the procedure introduced in this dissertation. Various numerical studies, including a

case for arbitrary ply orientations, confirmed that our higher-order beam theory using 26 nodal degrees of freedom for each node yields results sufficiently comparable with the detailed shell results. Satisfactory results were obtained for both static and free-vibration problems.

Figure A.1 shows a thin-walled box beam with width b , height h , and wall thickness t . The cross section of the beam lies on the plane containing the global X and Y -axes, and the axial direction of the beam is defined as the Z -axis. The local coordinates, n_{ed} , s_{ed} , and z_{ed} ($ed=1, 2, 3, 4$), are introduced for each of the four walls forming the thin-walled box beam. The positive directions of these local coordinates are illustrated in Fig. A.1. In the Appendix, the sign ed will be omitted when the equations are regardless of the edge number.

A.2 Cross-sectional deformations derived by plane stress assumption

Referring to Fig. 2.1, ply indices are assigned from the inside to the outside of the beam cross section. It is assumed that the q -th ply of each wall has circumferentially uniform stiffness (CUS) with the same angle. The overall process is sketched in Fig. A.2 and a detailed account of it will be presented below.

To derive the sectional shape functions, the stress distribution on the cross section is considered first for an external force, moment, or bimoment (see the figures on the left of Figs. A.3-A.4 for example.) Then, we calculate the strain field arising from the stress. The next step is to identify the cross-sectional deformations needed to generate the strain field. The obtained deformations are used to define the sectional shape functions for the degrees of freedom used for composite thin-walled box beam analysis. Although the subsequent analysis is valid for a case involving multiple plies, we assume that the composite thin-walled box beam consists of a single anisotropic ply at an arbitrary angle to facilitate our explanations. A case involving multiple plies will be considered in the examples at the end of the Chapter A.4 by extending the proposed approach in the single ply case in a straightforward manner.

Because the state of stress in the s - z plane at the centerline of the composite thin-

walled box beam ($n=0$) shown in Fig. 1.2 can be assumed to be in a state of plane stress, the following stress-strain relation is employed [72]:

$$\begin{Bmatrix} \varepsilon_{ss} \\ \varepsilon_{zz} \\ 2\varepsilon_{sz} \end{Bmatrix} = \begin{bmatrix} \bar{S}_{11} & \bar{S}_{12} & \bar{S}_{16} \\ \bar{S}_{21} & \bar{S}_{22} & \bar{S}_{26} \\ \bar{S}_{61} & \bar{S}_{62} & \bar{S}_{66} \end{bmatrix} \begin{Bmatrix} \sigma_{ss} \\ \sigma_{zz} \\ \sigma_{sz} \end{Bmatrix} \quad (\text{A.1})$$

If the eight degrees of freedom Vlasov beam theory [11] is used, one can consider eight external loads denoted by a symbol ζ , which represents four out-of-plane loads (F_z, M_x, M_y, B_L) and four in-plane loads (F_x, F_y, M_z, B_T). Here, F and M denote the force and moment, respectively, B_L denotes the longitudinal bimoment that generates warping, and B_T represents the transverse bimoment that causes distortion [34]. The stress fields caused by out-of-plane loads with unit magnitude and in-plane loads with unit magnitude are denoted by σ_{zz}^{ζ} and σ_{sz}^{ζ} , respectively. The second columns in Figs. A.3-A.4 illustrate the distribution of σ_{zz}^{ζ} and σ_{sz}^{ζ} , whose explicit formula are given below. Because the main forms of the stress fields were derived in [11, 77], the detailed procedure used to derive them are not repeated here.

$$\sigma_{zz}^{F_z}(s_{ed}) = 1 \quad (\text{A.2})$$

$$\sigma_{zz}^{M_x}(s_1) = -\sigma_{zz}^{M_x}(s_3) = s, \quad \sigma_{zz}^{M_x}(s_2) = -\sigma_{zz}^{M_x}(s_4) = \frac{h}{2} \quad (\text{A.3})$$

$$\sigma_{zz}^{M_y}(s_1) = -\sigma_{zz}^{M_y}(s_3) = \frac{-b}{2}, \quad \sigma_{zz}^{M_y}(s_2) = -\sigma_{zz}^{M_y}(s_4) = s \quad (\text{A.4})$$

$$\sigma_{zz}^{B_L}(s_1) = \sigma_{zz}^{B_L}(s_3) = \frac{bs}{2}, \quad \sigma_{zz}^{B_L}(s_2) = \sigma_{zz}^{B_L}(s_4) = \frac{-hs}{2} \quad (\text{A.5})$$

$$\sigma_{sz}^{F_x}(s_1) = -\sigma_{sz}^{F_x}(s_3) = -2s, \quad \sigma_{sz}^{F_x}(s_2) = -\sigma_{sz}^{F_x}(s_4) = \frac{2s^2}{b} - \left(\frac{b}{2} + h\right) \quad (\text{A.6})$$

$$\sigma_{sz}^{F_y}(s_1) = -\sigma_{sz}^{F_y}(s_3) = \left(\frac{h}{2} + b\right) - \frac{2s^2}{h}, \quad \sigma_{sz}^{F_y}(s_2) = -\sigma_{sz}^{F_y}(s_4) = -2s \quad (\text{A.7})$$

$$\sigma_{sz}^{M_z}(s_{ed}) = 1 \quad (\text{A.8})$$

$$\sigma_{sz}^{B_T}(s_{ed}) = (-1)^{ed+1} \quad (\text{A.9})$$

Once σ_{zz}^{ζ} and σ_{sz}^{ζ} are determined, stresses $\sigma_{zz}(s, z)$ and $\sigma_{sz}(s, z)$ created by external loads along the centerline of the cross section ($n=0$) can be written as $\sigma_{zz} = \sigma_{zz}^{\zeta}(s)\zeta(z)$ ($\zeta = F_z, M_x, M_y,$ and B_L) and $\sigma_{sz} = \sigma_{sz}^{\zeta}(s)\zeta(z)$ ($\zeta = F_x, F_y, M_z,$ and B_T), respectively.

The next step is to derive the strain fields associated with stress fields $\sigma_{zz} = \sigma_{zz}^{\zeta}(s)\zeta(z)$ and $\sigma_{sz} = \sigma_{sz}^{\zeta}(s)\zeta(z)$. We begin with the case for out-of-plane loads. Using Eq. (A.1) and Eqs. (A.2–A.5), the strain components, ε_{ss}^{ζ} , ε_{zz}^{ζ} , and ε_{sz}^{ζ} ($\zeta \in \{F_z, M_x, M_y, B_L\}$) on the centerline ($n=0$) can be expressed as:

$$\varepsilon_{ss}^{\zeta}(s, z) = \bar{S}_{12} \sigma_{zz}^{\zeta}(s)\zeta(z) \quad (\text{A.10})$$

$$\varepsilon_{zz}^{\zeta}(s, z) = \bar{S}_{22} \sigma_{zz}^{\zeta}(s)\zeta(z) \quad (\text{A.11})$$

$$2\varepsilon_{sz}^\zeta(s, z) = \bar{S}_{62} \sigma_{zz}^\zeta(s) \zeta(z) \quad (\text{A.12})$$

Because the deformed pattern or shape of the beam section is independent of the z -axis, the strains in Eqs. (A.10-12) can be written by using the product of the functions $(\phi_s^\zeta(s))$ and $(\phi_z^\zeta(s))$ of s and the functions $(\delta^\zeta(z))$ of z as:

$$\varepsilon_{ss}^\zeta(s, z) = \frac{\partial u_s^{(\zeta,1)}}{\partial s} = \frac{\partial(\phi_s^{(\zeta,1)}(s)\delta^{(\zeta,1)}(z))}{\partial s} = \dot{\phi}_s^{(\zeta,1)}(s)\delta^{(\zeta,1)}(z) \quad (\text{A.13})$$

$$\varepsilon_{zz}^\zeta(s, z) = \frac{\partial u_z^{(\zeta,2)}}{\partial z} = \frac{\partial(\phi_z^{(\zeta,2)}(s)\delta^{(\zeta,2)}(z))}{\partial z} = \phi_z^{(\zeta,2)}(s)\delta'^{(\zeta,2)}(z) \quad (\text{A.14})$$

$$\begin{aligned} 2\varepsilon_{sz}^\zeta(s, z) &= \frac{\partial u_s^{(\zeta,3)}}{\partial z} + \frac{\partial u_z^{(\zeta,4)}}{\partial s} = \frac{\partial(\phi_s^{(\zeta,3)}(s)\delta^{(\zeta,3)}(z))}{\partial z} + \frac{\partial(\phi_z^{(\zeta,4)}(s)\delta^{(\zeta,4)}(z))}{\partial s} \\ &= \phi_s^{(\zeta,3)}(s)\delta'^{(\zeta,3)}(z) + \dot{\phi}_z^{(\zeta,4)}(s)\delta^{(\zeta,4)}(z) \end{aligned} \quad (\text{A.15})$$

In Eqs. (A.13-15), the displacement field, u_η^ζ , is defined as $u_\eta^\zeta(s, z) = \phi_\eta^\zeta(s)\delta^\zeta(z)$. Instead of using the expression in Eq. (2.1), we introduce new symbols, $\phi_\eta(s)$ and $\delta(z)$, to express u_η because $\phi_\eta(s)$ may not be the same as $\psi_\eta(s)$ unless $\phi_\eta(s)$'s are independent to each other. To distinguish $\phi_\eta(s)$ from $\psi_\eta(s)$, $\phi_\eta(s)$ will be called the cross-section deformation function in this chapter. The procedure used to obtain $\psi_\eta(s)$'s from $\phi_\eta(s)$'s is given in Chapter A.3. The symbols in u_η^ζ are redefined as $(\zeta, 1)$ and $(\zeta, 2)$ for those associated with the ε_{ss} and ε_{zz} terms to count the number of cross-section deformation modes to be considered. Likewise, symbols $(\zeta, 3)$ and $(\zeta, 4)$ are used to represent the cross-section deformation mode related to the shear strain. In the

subsequent discussion, m_n in (ζ, m_n) will be called the mode number.

If Eqs. (A.10) and (A.13) are compared, the following relations can be identified:

$$\phi_s^{(\zeta, 1)}(s) = \int \sigma_{zz}^\zeta(s) ds \quad (\text{A.16})$$

$$\bar{S}_{12}\zeta(z) = \delta^{(\zeta, 1)}(z) \quad (\text{A.17})$$

Eq. (A.16) suggests that mode 1 has non-zero s -directional displacement. Because mode 1 represents distortion in the plane of the cross section, the n -directional displacement is also induced. The n -directional displacement can be found by considering the continuities in displacement, angle, and moment at the corners of the cross section once the s -directional displacement is determined. Because the procedure used to find the n -directional displacement is the same as that used in existing higher-order beam theory research [34, 39], the detailed procedure will not be repeated here. For convenience, the integration constant appearing in Eq. (A.16) is chosen so that $\phi_s^{(\zeta, 1)}$ is orthogonal to the sectional shape functions associated with the four degrees of freedom $(U_x, U_y, \theta_z, \chi)$.

The comparison of Eqs. (A.11) and (A.14) yields the following relations for mode 2:

$$\phi_z^{(\zeta, 2)}(s) = \sigma_{zz}^\zeta(s) \quad (\text{A.18})$$

$$\bar{S}_{22}\zeta(z) = \delta^{(\zeta, 2)}(z) \quad (\text{A.19})$$

As Eq. (A.18) shows, mode 2 involves the cross-sectional deformations occurring

in the z -direction.

By using Eqs. (A.12) and (A.15), one can find the cross-section deformation functions for modes 3 and 4 as follows:

$$\phi_s^{(\zeta, 3)}(s) = \sigma_{zz}^\zeta(s) \quad (\text{A.20})$$

$$\phi_z^{(\zeta, 4)}(s) = \int \sigma_{zz}^\zeta(s) ds \quad (\text{A.21})$$

$$\bar{S}_{62}\zeta(z) = \delta^{(\zeta, 3)}(z) + \delta^{(\zeta, 4)}(z) \quad (\text{A.22})$$

Modes 3 and 4 involve in-plane and out-of-plane deformations, respectively. The n -directional deformation for mode 3 can be obtained by using the procedure described for mode 1. In the case of mode 4, Eq. (A.21) determines the cross-section deformation function with only the z component. The integration constant value can be decided by imposing the continuity of displacement at the cross-section corners in the same manner as in existing studies [34, 39], and by making $\phi_z^{(\zeta, 4)}$ orthogonal to the sectional shape function associated with the axial deformation degree of freedom (U_z) for convenience.

The cross-section deformation functions derived by the procedure described above are explicitly given below and are graphically illustrated in Fig. A.3.

$$\begin{aligned} \phi_s^{(F_z, 1)}(s_{ed}) &= s \\ \phi_n^{(F_z, 1)}(s_1) &= \phi_n^{(F_z, 1)}(s_3) = \frac{b}{2}, \quad \phi_n^{(F_z, 1)}(s_2) = \phi_n^{(F_z, 1)}(s_4) = \frac{h}{2} \end{aligned} \quad (\text{A.23})$$

$$\phi_z^{(F_z, 2)}(s_{ed}) = \sigma_{zz}^{F_z}(s_{ed}) \quad (\text{A.24})$$

$$\begin{aligned} \phi_s^{(F_z, 3)}(s_{ed}) &= \sigma_{zz}^{F_z}(s_{ed}) \\ \phi_n^{(F_z, 3)}(s_1) = \phi_n^{(F_z, 3)}(s_3) &= \frac{-s(2b^2h + 3bh^2 - 4bs^2 - h^3 + 4hs^2)}{bh^2(b+h)}, \\ \phi_n^{(F_z, 3)}(s_2) = \phi_n^{(F_z, 3)}(s_4) &= \frac{-s(2h^2b + 3hb^2 - 4hs^2 - b^3 + 4bs^2)}{hb^2(b+h)} \end{aligned} \quad (\text{A.25})$$

$$\begin{aligned} \phi_s^{(M_x, 1)}(s_1) = -\phi_s^{(M_x, 1)}(s_3) &= \frac{s^2}{2} - \frac{h^2}{24}, \quad \phi_s^{(M_x, 1)}(s_2) = -\phi_s^{(M_x, 1)}(s_4) = \frac{hs}{2} \\ \phi_n^{(M_x, 1)}(s_1) = -\phi_n^{(M_x, 1)}(s_3) &= \frac{bs}{2}, \\ \phi_n^{(M_x, 1)}(s_2) = -\phi_n^{(M_x, 1)}(s_4) &= \frac{15b^4 + 8b^2h^2 - 72b^2s^2 + 48s^4}{96b^2} \end{aligned} \quad (\text{A.26})$$

$$\phi_z^{(M_x, 2)}(s_{ed}) = \sigma_{zz}^{M_x}(s_{ed}) \quad (\text{A.27})$$

$$\begin{aligned} \phi_s^{(M_x, 3)}(s_{ed}) &= \sigma_{zz}^{M_x}(s_{ed}) \\ \phi_n^{(M_x, 3)}(s_1) = -\phi_n^{(M_x, 3)}(s_3) &= \frac{-8bh^3 + 5h^4 - 24h^2s^2 + 16s^4}{16bh^2}, \\ \phi_n^{(M_x, 3)}(s_2) = -\phi_n^{(M_x, 3)}(s_4) &= \frac{-hs}{b} \end{aligned} \quad (\text{A.28})$$

$$\phi_z^{(M_x, 4)}(s_1) = -\phi_z^{(M_x, 4)}(s_3) = \frac{s^2}{2} - \left(\frac{h^2}{8} + \frac{bh}{4}\right), \quad \phi_z^{(M_x, 4)}(s_2) = -\phi_z^{(M_x, 4)}(s_4) = \frac{hs}{2} \quad (\text{A.29})$$

$$\begin{aligned} \phi_s^{(M_y, 1)}(s_1) = -\phi_s^{(M_y, 1)}(s_3) &= \frac{-bs}{2}, \quad \phi_s^{(M_y, 1)}(s_2) = -\phi_s^{(M_y, 1)}(s_4) = \frac{s^2}{2} - \frac{b^2}{24} \\ \phi_n^{(M_y, 1)}(s_1) = -\phi_n^{(M_y, 1)}(s_3) &= -\frac{15h^4 + 8b^2h^2 - 72h^2s^2 + 48s^4}{96h^2}, \\ \phi_n^{(M_y, 1)}(s_2) = -\phi_n^{(M_y, 1)}(s_4) &= \frac{hs}{2} \end{aligned} \quad (\text{A.30})$$

$$\phi_z^{(M_y, 2)}(s_{ed}) = \sigma_{zz}^{M_y}(s_{ed}) \quad (\text{A.31})$$

$$\begin{aligned}
\phi_s^{(M_y, 3)}(s_{ed}) &= \sigma_{zz}^{M_y}(s_{ed}) \\
\phi_n^{(M_y, 3)}(s_1) &= -\phi_n^{(M_y, 3)}(s_3) = \frac{bs}{h}, \\
\phi_n^{(M_y, 3)}(s_2) &= -\phi_n^{(M_y, 3)}(s_4) = \frac{-8hb^3 + 5b^4 - 24b^2s^2 + 16s^4}{16hb^2}
\end{aligned} \tag{A.32}$$

$$\phi_z^{(M_y, 4)}(s_1) = -\phi_z^{(M_y, 4)}(s_3) = \frac{-bs}{2}, \quad \phi_z^{(M_y, 4)}(s_2) = -\phi_z^{(M_y, 4)}(s_4) = \frac{s^2}{2} - \left(\frac{b^2}{8} + \frac{bh}{4}\right) \tag{A.33}$$

$$\begin{aligned}
\phi_s^{(B_L, 1)}(s_1) &= \phi_s^{(B_L, 1)}(s_3) = \frac{bs^2}{4} - \frac{bh^2}{48}, \quad \phi_s^{(B_L, 1)}(s_2) = \phi_s^{(B_L, 1)}(s_4) = -\frac{hs^2}{4} + \frac{hb^2}{48} \\
\phi_n^{(B_L, 1)}(s_1) &= \phi_n^{(B_L, 1)}(s_3) = \frac{hs(2b^3 + 3b^2h + h^3) - 4s^3(b^2 + h^2)}{24h(b+h)}, \\
\phi_n^{(B_L, 1)}(s_2) &= \phi_n^{(B_L, 1)}(s_4) = \frac{4s^3(b^2 + h^2) - bs(2h^3 + 3h^2b + b^3)}{24b(b+h)}
\end{aligned} \tag{A.34}$$

$$\phi_z^{(B_L, 2)}(s_{ed}) = \sigma_{zz}^{B_L}(s_{ed}) \tag{A.35}$$

$$\begin{aligned}
\phi_s^{(B_L, 3)}(s_{ed}) &= \sigma_{zz}^{B_L}(s_{ed}) \\
\phi_n^{(B_L, 3)}(s_{ed}) &= \frac{(-1)^{ed}bh}{4}
\end{aligned} \tag{A.36}$$

$$\begin{aligned}
\phi_z^{(B_L, 4)}(s_1) &= \phi_z^{(B_L, 4)}(s_3) = \frac{bs^2}{4} - \frac{bh(2b+h)}{48}, \\
\phi_z^{(B_L, 4)}(s_2) &= \phi_z^{(B_L, 4)}(s_4) = \frac{-hs^2}{4} + \frac{bh(b+2h)}{48}
\end{aligned} \tag{A.37}$$

Note that the cross-section deformation functions of modes 1 and 2 are the same as those defined for isotropic materials, while the cross-section deformation functions of modes 3 and 4 are newly derived because of the non-zero \bar{S}_{62} term for anisotropic materials. Because $\phi_z^{(F_z, 4)}$ cannot satisfy the axial edge continuity, making its actual occurrence difficult, we do not consider it as a cross-section

deformation function in this study.

Let us now consider the case of in-plane loading. In this case, the in-plane loads cause shear stress $\sigma_{sz}^\zeta(s)$ in the wall, as shown in Fig. A.4 ($\zeta \in \{F_x, F_y, M_z, B_T\}$). For non-zero $\sigma_{sz}^\zeta(s)$, one can find the following relations:

$$\varepsilon_{sx}^\zeta(s, z) = \bar{S}_{16} \sigma_{sz}^\zeta(s) \zeta(z) \quad (\text{A.38})$$

$$\varepsilon_{zz}^\zeta(s, z) = \bar{S}_{26} \sigma_{sz}^\zeta(s) \zeta(z) \quad (\text{A.39})$$

$$2\varepsilon_{sz}^\zeta(s, z) = \bar{S}_{66} \sigma_{sz}^\zeta(s) \zeta(z) \quad (\text{A.40})$$

By using Eqs. (A.38-40) and the equations defining strains such as Eqs. (A.13-15), the following cross-section deformation functions can be defined in a manner similar to Eqs. (A.16-22).

$$\phi_s^{(\zeta, 1)}(s) = \int \sigma_{sz}^\zeta(s) ds \quad (\text{A.41})$$

$$\bar{S}_{16} \zeta(z) = \delta^{(\zeta, 1)}(z) \quad (\text{A.42})$$

$$\phi_z^{(\zeta, 2)}(s) = \sigma_{sz}^\zeta(s) \quad (\text{A.43})$$

$$\bar{S}_{26} \zeta(z) = \delta^{(\zeta, 2)}(z) \quad (\text{A.44})$$

$$\phi_s^{(\zeta, 3)}(s) = \sigma_{sz}^\zeta(s) \quad (\text{A.45})$$

$$\phi_z^{(\zeta, 4)}(s) = \int \sigma_{sz}^\zeta(s) ds \quad (\text{A.46})$$

$$\bar{S}_{66} \zeta(z) = \delta^{(\zeta, 3)}(z) + \delta^{(\zeta, 4)}(z) \quad (\text{A.47})$$

Following the analysis step discussed for the case of out-of-plane loads, the cross-

section deformation functions for in-plane loads are derived below and are sketched in Fig. A.4.

$$\begin{aligned}
\phi_s^{(F_x, 1)}(s_1) &= -\phi_s^{(F_x, 1)}(s_3) = \frac{b^2}{5} + \frac{h^2}{12} - s^2, \\
\phi_s^{(F_x, 1)}(s_2) &= -\phi_s^{(F_x, 1)}(s_4) = \frac{-s(3b^2 + 6hb - 4s^2)}{6b} \\
\phi_n^{(F_x, 1)}(s_1) &= -\phi_n^{(F_x, 1)}(s_3) = -s\left(\frac{b^2}{3h} + b\right), \\
\phi_n^{(F_x, 1)}(s_2) &= -\phi_n^{(F_x, 1)}(s_4) = -\frac{s^4}{b^2} - \frac{9b^2}{80} - \frac{s^4}{3bh} + \frac{24bs^2 - 5b^3}{48h} - \frac{h^2}{6} + \frac{3s^2}{2}
\end{aligned} \tag{A.48}$$

$$\phi_z^{(F_x, 2)}(s_{ed}) = \sigma_{sz}^{F_x}(s_{ed}) \tag{A.49}$$

$$\begin{aligned}
\phi_s^{(F_x, 3)}(s_{ed}) &= \sigma_{sz}^{F_x}(s_{ed}) \\
\phi_n^{(F_x, 3)}(s_1) &= -\phi_n^{(F_x, 3)}(s_3) = \frac{8bh^3 - 5h^4 + 24h^2s^2 - 16s^4}{8bh^2}, \\
\phi_n^{(F_x, 3)}(s_2) &= -\phi_n^{(F_x, 3)}(s_4) = \frac{2hs}{b}
\end{aligned} \tag{A.50}$$

$$\begin{aligned}
\phi_z^{(F_x, 4)}(s_1) &= -\phi_z^{(F_x, 4)}(s_3) = -s^2 + \frac{3h^2 - 4b^2 - 6bh}{12}, \\
\phi_z^{(F_x, 4)}(s_2) &= -\phi_z^{(F_x, 4)}(s_4) = \frac{2s^3}{3b} - \left(\frac{b}{2} + h\right)s
\end{aligned} \tag{A.51}$$

$$\begin{aligned}
\phi_s^{(F_y, 1)}(s_1) &= -\phi_s^{(F_y, 1)}(s_3) = \frac{s(3h^2 + 6hb - 4s^2)}{6h}, \\
\phi_s^{(F_y, 1)}(s_2) &= -\phi_s^{(F_y, 1)}(s_4) = \frac{h^2}{5} + \frac{b^2}{12} - s^2 \\
\phi_n^{(F_y, 1)}(s_1) &= -\phi_n^{(F_y, 1)}(s_3) = \frac{5h^3 - 24hs^2}{48b} + \frac{s^4}{h^2} + \frac{9h^2}{80} + \frac{s^4}{3bh} + \frac{b^2}{6} - \frac{3s^2}{2}, \\
\phi_n^{(F_y, 1)}(s_2) &= -\phi_n^{(F_y, 1)}(s_4) = -s\left(\frac{h^2}{3b} + h\right)
\end{aligned} \tag{A.52}$$

$$\phi_z^{(F_y, 2)}(s_{ed}) = \sigma_{sz}^{F_y}(s_{ed}) \tag{A.53}$$

$$\begin{aligned}
\phi_s^{(F_y, 3)}(s_{ed}) &= \sigma_{sz}^{F_y}(s_{ed}) \\
\phi_n^{(F_y, 3)}(s_1) &= -\phi_n^{(F_y, 3)}(s_3) = \frac{-2bs}{h}, \\
\phi_n^{(F_y, 3)}(s_2) &= -\phi_n^{(F_y, 3)}(s_4) = \frac{8hb^3 - 5b^4 + 24b^2s^2 - 16s^4}{8hb^2}
\end{aligned} \tag{A.54}$$

$$\begin{aligned}
\phi_z^{(F_y, 4)}(s_1) &= -\phi_z^{(F_y, 4)}(s_3) = \left(\frac{h}{2} + b\right)s - \frac{2s^3}{3h}, \\
\phi_z^{(F_y, 4)}(s_2) &= -\phi_z^{(F_y, 4)}(s_4) = -s^2 + \frac{3b^2 - 4h^2 - 6bh}{12}
\end{aligned} \tag{A.55}$$

$$\begin{aligned}
\phi_s^{(M_z, 1)}(s_{ed}) &= \phi_s^{(F_z, 1)}(s_{ed}) \\
\phi_n^{(M_z, 1)}(s_{ed}) &= \phi_n^{(F_z, 1)}(s_{ed})
\end{aligned} \tag{A.56}$$

$$\phi_z^{(M_z, 2)}(s_{ed}) = \phi_z^{(F_z, 2)}(s_{ed}) \tag{A.57}$$

$$\begin{aligned}
\phi_s^{(M_z, 3)}(s_{ed}) &= \phi_s^{(F_z, 3)}(s_{ed}) \\
\phi_n^{(M_z, 3)}(s_{ed}) &= \phi_n^{(F_z, 3)}(s_{ed})
\end{aligned} \tag{A.58}$$

$$\begin{aligned}
\phi_s^{(B_r, 1)}(s_{ed}) &= (-1)^{ed+1} s \\
\phi_n^{(B_r, 1)}(s_1) &= \phi_n^{(B_r, 1)}(s_3) = \frac{-b}{2}, \quad \phi_n^{(B_r, 1)}(s_2) = \phi_n^{(B_r, 1)}(s_4) = \frac{h}{2}
\end{aligned} \tag{A.59}$$

$$\begin{aligned}
\phi_s^{(B_r, 3)}(s_{ed}) &= \sigma_{sz}^{B_r}(s_{ed}) \\
\phi_n^{(B_r, 3)}(s_1) &= \phi_n^{(B_r, 3)}(s_3) = \frac{s(h^2 + 2bh - 4s^2)}{bh^2}, \\
\phi_n^{(B_r, 3)}(s_2) &= \phi_n^{(B_r, 3)}(s_4) = -\frac{s(b^2 + 2bh - 4s^2)}{hb^2}
\end{aligned} \tag{A.60}$$

Modes 3 and 4 represent the same cross-sectional deformations that occur in isotropic materials, while modes 1 and 2 depict the additional cross-sectional deformations occurring in anisotropic materials, because \bar{S}_{16} and \bar{S}_{26} are non-zero in anisotropic materials. It is in the same context that modes 3 and 4 for out-

of-plane loads occur only in composite materials. In Fig. A.4, $\phi_z^{(M_z, 4)}$, $\phi_z^{(B_T, 2)}$, $\phi_z^{(B_T, 4)}$ are not defined for the same reason why $\phi_z^{(F_z, 4)}$ was not defined.

A.3 Definition of sectional shape functions for degrees of freedom

The sectional shape functions corresponding to the degrees of freedom used for higher-order beam analysis are depicted in Fig. A.5. The sectional shape functions are defined along the centerline of the walls of the beam cross section. In Fig. A.5, the eight sectional shape functions indicated by “*Vlasov beam deformation configurations*” are related to six rigid-body degrees of freedom for the box beam section, and two non-rigid-body degrees of freedom (warping W and distortion χ).

We choose the first eight degrees of freedom (ξ_1 to ξ_8) as $U_x, U_y, U_z, \theta_x, \theta_y, \theta_z, W$, and χ in order. (The symbol ξ_k is used to denote the k -th degree of freedom.) They were used in the existing higher-order beam theory [34, 39] and Vlasov beam theory [11]. The corresponding sectional shape functions $\xi_k \psi_n (k=1, \dots, 8)$ are given below. They will be called the “*Vlasov sectional shape functions*.”

$$\begin{aligned} \xi_1 \psi_s(s_1) = \xi_1 \psi_s(s_3) = 0, \quad \xi_1 \psi_s(s_2) = -\xi_1 \psi_s(s_4) = -1 \\ \xi_1 \psi_n(s_1) = -\xi_1 \psi_n(s_3) = 1, \quad \xi_1 \psi_n(s_2) = \xi_1 \psi_n(s_4) = 0 \end{aligned} \quad (\text{A.61})$$

$$\begin{aligned} \xi_2 \psi_s(s_1) = -\xi_2 \psi_s(s_3) = 1, \quad \xi_2 \psi_s(s_2) = \xi_2 \psi_s(s_4) = 0 \\ \xi_2 \psi_n(s_1) = \xi_2 \psi_n(s_3) = 0, \quad \xi_2 \psi_n(s_2) = -\xi_2 \psi_n(s_4) = 1 \end{aligned} \quad (\text{A.62})$$

$$\xi_3 \psi_z(s_{ed}) = 1 \quad (\text{A.63})$$

$$\xi_4 \psi_z(s_1) = -\xi_4 \psi_z(s_3) = -s, \quad \xi_4 \psi_z(s_2) = -\xi_4 \psi_z(s_4) = \frac{-h}{2} \quad (\text{A.64})$$

$$\xi_5 \psi_z(s_1) = -\xi_5 \psi_z(s_3) = \frac{-b}{2}, \quad \xi_5 \psi_z(s_2) = -\xi_5 \psi_z(s_4) = s \quad (\text{A.65})$$

$$\xi_6 \psi_s(s_1) = \xi_6 \psi_s(s_3) = \frac{b}{2}, \quad \xi_6 \psi_s(s_2) = \xi_6 \psi_s(s_4) = \frac{h}{2} \quad (\text{A.66})$$

$$\xi_6 \psi_n(s_{ed}) = -s$$

$$\xi_7 \psi_z(s_1) = \xi_7 \psi_z(s_3) = \frac{bs}{2}, \quad \xi_7 \psi_z(s_2) = \xi_7 \psi_z(s_4) = \frac{-hs}{2} \quad (\text{A.67})$$

$$\xi_8 \psi_s(s_{ed}) = \frac{(-1)^{ed+1} bh}{b+h}$$

$$\xi_8 \psi_n(s_1) = \xi_8 \psi_n(s_3) = \frac{-4s^3}{h(b+h)} + \frac{(2b+h)s}{b+h}, \quad (\text{A.68})$$

$$\xi_8 \psi_n(s_2) = \xi_8 \psi_n(s_4) = \frac{4s^3}{b(b+h)} - \frac{(b+2h)s}{b+h}$$

Additional degrees of freedom are associated with $\phi_\eta^{(\zeta, m_n)}$ derived in the previous sections. Referring to Figs. A.3-A.4, it appears that there may be 28 additional degrees of freedom altogether. However, they are not all independent of each other. If they were independent, $\phi_\eta^{(\zeta, m_n)}$ could be directly used as $\xi_k \psi_\eta$. Therefore, a procedure that takes only the independent degrees of freedom must be considered. Furthermore, the resulting independent degrees of freedom must be also independent of the eight Vlasov degrees of freedom. Here, we will use the Gram-Schmidt orthogonalization process as a means to select independent degrees of freedom. We note that 14 cross-section deformation functions shown in the columns of modes 1 and 2 in Fig. A.3 and modes 3 and 4 in Fig. A.4 also appear

for isotropic box beams. For this reason, they will be called the isotropic cross-section deformation functions. On the other hand, the 14 cross-section deformation functions shown in the columns of modes 3 and 4 in Fig. A.3 and modes 1 and 2 in Fig. A.4 appear only for anisotropic box beams. Therefore, they will be called the anisotropic cross-section deformation functions.

By applying the Gram–Schmidt process, one can identify the sectional shape function, $\xi_k \psi_\eta$, which corresponds to the orthogonal degrees of freedom:

$$\xi_k \psi_z = \phi_z^{(\zeta, m)} - \sum_{j=1}^{k-1} \xi_j \psi_z \frac{\langle \phi_z^{(\zeta, m_n)} \xi_j \psi_z \rangle}{\langle \xi_j \psi_z \xi_j \psi_z \rangle} \quad (\text{A.69})$$

$$\xi_k \psi_s = \phi_s^{(\zeta, m)} - \sum_{j=1}^{k-1} \xi_j \psi_s \frac{\langle \phi_s^{(\zeta, m_n)} \xi_j \psi_s \rangle}{\langle \xi_j \psi_s \xi_j \psi_s \rangle} \quad (\text{A.70})$$

$$\xi_k \psi_n = \phi_n^{(\zeta, m)} - \sum_{j=1}^{k-1} \xi_j \psi_n \frac{\langle \phi_n^{(\zeta, m_n)} \xi_j \psi_n \rangle}{\langle \xi_j \psi_n \xi_j \psi_n \rangle} \quad (\text{A.71})$$

where $k=9, 10, \dots$, and the operator, $\langle \rangle$, denotes the integration along the s -axis. For the isotropic cross-section deformation functions, it is found that there are only six independent degrees of freedom (ξ_9 to ξ_{14}) and the corresponding isotropic sectional shape functions are shown in the second row of Fig. A.5. For the anisotropic cross-section deformation functions, it is found that eight additional independent degrees of freedom (ξ_{15} to ξ_{22}) exist and the corresponding anisotropic sectional shape functions are shown in the third row of Fig. A.5.

Aside from the degrees of freedom considered so far, sectional shape functions depicting only the bending deformation of the wall plate should be also included. The importance of wall bending deformations was addressed in previous studies on composite beam analysis [59, 78], and also in the vibration and joint analysis of the higher-order beam theory [38, 39]. The specific forms of the selected four sectional shape functions listed below are defined in [38], and they are shown in the last row of Fig. A.5. The corresponding degrees of freedom are denoted by $\xi_{23}-\xi_{26}$.

$$\begin{aligned}\xi_{23} \psi_n(s_1) = \xi_{23} \psi_n(s_3) &= \frac{16s^4(b+h)}{h^4(5b+h)} - \frac{8s^2(3b+h)}{h^2(5b+h)} + 1, \\ \xi_{23} \psi_n(s_2) = \xi_{23} \psi_n(s_4) &= \frac{16s^2 - 4b^2}{h(5b+h)}\end{aligned}\quad (\text{A.72})$$

$$\begin{aligned}\xi_{24} \psi_n(s_1) = \xi_{24} \psi_n(s_3) &= \frac{16s^2 - 4h^2}{b(5h+b)}, \\ \xi_{24} \psi_n(s_2) = \xi_{24} \psi_n(s_4) &= \frac{16s^4(b+h)}{b^4(5h+b)} - \frac{8s^2(3h+b)}{b^2(5h+b)} + 1\end{aligned}\quad (\text{A.73})$$

$$\begin{aligned}\xi_{25} \psi_n(s_1) = -\xi_{25} \psi_n(s_3) &= \frac{16s^4(b+3h)}{h^4(5b+3h)} - \frac{24s^2(b+h)}{h^2(5b+3h)} + 1, \\ \xi_{25} \psi_n(s_2) = -\xi_{25} \psi_n(s_4) &= \frac{s(8b^2 - 32s^2)}{b(5bh + 3h^2)}\end{aligned}\quad (\text{A.74})$$

$$\begin{aligned}\xi_{26} \psi_n(s_1) = -\xi_{26} \psi_n(s_3) &= \frac{s(32s^2 - 8h^2)}{h(5bh + 3b^2)}, \\ \xi_{26} \psi_n(s_2) = -\xi_{26} \psi_n(s_4) &= \frac{16s^4(h+3b)}{b^4(5h+3b)} - \frac{24s^2(b+h)}{b^2(5h+3b)} + 1\end{aligned}\quad (\text{A.75})$$

Therefore, we have developed a higher-order beam theory using 26 degrees of freedom for the analysis of general composite thin-walled box beam.

A.4 Examples

Here, we present the numerical results based on the proposed theory for composite thin-walled box beams with various conditions. The validity of the proposed theory is verified by comparing the present results with the results obtained by the S8R shell elements of ABAQUS [75]. Lower-order S4R elements (which also exhibit similar accuracy to S8R elements) may be used, but we used higher-order S8R elements because our beam elements are based on the Hermite interpolation scheme requiring quadratic functions. In Examples 1–2, the numerical results based on our theory for composite thin-walled box beams are checked with different numbers of elements, beam lengths, and thicknesses, respectively. The effect of the number of degrees of freedom is examined in Example 3. Example 4 considers composite thin-walled box beams composed of plies at arbitrary angles for which static and eigenvalue problems are solved.

Example 1

This example considers the effects of the interpolation for finite element calculations. The geometric dimensions and material properties for the analysis of the beam are as follows: $L=1000$ mm, $b=100$ mm, $h=50$ mm, and $t=3$ mm, $E_L = 141.96$ GPa, $E_T = 9.79$ GPa, $G_{LT} = 6$ GPa, and $\nu_{LT} = 0.42$. The beam has six plies with the same thickness and is stacked at $[0^\circ/45^\circ]_3$. One side of the composite thin-walled box beam is fixed and the opposite side is subjected to a

bending moment (1 Nm) or a torsional load (1 Nm). The number of axial elements was changed for the linear and Hermite interpolations, and the numerical results were compared with those obtained using ABAQUS shell elements. Figures A.6 (a) and (b) show the errors of the bending and torsional rotations at the beam end by the bending and torsional moments, respectively. For the present higher-order beam theory analysis, 26 degrees of freedom were used for the sectional shape functions

In the case where the Hermite interpolation is used, the error becomes within 1-2% even if only ten finite elements are used. When 20 or more elements are used, nearly convergent results are obtained. However, in a case where linear interpolation is used, the error reduces to below 2% when more than 50 elements are used. Furthermore, the relative error obtained by the linear interpolation appears to be always larger than that obtained by the Hermite interpolation; it is larger by more than 1%. The error obtained by the linear interpolation may be inevitable because some of the strain energy caused by plate bending cannot be properly represented by the linear interpolation; in Eq. (2.6), the n -directional displacement is differentiated twice in the z coordinate. Therefore, shall hereafter employ the Hermite interpolation. In addition, 40 elements are used in the axial direction to ensure convergence.

Example 2

The aim of Example 2 is to show that the present results are sufficiently accurate

and comparable with the shell results. Specifically, we vary the length and thickness of the composite thin-walled box beams, and the geometric data, material properties, ply lamination, boundary conditions, and loading conditions (except length and thickness) are the same as in Example 1. Tables A.1 and A.2 show bending and torsional rotations at the end, while increasing the thickness of the member from 1.5-9 mm with the beam length fixed at 1000 mm. As the member becomes thicker, the analysis error becomes larger overall. However, even if the thickness reaches 9 mm, an error no greater than 2.5% occurs. Therefore, the proposed theory is found to be valid for the thin-walled aspect ratio assumed in this study.

In Tables A.3 and A.4, the length of the beam was reduced from 2000 mm to 250 mm with the beam thickness fixed at 6 mm, and bending and torsional rotations were observed at the beam end. The shorter the length of the member, the larger the analysis error. However, even if the beam length is 250 mm, the error is within 2.5%, so it is clear that our higher-order beam theory for composite thin-walled box beams is valid for the beam aspect ratio assumed in this study.

Example 3

In this example, we will investigate the effect of the number of sectional deformation degrees of freedom used for analysis. All conditions except beam thickness and ply angle are shown in Example 1. The ply is a single ply with a

thickness of 6 mm and an angle of 30° . Figure A.7 (a) plots the axial variation of the three-dimensional displacements at the point where s is $b/2$ at the center of wall 2, when the beam is subjected to the bending moment. Figure A.7 (b) shows the three-dimensional displacements at the point where s is $b/2$ at the center of wall 4. Figure A.8 presents the results when the torsional moment is imposed at the beam end. The numerical studies in Figs. A.7-A.8 suggest that the composite thin-walled box beam stiffness cannot be correctly evaluated if only the lowest eight degrees of freedom (which are used in the Vlasov beam theory) are used. When 18 degrees of freedom are used, excluding the anisotropic plane-stress related deformation degrees of freedom ($\xi_{15} - \xi_{22}$), the results become closer to the shell results. However, there are still several errors that cannot be overcome, especially near the loaded end. In the case where all 26 proposed degrees of freedom are used, the results are confirmed to be almost the same as those of the shell analysis, which supports the validity of this theory.

Example 4

In this example, a composite thin-walled box beam stacked with randomly oriented plies is analyzed. The beam is stacked with six plies, $[35^\circ/-55^\circ/-10^\circ/80^\circ/-55^\circ/35^\circ]$, while the other conditions are set the same as in Example 3. Figure A.9 (a) plots the three-dimensional displacement at the point where $s=0$ at the center of wall 1, when the beam is subjected to the bending moment. Figure A.9 (b) plots the stress

distribution in the outermost ply at the point where $s=b/40$ of wall 1. For this example, we used 80 higher-order beam elements to calculate the local stress at both ends in more detail. Figures A.10 (a) and (b) show the results for the torsional moment loading case; the three-dimensional displacement and stress are plotted at the same positions as in Fig. A.9. From the results in Figs. A.9-A.10, it is confirmed that our higher-order beam theory for composite thin-walled box beams yields results that are sufficiently close to those predicted by the shell theory.

Finally, the free vibration analysis of the same beam is carried out ($\rho = 1445$ kg/m³). The results obtained by the proposed higher-order beam theory shown in Fig. A.11 (b) agree with those by the ABAQUS shell analysis in Fig. A.11 (a); an average error of 1.41% and the maximum error of 3.88% are calculated for the lowest five modes.

Table A.1 Bending rotation predicted for various beam thickness by the proposed higher-order beam approach at the tip of composite box beam, and the relative errors with respect to the shell calculation

t (mm)	1.5	3	6	9
Shell (rad)	5.78821E-05	2.91095E-05	1.47031E-05	9.88165E-06
Proposed (rad)	5.77853E-05	2.90613E-05	1.46776E-05	9.86274E-06
Error (%)	0.167280	0.165633	0.173209	0.191329

Table A.2 Torsional rotation predicted for various beam thicknesses by the proposed higher-order beam approach at the tip of composite box beam, and the relative errors with respect to the shell calculation

t (mm)	1.5	3	6	9
Shell (rad)	3.22447E-04	1.15693E-04	4.83773E-05	2.99818E-05
Proposed (rad)	3.20281E-04	1.14559E-04	4.76448E-05	2.92764E-05
Error (%)	0.671719	0.980271	1.51413	2.35280

Table A.3 Bending rotation predicted for various lengths by the proposed higher-order beam approach at the tip of composite box beam, and the relative errors with respect to the shell calculation

L (mm)	2000	1000	500	250
Shell (rad)	5.82165.E-05	2.91095.E-05	1.45561.E-05	7.27937.E-06
Proposed (rad)	5.81263.E-05	2.90613.E-05	1.45280.E-05	7.26105.E-06
Error (%)	0.154917	0.165633	0.193074	0.251618

Table A.4 Torsional rotation predicted for various lengths by the proposed higher-order beam approach at the tip of composite box beam, and the relative errors with respect to the shell calculation

L (mm)	2000	1000	500	250
Shell (rad)	2.05565.E-04	1.15693.E-04	6.89469.E-05	3.20396.E-05
Proposed (rad)	2.04162.E-04	1.14559.E-04	6.80058.E-05	3.12696.E-05
Error (%)	0.682461	0.980271	1.36495	2.40344

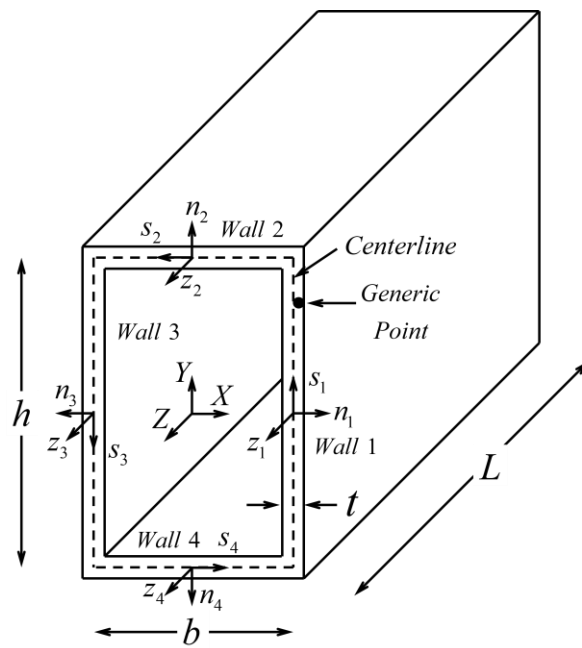


Fig. A.1 The coordinate system used for the analysis of the composite thin-walled box beam and the detail geometry parameters

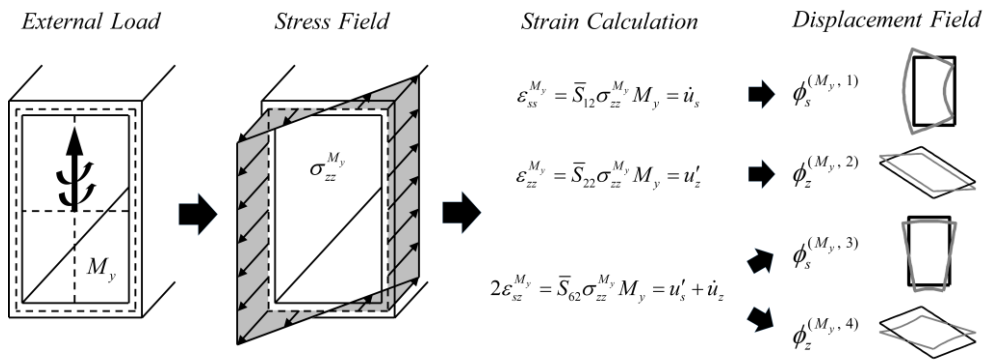


Fig. A.2 Schematic to explain the process to derive the displacement field associated with M_y

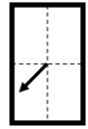
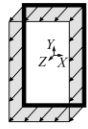

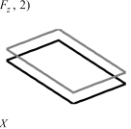

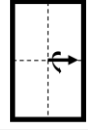


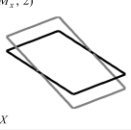

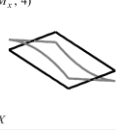
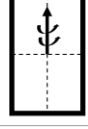
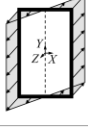

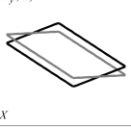

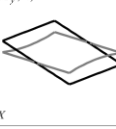
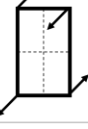
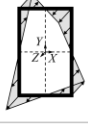

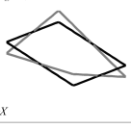

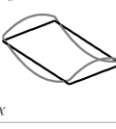
Resultant Force	Stress Distribution	Mode 1	Mode 2	Mode 3	Mode 4
F_z 	$\sigma_{zz}^{F_z}$ 	$\phi^{(F_z, 1)}$ 	$\phi^{(F_z, 2)}$ 	$\phi^{(F_z, 3)}$ 	N / A
M_x 	$\sigma_{zz}^{M_x}$ 	$\phi^{(M_x, 1)}$ 	$\phi^{(M_x, 2)}$ 	$\phi^{(M_x, 3)}$ 	$\phi^{(M_x, 4)}$ 
M_y 	$\sigma_{zz}^{M_y}$ 	$\phi^{(M_y, 1)}$ 	$\phi^{(M_y, 2)}$ 	$\phi^{(M_y, 3)}$ 	$\phi^{(M_y, 4)}$ 
B_L 	$\sigma_{zz}^{B_L}$ 	$\phi^{(B_L, 1)}$ 	$\phi^{(B_L, 2)}$ 	$\phi^{(B_L, 3)}$ 	$\phi^{(B_L, 4)}$ 

Fig. A.3 Derived cross-section deformation functions associated with out-of-plane loads

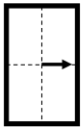
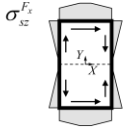
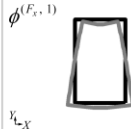
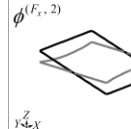
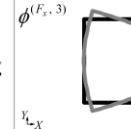
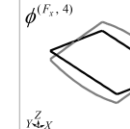
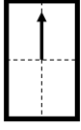
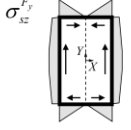
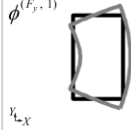
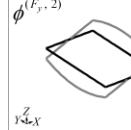
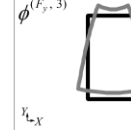
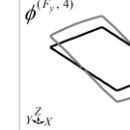
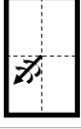
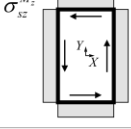
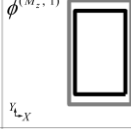
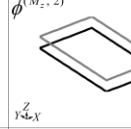
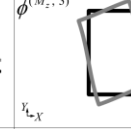
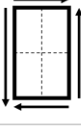
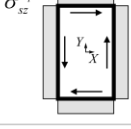
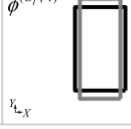
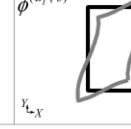
Resultant Force	Stress Distribution	Mode 1	Mode 2	Mode 3	Mode 4
F_x 	$\sigma_{xz}^{F_x}$ 	$\phi^{(F_x, 1)}$  y_{L-X}	$\phi^{(F_x, 2)}$  y_{L-X}^Z	$\phi^{(F_x, 3)}$  y_{L-X}	$\phi^{(F_x, 4)}$  y_{L-X}^Z
F_y 	$\sigma_{xz}^{F_y}$ 	$\phi^{(F_y, 1)}$  y_{L-X}	$\phi^{(F_y, 2)}$  y_{L-X}^Z	$\phi^{(F_y, 3)}$  y_{L-X}	$\phi^{(F_y, 4)}$  y_{L-X}^Z
M_z 	$\sigma_{xz}^{M_z}$ 	$\phi^{(M_z, 1)}$  y_{L-X}	$\phi^{(M_z, 2)}$  y_{L-X}^Z	$\phi^{(M_z, 3)}$  y_{L-X}	N / A
B_T 	$\sigma_{xz}^{B_T}$ 	$\phi^{(B_T, 1)}$  y_{L-X}	N / A	$\phi^{(B_T, 3)}$  y_{L-X}	N / A

Fig. A.4 Derived cross-section deformation functions associated with in-plane loads

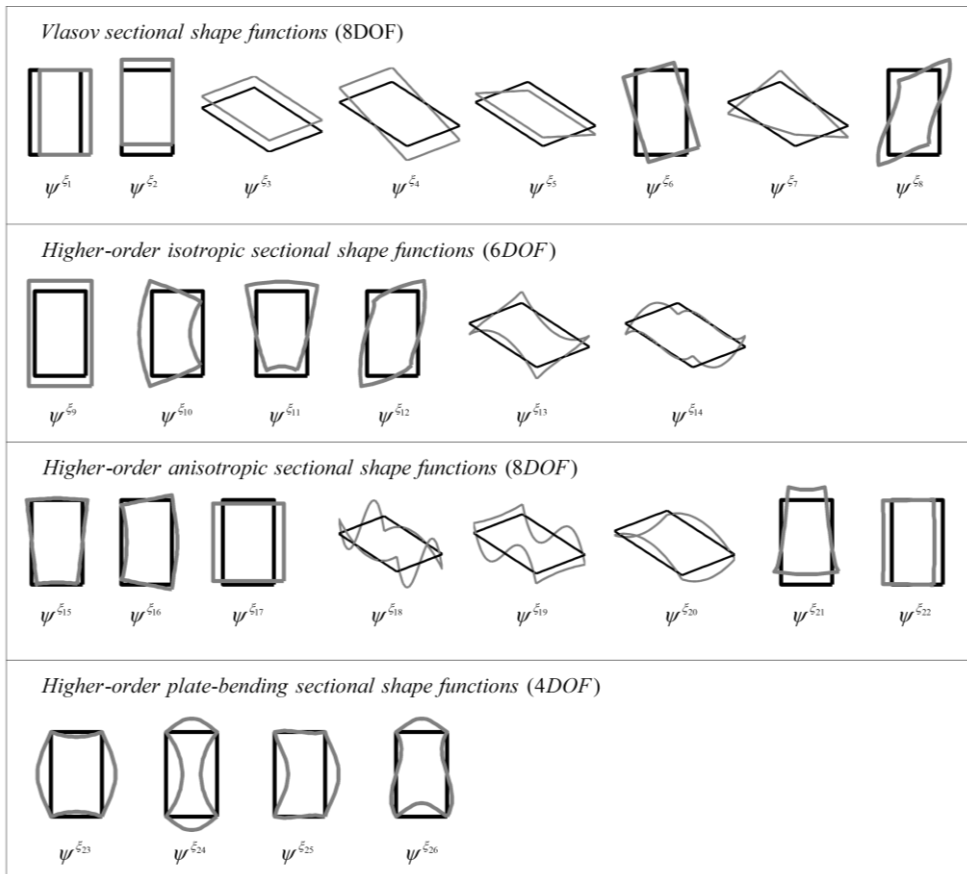


Fig. A.5 Sectional shape functions for the degrees of freedom employed in the Higher-order Beam Theory for composite thin-walled box beams

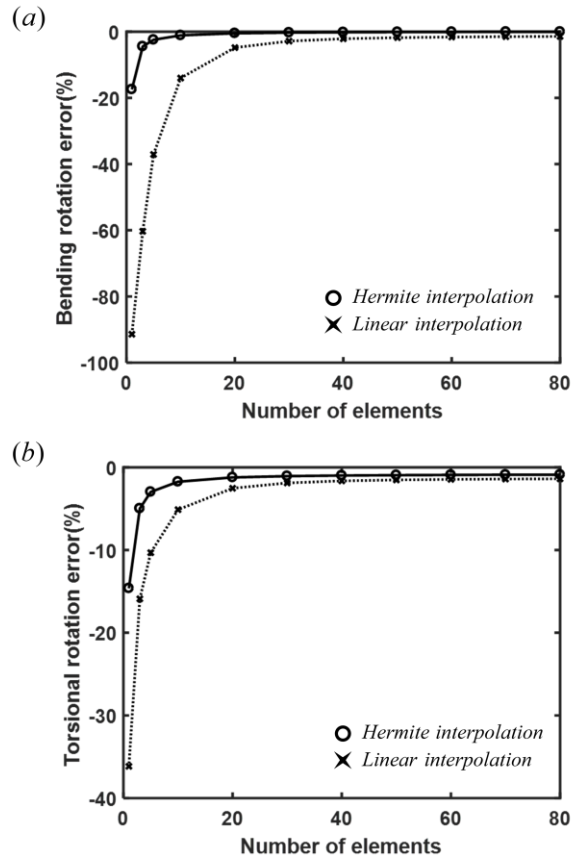


Fig. A.6 Numerical results for Example 1 in Appendix A to examine the effects of the linear and Hermite finite element interpolation functions. The composite box beam is subjected to (a) bending moment and (b) torsional moment

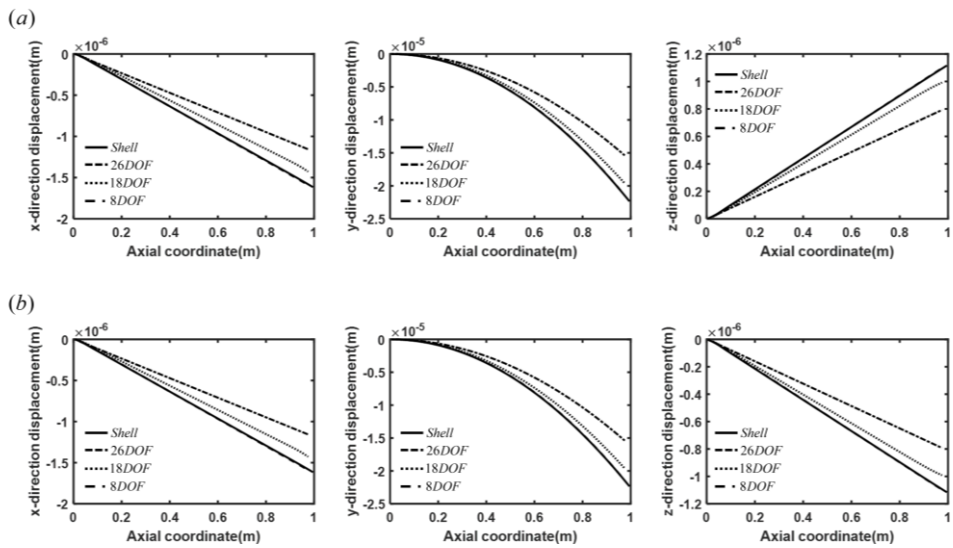


Fig. A.7 Numerical results for Example 3 in Appendix A in a single-layer composite thin-walled box beam under bending moment. Three-dimensional displacements at $s=b/2$ at the center of (a) wall 2 and (b) wall 4

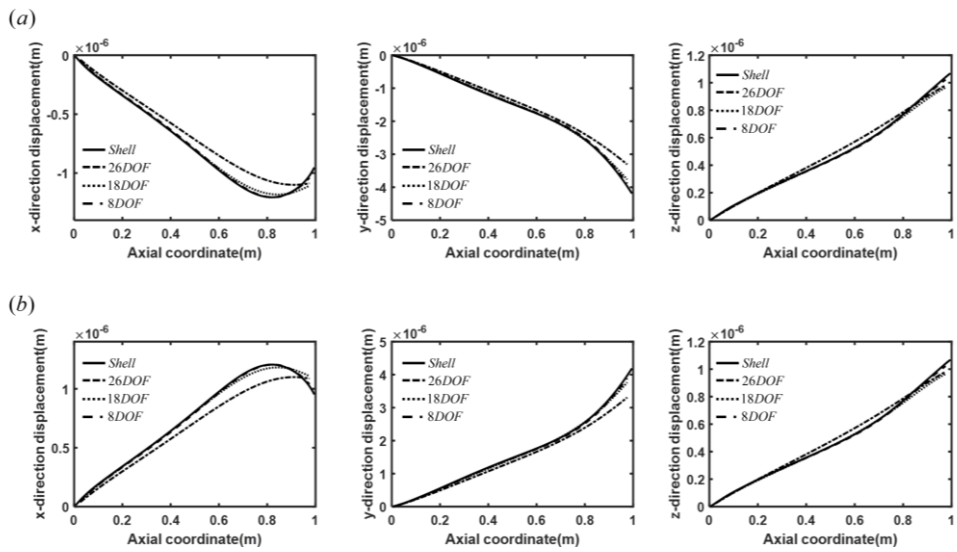


Fig. A.8 Numerical results for Example 3 in Appendix A in a single-layer composite thin-walled box beam under torsional moment. Three-dimensional displacements at $s=b/2$ at the center of (a) wall 2 and (b) wall 4

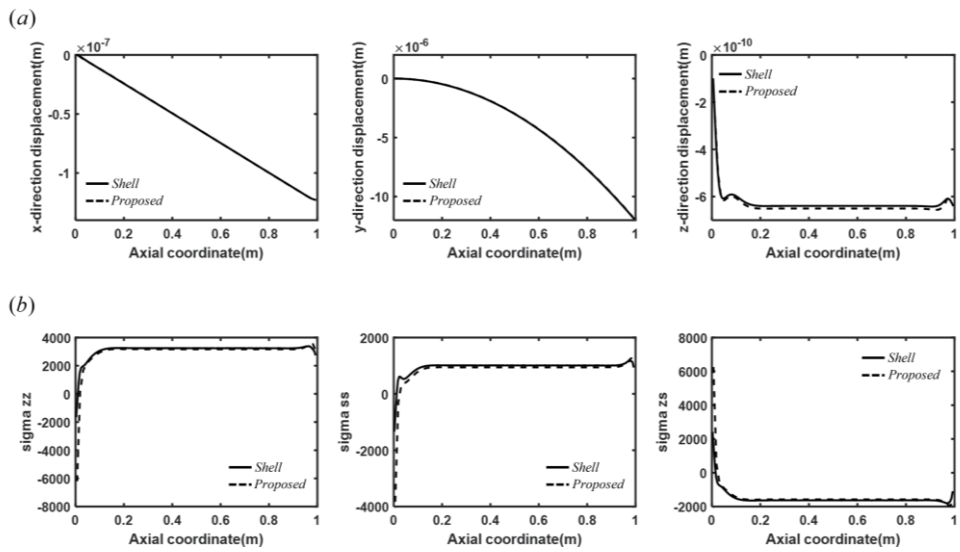


Fig. A.9 Static analysis results for Example 4 in Appendix A considering bending moment loading. (a) Three-dimensional displacement at $s=0$ at the center of wall 1 and (b) stress at $s=b/40$ at the outermost ply of wall 1

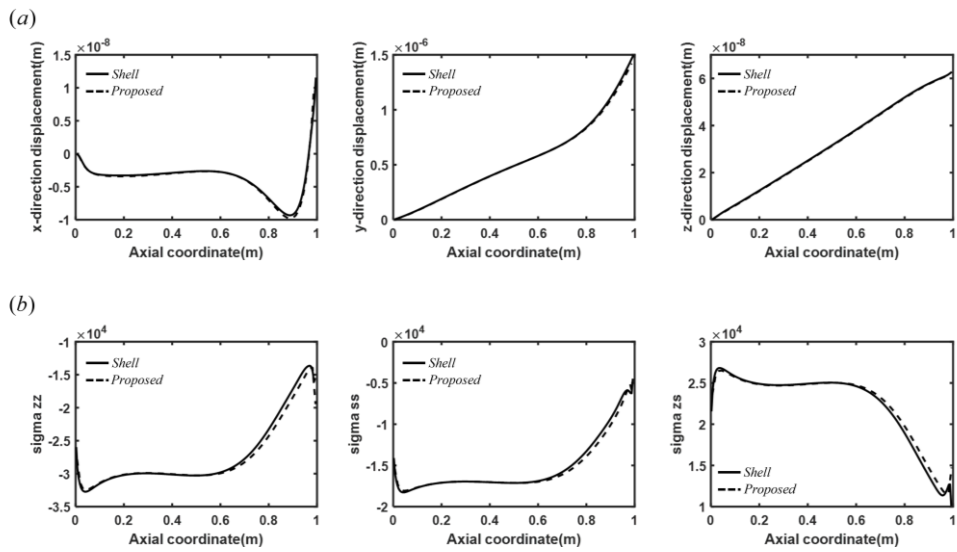


Fig. A.10 Static analysis results for Example 4 in Appendix A considering torsional moment loading. (a) Three-dimensional displacement at $s=0$ at the center of wall 1 and (b) stress at $s=b/40$ at the outermost ply of wall 1

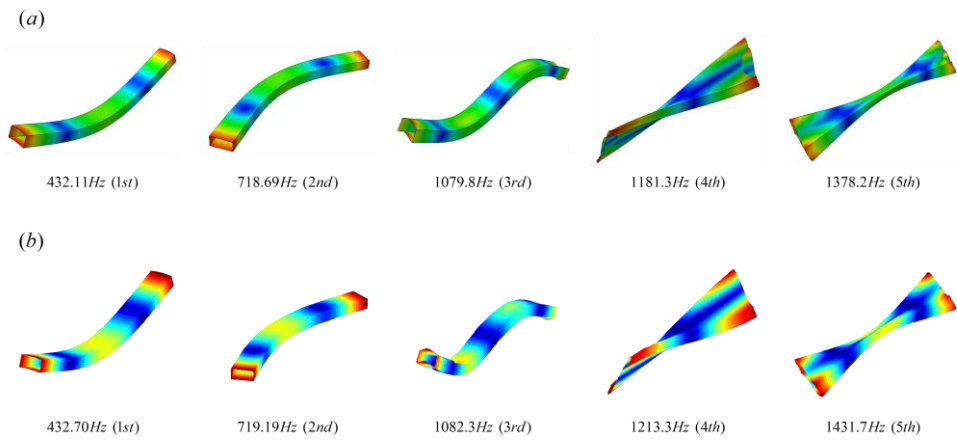


Fig. A.11 Free vibration analysis results for Example 4 in Appendix A. (a) ABAQUS shell results and (b) the present higher-order beam theory results

REFERENCES

- [1] A. Oishi, G. Yagawa, Computational mechanics enhanced by deep learning, *Computer Methods in Applied Mechanics and Engineering*, 327 (2017) 327-351.
- [2] S. Rawat, M.H. Shen, Application of Adversarial Networks for 3D Structural Topology Optimization, in, *SAE Technical Paper*, 2019.
- [3] Y. Yu, T. Hur, J. Jung, I.G. Jang, Deep learning for determining a near-optimal topological design without any iteration, *Structural and Multidisciplinary Optimization*, (2018) 1-13.
- [4] J. Neggers, O. Allix, F. Hild, S. Roux, Big data in experimental mechanics and model order reduction: today's challenges and tomorrow's opportunities, *Archives of Computational Methods in Engineering*, 25 (2018) 143-164.
- [5] T. Kirchdoerfer, M. Ortiz, Data-driven computational mechanics, *Computer Methods in Applied Mechanics and Engineering*, 304 (2016) 81-101.
- [6] T. Kirchdoerfer, M. Ortiz, Data driven computing with noisy material data sets, *Computer Methods in Applied Mechanics and Engineering*, 326 (2017) 622-641.
- [7] T. Kirchdoerfer, M. Ortiz, Data-driven computing in dynamics, *International Journal for Numerical Methods in Engineering*, 113 (2018) 1697-1710.
- [8] B. Peherstorfer, K. Willcox, Dynamic data-driven reduced-order models, *Computer Methods in Applied Mechanics and Engineering*, 291 (2015) 21-41.
- [9] S. Freitag, W. Graf, M. Kaliske, Recurrent neural networks for fuzzy data, *Integrated Computer-Aided Engineering*, 18 (2011) 265-280.

- [10] G.X. Gu, C.-T. Chen, D.J. Richmond, M.J. Buehler, Bioinspired hierarchical composite design using machine learning: simulation, additive manufacturing, and experiment, *Materials Horizons*, 5 (2018) 939-945.
- [11] V.Z. Vlasov, *Thin-walled elastic beams*, National Technical Information Service, 1984.
- [12] K. Yoon, P.-S. Lee, D.-N. Kim, An efficient warping model for elastoplastic torsional analysis of composite beams, *Composite Structures*, 178 (2017) 37-49.
- [13] E. Carrera, G. Giunta, P. Nali, M. Petrolo, Refined beam elements with arbitrary cross-section geometries, *Computers & structures*, 88 (2010) 283-293.
- [14] G. Giunta, S. Belouettar, F. Biscani, E. Carrera, Hierarchical theories for a linearised stability analysis of thin-walled beams with open and closed cross-section, *Adv. Aircraft Spacecraft Sci*, 1 (2014) 253-271.
- [15] S. Minera, M. Patni, E. Carrera, M. Petrolo, P. Weaver, A. Pirrera, Three-dimensional stress analysis for beam-like structures using Serendipity Lagrange shape functions, *International Journal of Solids and Structures*, 141 (2018) 279-296.
- [16] E. Carrera, A. Pagani, M. Petrolo, E. Zappino, Recent developments on refined theories for beams with applications, *Mechanical Engineering Reviews*, 2 (2015) 14-00298-00214-00298.
- [17] D. Camotim, N. Silvestre, R. Gonçalves, P.B. Dinis, GBT-based Structural Analysis of Thin-walled members: Overview, Recent Progress and Future Developments, in, Springer Netherlands, Dordrecht, 2006, pp. 187-204.
- [18] R. Gonçalves, M. Ritto-Corrêa, D. Camotim, A large displacement and finite

- rotation thin-walled beam formulation including cross-section deformation, *Computer Methods in Applied Mechanics and Engineering*, 199 (2010) 1627-1643.
- [19] R. Gonçalves, M. Ritto-Corrêa, D. Camotim, A new approach to the calculation of cross-section deformation modes in the framework of generalized beam theory, *Computational Mechanics*, 46 (2010) 759-781.
- [20] M. Abambres, D. Camotim, N. Silvestre, K.J. Rasmussen, GBT-based structural analysis of elastic-plastic thin-walled members, *Computers & Structures*, 136 (2014) 1-23.
- [21] R. Bebiano, R. Gonçalves, D. Camotim, A cross-section analysis procedure to rationalise and automate the performance of GBT-based structural analyses, *Thin-Walled Structures*, 92 (2015) 29-47.
- [22] R. Vieira, F. Virtuoso, E. Pereira, Definition of warping modes within the context of a higher order thin-walled beam model, *Computers & Structures*, 147 (2015) 68-78.
- [23] R. Vieira, F. Virtuoso, E. Pereira, A higher order beam model for thin-walled structures with in-plane rigid cross-sections, *Engineering Structures*, 84 (2015) 1-18.
- [24] R. Vieira, F. Virtuoso, E. Pereira, Buckling of thin-walled structures through a higher order beam model, *Computers & Structures*, 180 (2017) 104-116.
- [25] C.E. Cesnik, D.H. Hodges, VABS: a new concept for composite rotor blade cross-sectional modeling, *Journal of the American Helicopter Society*, 42 (1997) 27-38.

- [26] W. Yu, V.V. Volovoi, D.H. Hodges, X. Hong, Validation of the variational asymptotic beam sectional analysis, *AIAA journal*, 40 (2002) 2105-2112.
- [27] W. Yu, D.H. Hodges, J.C. Ho, Variational asymptotic beam sectional analysis—an updated version, *International Journal of Engineering Science*, 59 (2012) 40-64.
- [28] A. Genoese, A. Genoese, A. Bilotta, G. Garcea, A mixed beam model with non-uniform warpings derived from the Saint Venant rod, *Computers & Structures*, 121 (2013) 87-98.
- [29] A. Genoese, A. Genoese, A. Bilotta, G. Garcea, A geometrically exact beam model with non-uniform warping coherently derived from the Saint Venant rod, *Engineering Structures*, 68 (2014) 33-46.
- [30] A. Genoese, A. Genoese, A. Bilotta, G. Garcea, Buckling analysis through a generalized beam model including section distortions, *Thin-Walled Structures*, 85 (2014) 125-141.
- [31] M.K. Ferradi, X. Céspedes, A new beam element with transversal and warping eigenmodes, *Computers & Structures*, 131 (2014) 12-33.
- [32] M.K. Ferradi, X. Céspedes, M. Arquier, A higher order beam finite element with warping eigenmodes, *Engineering Structures*, 46 (2013) 748-762.
- [33] M.K. Ferradi, A. Lebé, A. Fliscounakis, X. Céspedes, K. Sab, A model reduction technique for beam analysis with the asymptotic expansion method, *Computers & Structures*, 172 (2016) 11-28.
- [34] Y.Y. Kim, J.H. Kim, Thin-walled closed box beam element for static and dynamic analysis, *International journal for numerical methods in engineering*, 45

(1999) 473-490.

[35] J.H. Kim, Y.Y. Kim, One-dimensional analysis of thin-walled closed beams having general cross-sections, *International Journal for Numerical Methods in Engineering*, 49 (2000) 653-668.

[36] J.H. Kim, H.S. Kim, D.W. Kim, Y.Y. Kim, New accurate efficient modeling techniques for the vibration analysis of T-joint thin-walled box structures, *International journal of solids and structures*, 39 (2002) 2893-2909.

[37] J. Kim, Y. Kim, Thin-walled multicell beam analysis for coupled torsion, distortion, and warping deformations, *Journal of applied mechanics*, 68 (2001) 260-269.

[38] S. Choi, Unified higher-order beam analysis for multiply-connected thin-walled box beams. Ph. D. thesis, Seoul National University, 2016.

[39] S. Choi, Y.Y. Kim, Analysis of two box beams-joint systems under in-plane bending and axial loads by one-dimensional higher-order beam theory, *International Journal of Solids and Structures*, 90 (2016) 69-94.

[40] D. Shin, S. Choi, G.-W. Jang, Y.Y. Kim, Finite element beam analysis of tapered thin-walled box beams, *Thin-Walled Structures*, 102 (2016) 205-214.

[41] I.S. Choi, G.-W. Jang, S. Choi, D. Shin, Y.Y. Kim, Higher order analysis of thin-walled beams with axially varying quadrilateral cross sections, *Computers & Structures*, 179 (2017) 127-139.

[42] D.-M Kim, S. Choi, G.-W. Jang, Y.Y. Kim, Buckling analysis of thin-walled box beams under arbitrary loads with general boundary conditions using higher-

order beam theory, *Journal of Mechanical Science and Technology*, (2019)
Accepted.

[43] D. Shin, S. Choi, G.-W. Jang, Y.Y. Kim, Higher-order beam theory for static and vibration analysis of composite thin-walled box beam, *Composite Structures*, 206 (2018) 140-154.

[44] J. Loughlan, M. Ata, The analysis of carbon fibre composite box beams subjected to torsion with variable twist, *Computer methods in applied mechanics and engineering*, 152 (1998) 373-391.

[45] T.P. Vo, J. Lee, Flexural–torsional behavior of thin-walled composite box beams using shear-deformable beam theory, *Engineering Structures*, 30 (2008) 1958-1968.

[46] C.E. Cesnik, D.H. Hodges, VABS: a new concept for composite rotor blade cross-sectional modeling, *Journal of the American Helicopter Society*, 42 (1997) 27-38.

[47] W. Yu, D.H. Hodges, J.C. Ho, Variational asymptotic beam sectional analysis—an updated version, *International Journal of Engineering Science*, 59 (2012) 40-64.

[48] S.N. Jung, I.-J. Park, E.S. Shin, Theory of thin-walled composite beams with single and double-cell sections, *Composites Part B: Engineering*, 38 (2007) 182-192.

[49] A.H. Sheikh, O.T. Thomsen, An efficient beam element for the analysis of laminated composite beams of thin-walled open and closed cross sections, *Composites Science and Technology*, 68 (2008) 2273-2281.

- [50] M. Mitra, S. Gopalakrishnan, M.S. Bhat, A new super convergent thin walled composite beam element for analysis of box beam structures, *International Journal of Solids and Structures*, 41 (2004) 1491-1518.
- [51] A. Pagani, E. Carrera, A. Ferreira, Higher-order theories and radial basis functions applied to free vibration analysis of thin-walled beams, *Mechanics of Advanced Materials and Structures*, 23 (2016) 1080-1091.
- [52] D.C. Cardoso, J.D. Vieira, Comprehensive local buckling equations for FRP I-sections in pure bending or compression, *Composite Structures*, 182 (2017) 301-310.
- [53] A.S. Sayyad, Y.M. Ghugal, Bending, buckling and free vibration of laminated composite and sandwich beams: A critical review of literature, *Composite Structures*, 171 (2017) 486-504.
- [54] N. Silvestre, D. Camotim, First-order generalised beam theory for arbitrary orthotropic materials, *Thin-Walled Structures*, 40 (2002) 755-789.
- [55] N. Silvestre, D. Camotim, Shear deformable generalized beam theory for the analysis of thin-walled composite members, *Journal of Engineering Mechanics*, 139 (2012) 1010-1024.
- [56] E. Carrera, M. Petrolo, Refined one-dimensional formulations for laminated structure analysis, *AIAA journal*, 50 (2012) 176-189.
- [57] E. Carrera, M. Filippi, E. Zappino, Laminated beam analysis by polynomial, trigonometric, exponential and zig-zag theories, *European Journal of Mechanics-A/Solids*, 41 (2013) 58-69.

- [58] E. Carrera, M. Filippi, P.K. Mahato, A. Pagani, Accurate static response of single-and multi-cell laminated box beams, *Composite Structures*, 136 (2016) 372-383.
- [59] A. Genoese, A. Genoese, A. Bilotta, G. Garcea, A generalized model for heterogeneous and anisotropic beams including section distortions, *Thin-Walled Structures*, 74 (2014) 85-103.
- [60] F. Susac, E.F. Beznea, N. Baroiu, Artificial Neural Network Applied to Prediction of Buckling Behavior of the Thin Walled Box, in: *Advanced Engineering Forum*, Trans Tech Publ, 2017, pp. 141-150.
- [61] J. Ferreiro-Cabello, E. Fraile-Garcia, E.M. de Pison Ascacibar, F.J.M. de Pison Ascacibar, Metamodel-based design optimization of structural one-way slabs based on deep learning neural networks to reduce environmental impact, *Engineering Structures*, 155 (2018) 91-101.
- [62] S. Lee, J. Ha, M. Zokhirova, H. Moon, J. Lee, Background Information of Deep Learning for Structural Engineering, *Archives of Computational Methods in Engineering*, 25 (2018) 121-129.
- [63] I. Jolliffe, Principal component analysis, in: *International encyclopedia of statistical science*, Springer, 2011, pp. 1094-1096.
- [64] M.A. Aschheim, E.F. Black, I. Cuesta, Theory of principal components analysis and applications to multistory frame buildings responding to seismic excitation, *Engineering Structures*, 24 (2002) 1091-1103.
- [65] J. Ramachandran, M.A. Aschheim, Sample size and error in the determination

of mode shapes by principal components analysis, *Engineering structures*, 27 (2005) 1951-1967.

[66] H.J. Lee, M.A. Aschheim, D. Kuchma, Interstory drift estimates for low-rise flexible diaphragm structures, *Engineering structures*, 29 (2007) 1375-1397.

[67] B. Lechner, M. Pircher, Analysis of imperfection measurements of structural members, *Thin-walled structures*, 43 (2005) 351-374.

[68] J. Li, U. Dackermann, Y.L. Xu, B. Samali, Damage identification in civil engineering structures utilizing PCA-compressed residual frequency response functions and neural network ensembles, *Structural Control and Health Monitoring*, 18 (2011) 207-226.

[69] R.P. Bandara, T.H. Chan, D.P. Thambiratnam, Frequency response function based damage identification using principal component analysis and pattern recognition technique, *Engineering Structures*, 66 (2014) 116-128.

[70] H. Kim, G.-W. Jang, Higher-order thin-walled beam analysis for axially varying generally shaped cross sections with straight cross-section edges, *Computers & Structures*, 189 (2017) 83-100.

[71] D. Shin, Y.Y. Kim, Data-driven approach for a one-dimensional thin-walled beam analysis, Manuscript submitted for publication.

[72] J.N. Reddy, *Mechanics of laminated composite plates and shells: theory and analysis*, CRC press, 2004.

[73] K.-J. Bathe, *Finite element procedures*, Klaus-Jurgen Bathe, 2006.

[74] S.W. Tsai, N.J. Pagano, Invariant properties of composite materials, in, *AIR*

FORCE MATERIALS LAB WRIGHT-PATTERSON AFB OHIO, 1968.

[75] D. Simulia, ABAQUS 6.13 User's manual, Dassault Systems, Providence, RI, (2013).

[76] R.J. Allemang, The modal assurance criterion—twenty years of use and abuse, *Sound and vibration*, 37 (2003) 14-23.

[77] R.C. Hibbeler, *Statics and mechanics of materials*, Pearson Higher Ed, 2013.

[78] V.V. Volovoi, D.H. Hodges, Single-and multicelled composite thin-walled beams, *AIAA journal*, 40 (2002) 960-965.

ABSTRACT (KOREAN)

데이터 분석 기반 복합소재 박판 보의 유한요소 모델 개발

신 동 일

서울대학교 대학원

기계항공공학부

일 차원 유한요소를 가지고 박판 보의 거동을 해석하기 위해서는 보의 단면에서 발생하는 복잡한 단면 변형을 고려해야 한다. 보 단면에서의 국부적인 변형들을 기술하는 형상 함수들의 엄밀한 정의는 복합소재로 만들어진 박판 보를 해석할 때 더욱 중요해진다. 등방성 물질로 구성된 보에서는 고려되지 않는 이방성 특성과 적층 특성들이 보의 단면에서 발생하는 변형을 더 복잡하게 만들기 때문이다. 이 논문에서는 복합소재 박판 보를 다루기 위한 형상 함수들을 정의하고, 이를 활용하여 기존에 등방성 물질로 구성된 박판 보 해석에 한정되어 있었던 고차 보 이론 연구를 확장한다.

본 연구에서는 데이터 분석 기반 접근을 통하여 일반적인 플라이 각도

및 적층 순서를 포괄하는 다양한 단면의 복합소재 박판 보 해석에 필요한 형상 함수들을 구하였다. 복합소재 박판 보의 쉘 모델 기반 해석 결과들을 통하여 단면 변형들을 대표하는 빅 데이터를 확보하고, 이에 대한 주성분 분석을 수행하여 형상 함수들을 정의하였다. 제안하는 방법론을 통하여 기존의 복합소재 박판 보 해석 연구들에서 요구하였던 보 단면 형상에 대한 특정 기구학적 가정 없이 형상 함수들을 식별할 수 있었다. 또한, 형상 함수들이 특정 플라이 각도나 적층 순서에 제한되지 않고 일관되도록 정의할 수 있었다.

복합소재 박판 보 해석으로 확장한 고차 보 요소들은 확보한 데이터 분석 기반의 형상 함수들을 기반으로 정의되었으며, 제안한 보 요소를 활용하여 다양한 조건에서의 복합소재 박판 보의 정적, 진동 및 좌굴 해석을 수행하였다. 본 논문에서는 다양한 수치 예제들을 통해, 제안하는 일차원 보 해석 모델이 기존의 이차원 쉘 해석 모델들에 준하는 해석을 수행할 수 있음을 입증하였다. 제안하는 연구는 복합소재 박판 보 해석 모델을 요구하는 다양한 산업 분야에 활용될 것으로 기대된다.

주요어: 적층판, 이방성, 박판 보, 단면 변형, 데이터 기반 해석, 유한요소법

학 번 : 2013-22493